TOWARD NON-RECIPROCAL CHIP-SCALE SILICON PHOTONICS

by

Yisu Yang

A dissertation submitted to the Faculty of the University of Delaware in partial fulfillment of the requirements for the degree of Doctor of Philosophy in Electrical and Computer Engineering

Summer 2015

TOWARD NON-RECIPROCAL CHIP-SCALE SILICON PHOTONICS

by

Yisu Yang

Approved: ____

Kenneth E. Barner, Ph.D.
Chair of the Department of Electrical and Computer Engineering

Approved: ____

Babatunde Ogunnaike, Ph.D.
Dean of the College of Engineering

Approved: ____

James G. Richards, Ph.D.
Vice Provost for Graduate and Professional Education

I certify that I have read this dissertation and that in my opinion it meets the academic and professional standard required by the University as a dissertation for the degree of Doctor of Philosophy.

Signed: ____
Mark S. Mirotznik, Ph.D.
Professor in charge of dissertation, advisor

I certify that I have read this dissertation and that in my opinion it meets the academic and professional standard required by the University as a dissertation for the degree of Doctor of Philosophy.

Signed: ____
Michael Hochberg, Ph.D.
Member of dissertation committee, co-advisor

I certify that I have read this dissertation and that in my opinion it meets the academic and professional standard required by the University as a dissertation for the degree of Doctor of Philosophy.

Signed: ____
Keith W. Goossen, Ph.D.
Member of dissertation committee

I certify that I have read this dissertation and that in my opinion it meets the academic and professional standard required by the University as a dissertation for the degree of Doctor of Philosophy.

Signed: ____
Shouyuan Shi, Ph.D.
Member of dissertation committee

ACKNOWLEDGMENTS

I would like to express my special appreciation and thanks to my advisor Dr. Michael Hochberg. Your continuous advice, guidance and support in both research and my career are invaluable. I want to thank Dr. Tom Baehr-Jones who always helps me to generate new ideas and build up research competence.

I would also like to thank Dr. Mark S. Mirotznik for helping me to pass the difficulties in my study. I would also like to thank the members of my dissertation committee: Dr. Keith W. Goossen and Dr. Shouyuan Shi. Your significant inputs are critical for improving the quality of this dissertation. For your brilliant comments and suggestions, thanks to you.

I would also like to thank my important collaborators: Dr. Dennis Prather, Dr. Keren Bergman, Dr. Michal Lipson, Dr. Lukas Chrostowski, Dr. Hong Tang and Dr. Christophe Galland. Your kind personal help and academic supports make me go beyond the boundaries of disciplines.

I appreciate the time to co-work with many excellent students and friends. Many thanks to Ran Ding, Yang Liu, Yi Zhang, Shuyu Yang, Yangjin Ma, Matt Streshinsky, Nick Harris, Li He, Kang Tan, Zhe Xuan, Yifei Zhang, Hang Guan, Qi Li, Ari Novack, Mian Zhang, Lawrence Tzuang and Yoon Ho Daniel Lee.

I sincerely thank University of Delaware and its ECE department's support.

Finally, I thank my parents and my homeland.

TABLE OF CONTENTS

LIST OF TABLES

LIST OF FIGURES

LIST OF ABBREVIATIONS

AFG: Arbitrary Function Generator

APD: Avalanche Photodetector

BOX: Buried Oxide

BPF: Band Pass Filter

CAGR: Compound Annual Growth Rate

CMOS: Complementary Metal Oxide Semiconductor

CW: Continuous Wave

DFB: Distributed Feedback

DUT: Device Under Test

EDFA: Erbium Doped Fiber Amplifier

EO: Electro-Optic

ER: Extinction Ratio

FDTD: Finite Difference Time Domain

FSR: Free Spectral Range

GC: Grating Coupler

IMD3: Third Intermodulation Distortion

InP: Indium Phosphide

I/O: input/output

$LiNbO_3$: Lithium Niobate

MPW: multi-project-wafer

MUX: Multiplexier

MZI: Mach-Zehnder Interferometer

MZM: Mach-Zehnder Modulator

NRZ: Non-Return to Zero

PC: Polarization Controller

PCB: Printed Circuit Board

PD: Photodetector.

PDK: Process Design Kit

PIC: Photonic Integrated Circuit

PM: Polarization Maintaining

Q: Quality Factor

PRBS: Pseudo-random Bit Sequence

RBW: Resolution Bandwidth

RF: Radio Frequency

RTA: Rapid Thermal Anneal

SEM: Scanning Electronic Microscope

SFDR: Spur-Free Dynamic Range

SHD: Second Harmonic Distortion.

SOA: Semiconductor Optical Amplifier

SOI: Silicon-On-Insulator

TE: Transverse Electric

TL: Transmission Line

TWMZ: Traveling Wave Mach-Zehnder

VDL: Variable Delay Line

VNA: Vector Network Analyzer

UD OpSIS: University of Delaware, Optoelectronic Systems Integration in Silicon

WDM: Wavelength Division Multiplexing

ABSTRACT

A critical problem in modern photonics is the optical isolation. An optical isolator allows light to pass through in one direction but blocks it in the other, thereby acting as the optical analogue of an electronic diode. Because such a device induces a preferred direction for light, it must break the symmetry of Maxwell's equations known as Lorentz reciprocity. The effort to find a solution, especially in the realm of “on-chip” photonic integrated circuits (PICs), has generated intense research activities in the past decade.

This dissertation focuses on the reciprocity breaking photonic architecture that is comprised of optical modulators under prescribed driving conditions, optical delay lines and directional couplers in the silicon photonic platform. Unlike isolators based on magneto-optical Kerr effects or nonlinear effects, the author’s non-reciprocal system is built by silicon photonic devices in the linear and reciprocal material platform. We demonstrate the system that works as the optical isolator and circulator at the same time by a fiber-based proof-of-concept experiment. The system architecture provides a practical answer to the challenge of non-reciprocal light routing in PICs. Silicon photonics is the platform for our system as it can provide the high integration density and compatibility with complementary metal oxide semiconductor (CMOS) processing. It is an attractive platform for realizing densely integrated, highly scalable and potentially very low cost solutions for various applications such as on-chip optical interconnects, sensors and all optical processing devices.

A silicon optical modulator that can satisfy the non-reciprocal system's demands is studied. The application of the PN junction's nonlinearity in the modulator can improve the robustness of the non-reciprocal system by removing the signal distortion's influence. The high-linear Mach-Zehnder (TWMZ) modulator in silicon is also presented. Large spur-free dynamic range (SFDR) is verified by experiments when the modulator works at the optimized bias voltage. An advanced PN junction design is applied to reduce the modulator's half wave voltage (V_π) for the high modulation efficiency. We also demonstrate the device's high-speed data transmission operation.

The phase coherence length of the silicon photonic platform is another highlight of the author's work to fulfill a reliable non-reciprocal system. The coherence length can quantitate the semiconductor fabrication uniformity that is critical in the design of complex PICs. A new method is proposed to analyze the random phase fluctuations from more than 800 on-chip silicon Mach-Zehnder interferometers across the wafer. For the first time, the waveguide coherence length of silicon photonic platform is extracted with statistical significance. The coherence length theory is verified by experiments.

Directional coupler is a key passive device in the non-reciprocal system. A fabrication error model is proposed in order to effectively design the low loss compact directional coupler. High consistent performance of device is verified by experiments.

Chapter 1

INTRODUCTION

1.1 Background

In this era, a tremendous amount of information is flooded in front of us through smartphones, laptops and other portable devices. People are closely connected through broadband wired or wireless networks. Network traffic, especially mobile data traffic, is growing at extremely high speed. For example, global mobile data traffic reached 2.5 Exabytes (1 Exabyte=10^{18} Byte) per month at the end of 2014, up from 1.5 Exabytes per month at the end of 2013 [1]. The compound annual growth rate (CAGR) of mobile data traffic is predicted to be 57% from 2014 to 2019 as shown in Figure 1.1 (a). The exponentially increasing number of wireless devices that are accessing mobile networks worldwide as shown in Figure 1.1 (b) is one of the primary contributors to global mobile traffic growth.

(a)

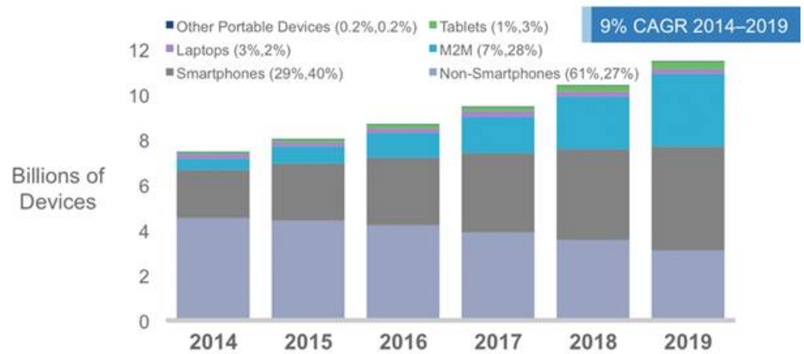

(b)

Figure 1.1: (a) Global mobile data traffic forecast by region. Numbers in parentheses refer to regional share in 2019. (b) Global mobile devices growth forecast. Numbers in parentheses refer to 2014, 2019 device share. Reproduced with permission from [1] (copyright 2015 Cisco).

To keep pace with this data traffic growth rate, the development of integrated circuits will need to follow Moore's law, which predicts that the number of transistors in a dense integrated circuit doubles approximately every two years. However, the continuation of Moore's law will eventually lead to a performance bottleneck. The RC time constant of the traditional metal interconnects will cause the nanometer-scale electronic device performance to deteriorate sharply. Therefore the device bandwidth cannot increase at the rate Moore's law predicted. In addition to time constant deterioration, traditional metal interconnects will become bandwidth limited due to frequency-dependent losses, such as the skin effect and dielectric losses from the printed circuit board (PCB) substrate material [2].

1.2 Silicon Photonics

Optics, which is both an ancient and modern field, has aroused countless curiosities for centuries. It also provides a platform for solving the electrical interconnect bottleneck. An optical signal has much higher bandwidth than its electronic counterparts. Infrared light, around 1550 nm, bandwidth is on the order of 200 THz. Optical signals can also be transmitted by optical waveguides and optic fibers that have significantly less loss and distortion than electronic interconnects. However, the major disadvantages are the high cost and low integration. The alignment and packaging of discrete optical components to build practical systems are time-consuming and expensive. Therefore, monolithic PICs) are in urgent demand. The complementary metal oxide semiconductor (CMOS) process can provide low-cost integrated devices. Under this circumstance, the interdisciplinary field of silicon photonics has attracted intense research enthusiasm since late 1990s. Silicon photonics is the study and application of photonic devices and systems that use silicon as light propagation media, which dates back to late 1980s [3 - 6]. In addition to the broad bandwidth, the strong optical confinement offered by the high index contrast between silicon (n=3.45) and SiO_2 (n=1.45) near 1550nm makes it possible to shrink photonic devices to the hundreds of nanometer level [7]. The major applications of silicon photonics are digital communication [8], analog optical links [9-11] and optical interconnects for electronics [2]. More recently, silicon photonics has been applied in bio-sensing [12], nonlinear optics [13] and quantum optics [14].

Most importantly, the compatibility of silicon photonics with mature silicon IC manufacturing provides competitive prices and performances for PICs. A low cost per unit area for planar waveguide circuits can be achieved by utilizing the CMOS foundry facilities that use Silicon-On-Insulator (SOI) wafers. The latest report of silicon photonics integration density defined by the number of optical components in each die (2.5×3.2 cm^2) is summarized in Figure 1.2 and Moore's law-like growth is predicted. The saturation density is calculated by doubling the record of [8] in order to maintain necessary space for optical I/O to off-chip system. If multi-layer 3D-integration is available [16], there will not be a saturation limit. Therefore, silicon photonics provides a practical and promising path for the urgent requirement in the exponential growth of global data traffic.

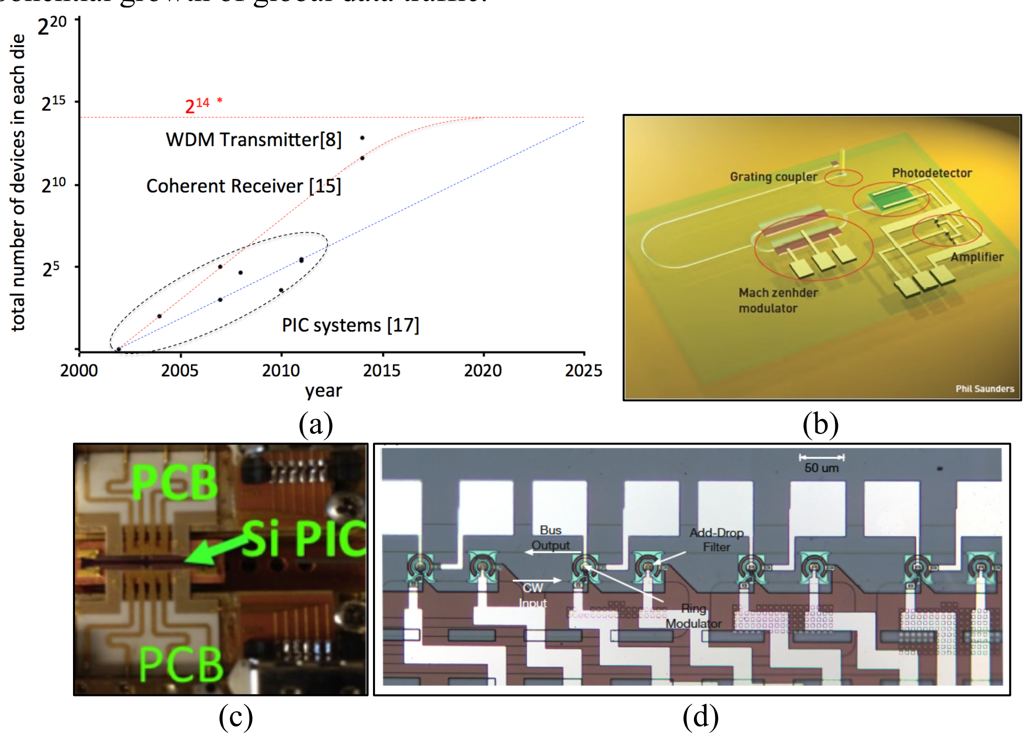

Figure 1.2: The state-of-the-art of silicon photonics integration density. (a) The recent reports and our prediction of integration density of silicon PICs. The prediction of growth speed is shown in the red line (doubling every 12 months) and blue line (doubling every 18 months). (b) The schematic of a silicon PIC for the application of optical communication system. (c) Photograph of the packaged PIC for the coherent transmitter. PCB: printed circuit board. (d) Photograph of the integrated PIC for the modulator-filter-MUX transmitter. Reproduced with permission: (a) from [17], (b) from [18], (c) from [15], (d) from [8].

Silicon photonics is a good candidate for most passive devices and some active devices as shown in the Table 1.1 [19]. Although it is difficult to use silicon to make lasers due to the in-direct band gap, recent work on silicon based lasers either using bonded III-V layers or using III-V quantum dot laser growth on silicon has greatly improved the performance [20, 21]. The rapid development of silicon photonics will therefore provide the full suite of PIC solutions in the future.

Table 1.1: Compare device performance in InP (III-V material), silicon and silicon nitride material systems. Dot: good in performance; circle: bad in performance. 1: edge coupler method, 2: grating coupler (GC) method. Reproduced with permission from [19](copyright 2014 ePIXfab).

	Material System		
Building block	InP	Si	SiN
Passive components	●	●●	●
Lasers	●●●	○	○
Modulators	●●●	●●	●
Switches	●●●	●●●	●
Optical amplifiers	●●●	○	○
Detectors	●●●	●●●	○
Footprint	●●	●●	●
Chip cost	●	●●	●●
CMOS compatibility	○○	●●	●
Low cost packaging	○	○[1]/●●[2]	●●

1.3 Non-Reciprocity in Silicon

In simple terms, reciprocity in optics is “if I can see you, then you can see me”. Thus non-reciprocity denotes, “I can see you but you cannot see me”. Examples of this phenomenon in practice are the optical isolator and circulator. An optical isolator allows light to pass through in one direction but blocks it in the other, thereby acting as the optical analogue of the electronic diode. In a circulator, the light injected from a first input port is transmitted to the output port, while light incoming into the output port is redirected to a third port. Because such devices induce a preferred direction for light, they break the Lorentz reciprocity that is a property of the linear, sourceless time harmonic Maxwell's equations. This is a difficult task and the effort to find a solution, especially in the realm of “on-chip” PICs, has generated significant research interest in the past decade. The optical isolator is currently the only solution in a laser system to effectively prevent instability from strong back reflections. The optical circulator was used to perform tasks such as spectral filtering [22], and more generally they allow for versatile light routing. The author believes, similar to the critical role of electronic diodes and transistors in the development of very-large-scale integration (VLSI), non-reciprocal photonic devices will play a significant role in PICs.

Magneto-optical materials are widely used to realize non-reciprocal devices but hard to fabricate in CMOS processes [23-29]. The achievement of optical isolation without magneto-optical materials has been a long-standing challenge that has regained interest with the development of PIC in silicon and III/V material platforms. Some possible methods include using optical nonlinearities [30,31], opto-mechanical structures [32], and time-varying media [33-37].

In prior work, time-dependent media is used to break time-reversal symmetry [37]. The non-reciprocal system consists of optical modulators that can be fabricated in the silicon photonics platform. The modulator's phase shifters and the modulation drive signals are carefully designed such that a direction-dependent phase difference is realized. Following the pioneering work of Noé and coworkers [34], some state-of-the-art experimental results [33-37] have shown promise along this line of research, but still suffer from either low isolation, prohibitively high insertion loss, or narrow-band operation, and can be complex to implement.

In order to provide a practical answer to above-mentioned challenges, a new architecture for a time-modulated optoelectronic system is proposed. The system performs the key functions of optical isolator and circulator with a minimum level of complexity. Our non-reciprocal system is comprised of discrete optoelectronic devices but is a first proof of principle experiment that is compatible with existing PIC technologies such as integrated silicon photonics. In previous approaches, reciprocity could only be broken if the light travel time through the modulators was larger than the period of the modulation signal, requiring both long modulators and high (>1 GHz) driving frequencies. The author's work overcomes these requirements by using a two-stage architecture in which two Mach-Zehnder modulators are separated by a passive optical delay line. This strongly relaxes the demand on modulator speed and geometry. The main characteristics and performances of this system are compared to previous results on modulation-based isolators in Table.1.2. Lastly, we are the first to demonstrate a device that is also an optical circulator without relying on magneto-optical materials.

Table 1.2: Summary of time-modulated optical isolator systems that achieve broadband isolation.

Ref	Traveling-wave modulator	Delay line	Modulation signal	Circulator	Bandwidth (THz)	Insertion loss (dB)	Extinction Ratio (dB)
[33]	Yes	No	Sine, 10 GHz	No	0.2	70	3
[35]	No	Yes	Sine, 2 GHz	No	5	11	3
[34]	Yes	No	Sine, **2 GHz**	**No**	**3.7**	**23.8**	**30**
[37]	Yes (not on-chip)	No	Sine, 50MHz	No	NA	NA	13
This work	No (not on-chip)	Yes	Square, **20 MHz**	**Yes**	**8.7**	**9.1**	**12.5**

1.4 Other Works Related to Non-Reciprocal System

In the path of exploring the non-reciprocal system in silicon, we have to overcome the challenging requirement for an on-chip broadband low loss optical modulator. On one hand, we want to utilize the nonlinear effects of PN junction phase shifter to increase the non-reciprocal system's robustness. On the other hand, nonlinear effects exerted by the modulator will deteriorate the light signal that passes through the non-reciprocal system and break the phase stability that will result in the high Bit Error Rate (BER). This work includes special nonlinear phase shifters for non-reciprocal systems and high-linear phase shifters for analog optical applications.

The optical modulator is based on reverse-biased silicon PN junctions. This kind of modulator has low power consumption, compact footprint and broad bandwidth simultaneously. Micro-ring based PN junction modulators have been demonstrated [8, 38, 39] although a few issues remain to be fully addressed, such as limited optical bandwidth and thermal stabilization. The other main category of carrier-depletion PN junction modulator is the traveling wave Mach-Zehnder (TWMZ) modulator. The traveling-wave electrode increases device bandwidths by allowing a longer phase shifter for higher modulation efficiency (low V_π) than lumped-element designs, but the longer phase shifter has higher insertion loss. During the time that the work in this thesis was being performed, several other groups demonstrated on-chip silicon modulator improvements. Significant progress has been made in realizing high-speed, low voltage devices with low loss [40]. Recent work has focused on linearity in these devices [9-11] applied in optical analog transmission links. A figure of merit is spur-free dynamic range (SFDR), which is the signal-to-noise ratio of the largest signal that the link can transmit and receive without introducing distortion. However, the SFDR of the link with a single drive silicon push-pull TWMZ modulator has not been previously reported. In this thesis, we demonstrated a single drive push-pull TWMZ modulator in silicon with SFDR experiment results. The modulator can suppress second-order and third-order intermodulation distortion by advanced design method. We also compare linearity performance between silicon modulators and the commercial lithium niobate ($LiNbO_3$) modulators.

Another challenge of our non-reciprocal system is the moderately complex system architecture. The system requires accurate phase control. However, current system level designs in silicon photonics are far from mature due to the lack of reliable fabrication processes and process design kits (PDKs). The fabrication random errors will make the integrated silicon photonic devices' resonance positions unpredictable [41]. Typical devices include micro-rings and Mach-Zehnder interferometers (MZIs). They are basic building blocks in silicon photonics. More power will be spent on the tuning of these devices' resonance positions in order to make them work in the system. It is urgent to find a figure of merit to evaluate the phase uncertainty in the silicon photonic platform.

Traditionally, coherence length was used to characterize the phase noise level of a laser in interferometric measurements. This concept was then applied to study the phase noise of low confinement non-silicon waveguides. However, former coherence length reports in integrated optics didn't show strong statistical significance as they were extracted from small numbers of samples, due to fabrication and test limitations [42]. For instance, typical fiber Bragg grating coherence length is about 10-100 cm [43] and the silica channel waveguide's coherence length was about 27 m [42]. The work in this thesis owes a significant debt to the research of Dr. Adar [42], which performed initial groundbreaking research in the area of coherence length.

We present a new experiment method to analyze the variance of random phase shifts in the waveguides of the multi-project wafer (MPW). Over 800 silicon MZIs in clusters were measured across the wafer. To our best knowledge, we demonstrate for the first time the typical coherence length of a fully functional Si MPW with statistical significance.

1.5 Original Contributions and Dissertation Outline

The author has several original contributions focused on the topic of broadband Lorentz reciprocity breaking in an integrated photonic architecture. Specifically:

- An optical delay line assisted on-chip photonic non-reciprocal architecture in silicon. This architecture features broad bandwidth, low insertion loss and compatible with silicon photonic platform. It realizes both isolation and circulation at the same time at low modulation speed.
- The novel PN junction devices for the non-reciprocal architecture and high-linear application scenarios. One device is a nonlinear phase shifter for non-reciprocal architecture to improve the system robustness. The other is a silicon traveling wave optical modulator that has high linear performance.
- The first report of phase coherence length in the silicon photonic platform with statistical significance as a guideline of designing the phase sensitive PICs like the non-reciprocal system. A new method to analyze the phase errors due to fabrication non-uniformity.
- The low loss directional couplers with high yield for PICs. A fabrication error model is verified by experiments.

This dissertation is organized as follows:

Chapter 2 explains the system working principle and shows comprehensive simulations as well as proof-of-concept experiments for the delay-line assisted broadband low loss time-dependent non-reciprocal architectures. The author presents the system performance and discusses the potential issues in practical applications.

Chapter 3 focuses on the design and experiments of active devices for non-reciprocal system. First, the nonlinearity of PN junction is applied in a phase modulator to increase the robustness of the system. Secondly, a TWMZ on-chip modulator with high linearity is designed and measured.

Chapter 4 discusses the fabrication non-uniformity in the silicon photonic platform, which is a critical issue for the real PIC. The phase coherence length of silicon photonic platform is shown for the first time. It is verified by experiments and can be considered as a basic design guideline of PICs.

Chapter 5 focuses on the design and experiments of high yield low loss silicon directional coupler that is a key passive component in the non-reciprocal system.

Chapter 6 summarizes this dissertation and provides some insights towards future research.

Chapter 2

NON-RECIPROCITY IN SILICON

To break Lorentz reciprocity theorem for silicon's symmetric permittivity and permeability tensor requires one to incorporate magneto-optical materials [24, 28, 29] as well as nonlinear [30, 31], or time-dependent media [35, 36]. The present work's contribution is the time-dependent non-reciprocal system in silicon platform. Unlike prior work, our system uses long optical delay lines and square-wave driving signals in a photonic architecture with two tandem modulators. We present a proof-of-principle experiment based on single-mode polarization-maintaining fibers and commercially available optical modulators. Both the isolator and circulator are realized simultaneously in the architecture. Our theory model and experiment prove that the system is a broadband low loss time-dependent non-reciprocal architecture with the state-of-the-art performance.

2.1 Introduction of Non-Reciprocity

The realization of true non-reciprocity requires breaking Lorentz reciprocity. This is a difficult and interesting topic as mentioned in the chapter 1.3. The physics of non-reciprocity must be clarified at the beginning in order to distinguish it from other superficial alike concepts such as 'one-way' modal conversion and 'one-way' diffraction effects [44]. In general, consider two supported modes in an optical system (for example, a waveguide) with amplitude column vectors **A'**, **B'** and **A''**, **B''** as well as the corresponding electromagnetic fields **E'**(x, y, z), **H'**(x, y, z), **E''**(x, y, z) and

H"(x, y, z) [45,46]. The time-harmonic sourceless Maxwell equations for the first mode are

$$\nabla \times E' = -j\omega\mu H' \tag{2.1}$$

$$\nabla \times H' = j\omega\varepsilon E'. \tag{2.2}$$

Dot multiplying Eq. (2.1) with **H"** and Eq. (2.2) with **E"** and then summing gives:

$$\mathrm{H}''\nabla \times E' + \mathrm{E}''\nabla \times H' = j\omega(\mathrm{E}''\varepsilon\mathrm{E}' - H''\mu H'). \tag{2.3}$$

Applying the same process with interchanged primes yields:

$$\mathrm{H}'\nabla \times E'' + \mathrm{E}'\nabla \times H'' = j\omega(\mathrm{E}'\varepsilon\mathrm{E}'' - H'\mu H''). \tag{2.4}$$

Subtracting these two equations we obtain

$$\nabla \cdot (\mathrm{E}' \times H'' - E'' \times \mathrm{H}') = j\omega(\mathrm{E}''\varepsilon\mathrm{E}' - \mathrm{E}'\varepsilon\mathrm{E}'' - H''\mu H' + H'\mu H''). \tag{2.5}$$

If ε and μ are scalars or symmetric tensors, the right-hand side of Eq. (2.5) adds up to zero, yielding the Lorentz reciprocity theorem:

$$\nabla \cdot (\mathrm{E}' \times \mathrm{H}'' - \mathrm{E}'' \times \mathrm{H}') = 0. \tag{2.6}$$

Eq. (2.6) also holds for materials with gain or loss, provided ε and μ are symmetric. The reciprocity loosely states that the relationship between an oscillating current and the resulting electric field is unchanged if one interchanges the points where the current is placed and where the field is measured. For the specific case of an electrical network, it is sometimes phrased as 'voltages and currents at different points in the network can be interchanged'.

For the magneto-optical material, the permittivity ε is an asymmetric tensor and the order in which E", E' and ε are multiplied becomes important. In this case, the right-hand side of Eq. (2.5) will be non-zero in general. The reciprocity is also broken in the nonlinear material as ε is a function of the electric-field strength and the right-hand side of Eq. (2.5) becomes E"ε(E') E'– E' ε(E") E", which is non-zero if E" and E' are different. The reciprocity also does not hold in structures for which ε and μ depend on time. For example, ε is modulated in time by some external processes. Look into the isolator that is based on this time-dependent principle. A propagating index perturbation is used to couple two specific forward-propagating modes but no pairs of backward-propagating modes. Therefore, the non-reciprocity is realized.

2.2 Theory Model

Optical isolator and circulator are typical devices using non-reciprocity theorem, which are defined in the chapter 1.3. Magneto-optical materials are ubiquitously employed in current bulk and fibered optical systems to achieve key functionalities of optical isolation and circulation. Unfortunately, this kind of material is difficult to integrate in scalable CMOS fabrication processes [24, 28]. As a replacement, the nonlinear non-reciprocal device is intrinsically narrow-band and the performance is power-dependent [29, 30]. Another substitute is the opto-mechanical isolator but it cannot isolate and pass light at the same time [32]. These problems severely limit the widespread applicability of such devices. Recent published reports of on-chip isolators are highlighted in Table.2.1 with device working principles.

Table 2.1: Summary of recent integrated optical isolators' working principles and performances. *ER=extinction ratio, magneto-optical Kerr devices (blue); nonlinearity devices (orange); opto-mechanical devices (purple).

Reference	Material	Results			
		*ER (dB)	Bandwidth (nm)	Insertion Loss (dB)	Features
T. Shintaku [24]	Garnet	27	NA	2~5	Magneto-optical effects
J. Hwang et al. [25]	Liquid crystals	11	50	1	working wavelength is around 500nm (Magneto-optical effects)
W.V. Parys, et al. [27]	InGaAsP, InP, $Co_{50}Fe_{50}$	99 dB/cm	1	18	InGaAsP SOA (Magneto-optical effects)
H. Yokoi et al. [23]	Si, SiO_2 and garnet	21	35	8	Bonding garnet and silicon MZI; device length=4mm (Magneto-optical effects)
L. Bi et al. [28]	Si, SiO_2 and garnet	19.5	1.6 GHz	18.8	Device length=290µm; bonding silicon chip and garnet (Magneto-optical effects)
M. Tien et al. [29]	Si, SiO_2 and garnet	9	0.1	NA	On-chip device; bonding garnet (Ce: YIG) onto a silicon ring resonator with diameter=1.8mm
H. Shimizu et al. [47]	InGaAsP ,InP, Fe	14.7 dB/mm	30	14.1dB/mm	InGaAsP SOA (Magneto-optical effects)
S. Ghosh et al. [48]	Si, SiO_2 and garnet	25	0.5	8	Adhesive bonding (Magneto-optical effects)
Y. Shoji et al. [49]	Si, SiO_2 and Garnet	30	5	13	Chip size is $1.5mm^2$ (Magneto-optical effects)
L. Fan et al. [50]	Si and SiO_2	28	1	12	Nonlinear silicon ring resonators
L. Wang et al. [51]	Si and SiO_2	40	0.1	15.5	Nonlinear silicon ring resonators; 2.3mW input power
S. Manipatruni et al. [32]	Si and SiO_2	20	0.25	0.1	On-chip device using opto-mechanic resonator; mirror size: 100 μm^2

The advent of PICs has made the need for non-reciprocal systems that do not rely on magneto-optic or nonlinear materials. Probably the most promising technology for the non-reciprocity is using time-varying media. A few recent reports [33-35, 37] have shown progresses along this trend, but still suffer from many issues such as low isolation, high insertion loss, narrow-band operation, and complex system integration as shown in Table 1.2. The author proposes a new architecture for a time-modulated optoelectronic system that performs key functions of optical isolator and circulator with a minimum level of complexity. Although, realized by discrete optoelectronic devices, it is a first proof of principle of a design that is compatible with existing PIC technologies like silicon photonics. In previous approaches based on traveling-wave modulators [33,34], reciprocity could only be broken if the light travel time through the modulators was larger than the period of the modulation signal, requiring both long modulators and high (>1 GHz) driving frequencies. We overcome these requirements by using a two-stage architecture in which two Mach-Zehnder modulators are separated by two passive optical delay lines. This strongly relaxes the demand on modulator speed and geometry, as the modulation frequency is inversely proportional to the light propagation time inside the delay line instead of inside the modulator itself. Compared to the scheme used by [35], we achieve the efficient and broadband isolation over the telecommunication band with only two modulators, without the need for a multiplicity of active systems in parallel, drastically reducing the implementation complexity. The main characteristics and performances of our system are compared to previous results on modulation-based isolators in Table 1.2. Lastly, we are the first to demonstrate a device that is also an optical circulator – a vital component in large-scale photonic circuits – without relying on magneto-optical materials.

By making use of a non-sinusoidal drive signal, a time-modulated optical system can be constructed that violates reciprocity. With a square wave signal, theoretically perfect isolation can be achieved. Moreover, by using a passive delay line, the modulation speed can be lowered dramatically to 20 MHz instead of several GHz. Figure 2.1 (a) shows a block diagram of the system. Due to the very low speeds involved, we note that the modulators are expected to function essentially as lumped elements.

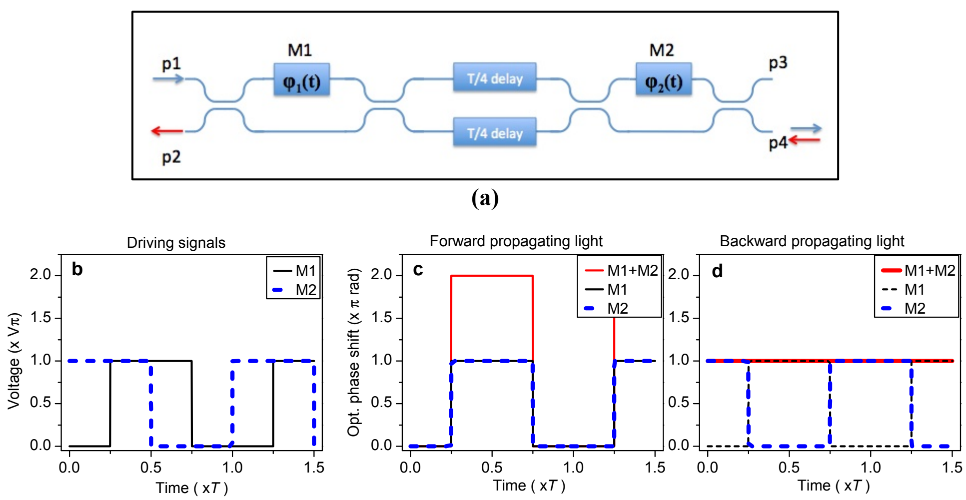

Figure 2.1: Schematics and working principle of the optical isolator/circulator system. (a) Block diagram of our non-reciprocal system, consisting of two Mach-Zehnder modulators in series, separated by a pair of fiber-based delay lines. The path for forward propagation of light is shown in blue, from port p1 to port p4. In contrast, the reverse flow of light is redirected in a nonreciprocal manner from port p4 to p2, as shown by the red arrows. (b) Schematic time-domain square wave signals used to drive the two modulators, in units of V_π, the voltage corresponding to an applied π optical phase. The time axis is in units of the period T of the drive signals. (c) The optical phase modulation experienced by the forward and (d) backward propagating modes, evidencing how our scheme breaks Lorentz reciprocity.

As shown in Figure 2.1, the drive signals of two modulators are shifted by a time lag matching the propagation time in the optical delay line, which is equal to one quarter of the modulation period. As a result, when each modulator is driven with an amplitude V_{π} (Figure 2.1 (b)), the forward-propagating mode experiences an accumulated optical phase shift of 0 or 2π radians (Figure 2.1 (c)), while the backward propagating mode sees a net optical phase shift of π radians (Figure 2.1 (d)). The offset bias of the system has been chosen so that the forward propagating mode is coupled from p1 to p4, while the reverse mode couples from p4 to p2. Thus, non-reciprocal coupling and both isolator and circulator functionalities are achieved.

Next, one can analyze the port-to-port, time-variable transfer function of the non-reciprocal system by the scattering matrix formalism. The complex electric field amplitudes at the input and the output of a four-port network as shown in Figure 2.1 (a) can be written in the vector notation:

$$\begin{pmatrix} p_1 \\ p_2 \end{pmatrix}, \begin{pmatrix} p_3 \\ p_4 \end{pmatrix}. \tag{2.7}$$

To make a simple and clear demonstration of the working principle, we can neglect the loss of each component in Figure 2.1 (a). After discussing the simplified model, we will provide a more complicated model considering the influences of the optical loss, non-idealities in the modulators and the unbalanced length between two delay lines. The scattering matrix of an ideal 50/50 directional coupler can be written as:

$$M_{DC} = \frac{1}{\sqrt{2}} \begin{pmatrix} 1 & i \\ i & 1 \end{pmatrix}. \tag{2.8}$$

The scattering matrices of these two modulators shown in Figure 2.1 (a) can be written as:

$$M_1 = \begin{pmatrix} exp[i\phi_1(t)] & 0 \\ 0 & 1 \end{pmatrix}, M_2 = \begin{pmatrix} exp[i\phi_2(t)] & 0 \\ 0 & 1 \end{pmatrix}. \tag{2.9}$$

Phase shifts ($\phi_1(t)$, $\phi_2(t)$) are time-dependent as shown in Figure 2.1 (b). The scattering matrix of the optical delay line (delay time=T/4) between M1 and M2 writes:

$$M_{Delay} = \begin{pmatrix} i & 0 \\ 0 & i \end{pmatrix}. \tag{2.10}$$

Therefore the total scattering matrix of the system for forward propagation is

$$M_{sys-fwd} = M_{DC} \times M_2 \times M_{DC} \times M_{Delay} \times M_{DC} \times M_1 \times M_{DC} , \tag{2.11}$$

$$M_{sys-fwd} = \frac{1}{2}\begin{pmatrix} -i[e^{i\phi_1(t)} + e^{i\phi_2(t+\frac{T}{4})}] & e^{i\phi_1(t)} - e^{i\phi_2(t+\frac{T}{4})} \\ -e^{i\phi_1(t)} + e^{i\phi_2(t+\frac{T}{4})} & -i[e^{i\phi_1(t)} + e^{i\phi_2(t+\frac{T}{4})}] \end{pmatrix}. \tag{2.12}$$

For light sent into port p1, the input complex field amplitude vector is

$$\begin{pmatrix} p_1 \\ p_2 \end{pmatrix} = \begin{pmatrix} 1 \\ 0 \end{pmatrix}. \tag{2.13}$$

Therefore, the output complex field amplitude vector of the total system is

$$\begin{pmatrix} p_3 \\ p_4 \end{pmatrix} = \mathrm{M}_{sys-fwd} \times \begin{pmatrix} p_1 \\ p_2 \end{pmatrix} = \begin{cases} \begin{pmatrix} 0 \\ -1 \end{pmatrix} & t \in [0, T/4), (3T/4, T] \\ \begin{pmatrix} 0 \\ 1 \end{pmatrix} & t \in [T/4, 3T/4] \end{cases}. \tag{2.14}$$

Eq. (2.14) shows that all the light is directed to port p4, with only an imprinted phase modulation. The system's transfer matrix in reverse operation is

$$M_{sys-rev} = M_{DC} \times M_1 \times M_{DC} \times M_{Delay} \times M_{DC} \times M_2 \times M_{DC}, \tag{2.15}$$

$$M_{sys-rev} = \frac{1}{2}\begin{pmatrix} -i[e^{i\phi_2(t)} + e^{i\phi_1(t+\frac{T}{4})}] & e^{i\phi_2(t)} - e^{i\phi_1(t+\frac{T}{4})} \\ -e^{i\phi_2(t)} + e^{i\phi_1(t+\frac{T}{4})} & -i[e^{i\phi_2(t)} + e^{i\phi_1(t+\frac{T}{4})}] \end{pmatrix}. \tag{2.16}$$

The complex field amplitude vector of input signal to M2 p4 is

$$\binom{p_3}{p_4} = \binom{0}{1} \tag{2.17}$$

Therefore, the output complex field amplitude vector of the total system is

$$\binom{p_1}{p_2} = \mathrm{M}_{sys-rev} \times \binom{p_3}{p_4} = \begin{cases} \binom{0}{i} & t \in (0, T/2) \\ \binom{0}{-i} & t \in [T/2, T] \end{cases}. \tag{2.18}$$

The above equation shows that, in backward direction, all the light will come out at p2 and Lorentz reciprocity is broken. If the RF drive signals are two square-wave voltages that have the same period (T=4×delay time) and the same peak-to-peak amplitude (V_{pp}=V_π) but one is falling behind the other at a period of T/4, perfect isolation is expected. In real applications, the condition for isolation will be broken at rising and falling edges of the non-ideal square drive signals. As long as the modulation frequency is small compared to the bandwidth of the modulators, the duration over which the isolator/circulator function is impaired will be relatively small. This condition is well satisfied in our system, with a measured rise and fall time of 4ns corresponding to a bandwidth of 250 MHz. It is much smaller than each modulator's 3 dB bandwidth that is about 14 GHz (See Appendix A.4). In our design, it is advantageous to use a long delay line for optimal isolation in order to relieve the requirement of high-speed modulation, while a trade-off with increasing insertion loss must be considered.

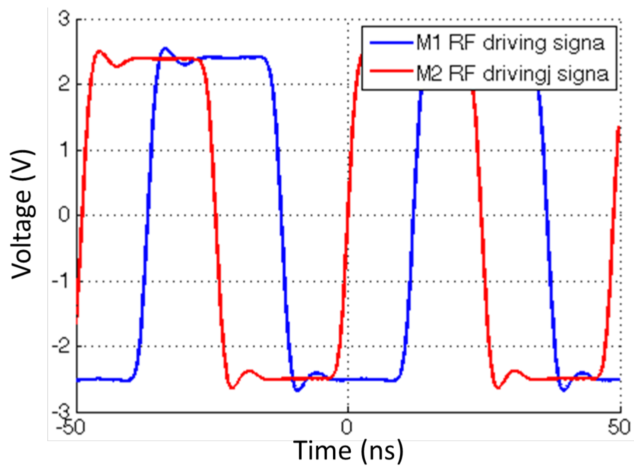

Figure 2.2: Real drive signals of two modulators.

Next, the non-reciprocal system performance is studied when taken into consideration the non-idealities including the non-square waveform, the waveguide insertion losses, the unbalanced length between two optical delay lines, and the modulator's DC bias drift. The directional coupler's scattering matrix is rewritten as:

$$M_{DC}(r,k) = 10^{-k/20}\begin{pmatrix} \sqrt{1-r} & i\sqrt{r} \\ i\sqrt{r} & \sqrt{1-r} \end{pmatrix}, \tag{2.19}$$

where r is the coupler's power coupling ratio (ideally 0.5) and k is the insertion loss (dB). Scattering matrices of two phase modulators are rewritten as:

$$M_1(t,k_1) = \begin{pmatrix} 10^{-k1/20}exp[i\phi_1(t)] & 0 \\ 0 & 10^{-k1/20} \end{pmatrix}, \tag{2.20}$$

$$M_2(t,k_2)=\begin{pmatrix}10^{-k2/20}exp[i\phi_2(t)] & 0\\ 0 & 10^{-k2/20}\end{pmatrix}. \tag{2.21}$$

k_i (i=1,2) is the insertion loss (dB) of i-th modulator (M_i). Based on the real modulator's specification, we select k_1 = 3.4 dB, k_2 = 3.2 dB (See Appendix A.4). The scattering matrix of two optical delay lines between M1 and M2 is rewritten as:

$$M_{Delay}(k_{top},k_{bot})=\begin{pmatrix}10^{-k_{top}/20}exp[i\phi_{top}] & 0\\ 0 & 10^{-k_{bot}/20}exp[i\phi_{bot}]\end{pmatrix}. \tag{2.22}$$

k_{top} and k_{bot} are the insertion losses (dB) of top and bottom optical delay lines.

In the simulation, considering real drive signals shown in Figure 2.2, we modeled each by a sum of a square wave, raised-cosine waves and sine pulses. The sine pulse that overlaps the major square wave at the end of rising/falling edge can be written as:

$$y(t)=A_1e^{-A_2t/T}sin(2\pi f_1t), \tag{2.23}$$

where A_1 = 0.4 V, A_2 = 16 (a.u.), $f_1=5/T$. T is the period of RF drive signal. We use the raised-cosine wave to link the top and bottom levels of square wave. The raise time was about 4 ns as shown in Figure 2.2, so the raised cosine factor (β) is selected as 0.25. The raised-cosine function is:

$$V(t)=\frac{1}{2}V_{pp}\left\{cos\left[\frac{1}{\beta}\pi f_{sa}\left(-t-\frac{1}{2f_{sa}}(1-\beta)\right)\right]\right\}, \tag{2.24}$$

where $f_{sa}=2/T$, V_{pp} is the RF drive signal's peak-to-peak amplitude. The simulated drive signals for two modulators perfectly match real signals (Figure 2.2) shown as below.

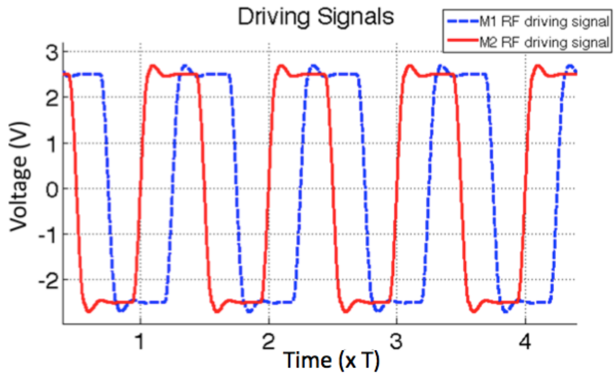

Figure 2.3: Simulation of two RF drive signals for modulators M1 and M2.

The simulated system port-to-port transfer functions in time domain are shown in Figure 2.4. Detailed simulation parameters are summarized in the Table 2.2. The simulated time averaged extinction ratio is about 23.7 dB with insertion loss of 9.5 dB.

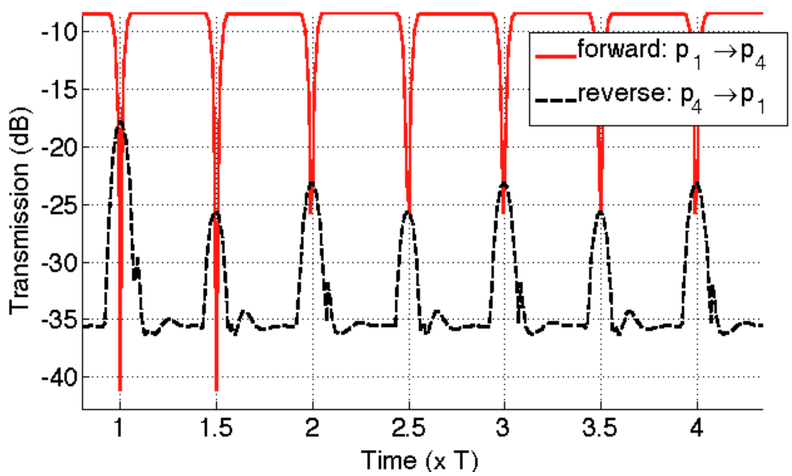

Figure 2.4: Simulated transfer function of non-reciprocal system in forward and backward propagations.

Table 2.2: Simulation parameters used in Figure 2.4.

Parameters	*Value*	*Unit*
M1 Vπ	4.6	V
M2 Vπ	4.6	V
Vpp of driving signal	4.5	V
Splitter coupling ratios	0.5,0.55,0.49,0.5	NA
Splitter losses	0.1,0.1,0.2,0.2	dB
Loss of upper optical delay path	1.2	dB
Loss of lower optical delay path	1.1	dB
Optical path length between M1 and M2	2.51	m
Length difference between bottom path and top path	0.1	mm
M1 insertion loss	3.4	dB
M2 insertion loss	3.2	dB
Group index of light in fiber	1.48	
Modulation frequency	20	MHz
Raising cosine factor	0.25	

2.3 Experiment Results and Discussion

Our isolator/circulator system was realized in polarization-maintaining (PM) single-mode optical fibers by means of two EOSpace™ X-cut lithium niobate 2x2 modulators (See Appendix A.4) configured for push-pull operation. For simplicity and without loss of generality, we replaced push-pull configurations by the equivalent system schematics as shown in Figure 2.1(a). V_π was approximately 4.6 V. In addition to the modulation signal, a DC offset on each modulator was applied to properly bias the phase imbalance of the interferometers. We used two General Photonics™ manual tunable delay lines to balance the path lengths between the two modulators. 2.5 m long of the optical delay line has an accuracy of delay time better than 100 ps. The exact time delay is a key requirement for broadband performance. Arbitrary function generator (AFG, Tektronix™ AFG3252C) provided modulators' RF driving voltage with 4.5V peak-to-peak amplitude. Given the 2.5 m-long optical path of the delay line, the corresponding time-shift of the two drive signals was $T/4$ = 12.4 ns, corresponding to an optimal modulation frequency f = 20.2 MHz. All components in the system were polarization maintaining, and the laser was linearly polarized. Thus, only a single optical mode existed, common to all ports, which was an essential requirement to prove unambiguously the non-reciprocal nature of the system [44,45]. The delay lines were adjusted to give as close to a balanced path as possible, which was correlated with the optical bandwidth seen in a spectral sweep of the circulator transmission from p1 to p4. In the course of our experiments as shown in Figure 2.5, the DC biases on the modulators usually had to be adjusted slightly between measurements. This was due to the fluctuating phase imbalance between the optical paths in the delay line and could easily be mitigated by an active feedback stabilization loop, which would however add unnecessary complexity to our proof-of-principle experiment. Moreover, it is expected that an integrated version of our architecture would be intrinsically much more stable. The delay lines and modulation frequency were not adjusted within each set of steady state and time-domain measurements shown below, but a tiny adjustment was performed between them. In particular, the frequency was adjusted by around 2%. This is likely due to a combination of slightly changing effective path lengths, and possible instabilities in the arbitrary function generator's internal clock.

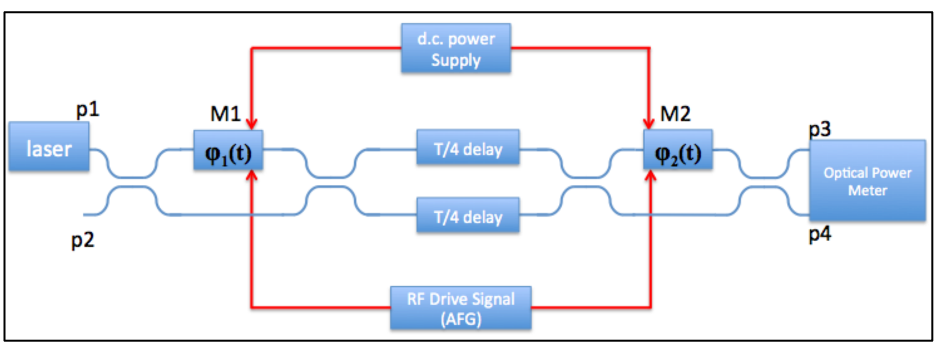

(a)

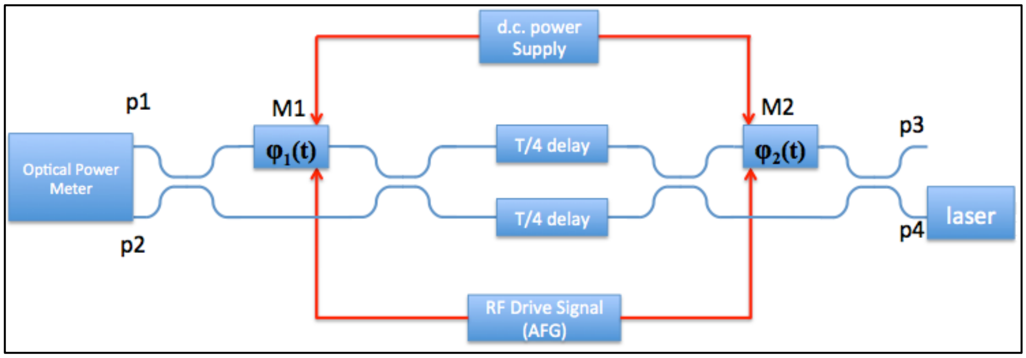

(b)

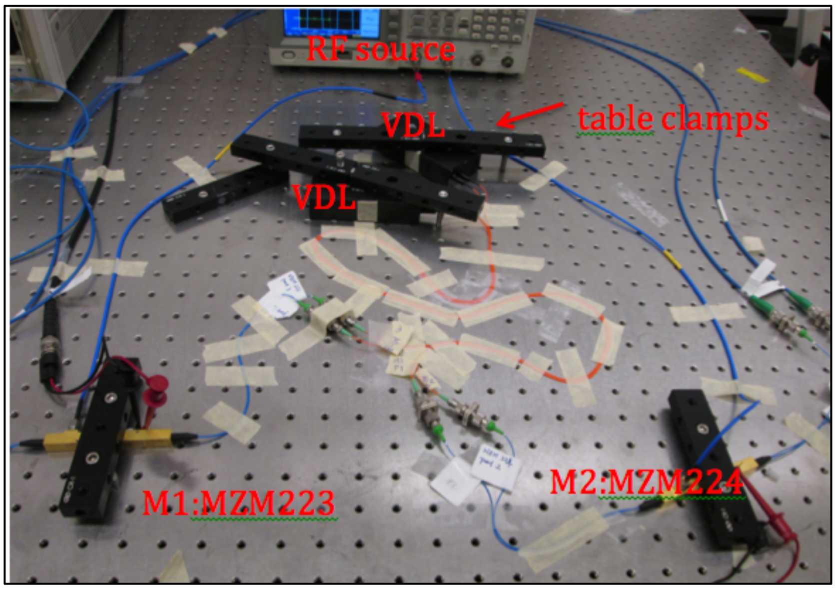

(c)

Figure 2.5: Schematic and photo of the experiment setup: M_1, M_2: Mach-Zehnder Modulator (MZM) 1 and 2; red line: electrical signal path, blue line: optical path. (a) Forward transmission measurement (b) backward transmission measurement (c) photograph of experiment setup; VDL: variable delay line; 223 and 224 are serial numbers.

Accurate balance is essential for optimal operating bandwidth. To balance two optical paths of the delay line, we first maximized the Free Spectral Range (FSR) of the system's transmission without modulation. In forward status, when 0 dBm of continuous wave (CW) laser beam was sent to port p1, port p4 output was measured. In the reverse configuration, keeping all system's parameters unchanged, we sent the same laser beam into port p4 and measured port p1's output power. The laser was swept from 1470 to 1570 nm. The overall power conservation in forward vs. reverse propagation was verified by measuring the ports p2 and p3 outputs.

The main results of isolation are presented in Figure 2.6. The maximum isolator/circulator system excess loss is 9.2 dB with an isolation ER of 12.5 dB or more across the wavelength range 1500 – 1568 nm, which corresponds to a record optical bandwidth of 8.7 THz. The total loss during active operation was only 1 dB more than when the modulators were biased at full transmission and the modulation signal was powered off.

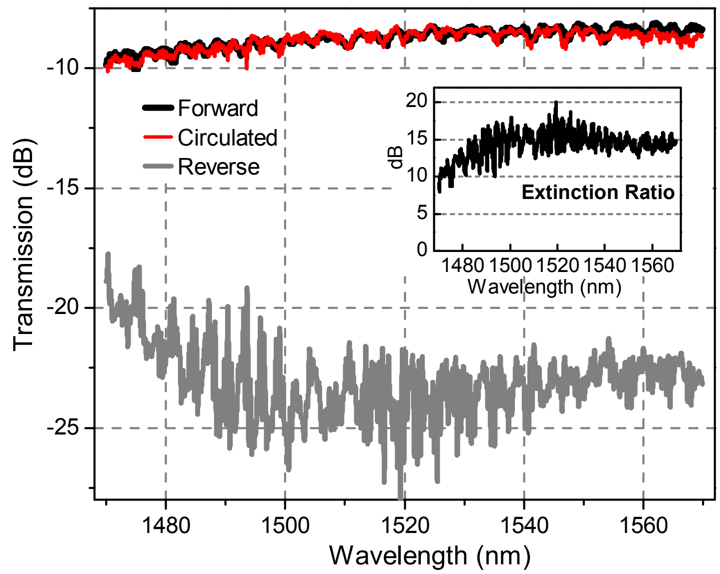

Figure 2.6: The optical characterization of the non-reciprocal system. The laser wavelength was swept from 1470 nm to 1570 nm while measuring the transmission through the forward path from p1 to p4 (black line), the backward path from p4 to p1 (grey line), and the circulated path from p4 to p2 (red line). The extinction ratio of the isolator (the difference between the black and grey curves) is plotted in the inset. It reaches close to 20 dB at some wavelengths and is over 12.5 dB over the 1500 – 1568 nm window. p1 and p4 are defined in Figure 2.1(a).

The real-time output powers of the system in forward and backward configurations were characterized as shown in Figure 2.7. Time domain characterization of the system transmission was performed with a 1.4 GHz bandwidth avalanche photodetector (APD) and optical power meter. So we could obtain the average power sent to the APD while recording the real-time output signal with a fast oscilloscope (Agilent^{TM} DSO7014A 100MHz 2GSa/s). A CW laser beam (wavelength=1555.51nm, power = -8 dBm) was sent successively through the path p1 to p4 (forward path), through p4 to p1 (isolated path), and p4 to p2 (circulated path) to observe any possible fluctuations in the time domain transmission. Experimental results showed that typical amplitudes fluctuations were lower than 1.0% for the forward path, while fluctuations of 23.4% were seen for the isolated path and 1.6% for the circulated path as shown in Figure 2.8 (a). The fluctuations on the isolated path are low in absolute terms, given the high extinction on this port (Inset in Figure 2.8 (a)). The isolation performance is weakened by the non-ideal square wave with a rise and fall time of 4ns as shown in Figure 2.2. But the averaged isolation ratio is still better than 10 dB.

Finally, in view of the important applications of PICs in high-speed digital telecommunications, we characterized the impact of the non-reciprocal system on the data transmission fidelity. Due to the isolator/circulator system working principle, the optical phase is flipped twice per period, which could be problematic if a phase-modulated signal format was sent to the system. Therefore we limit the study here to OOK modulation.

The test setup is shown in Figure 2.7. We sent an optical signal encoding a 25 Gb/s non-return-to-zero (NRZ) pseudo-random bit sequence (PRBS was generated by Tektronix™ Arbitrary Waveform Generator AWG70001A) through the non-reciprocal system from port p1 to p4, and measured the output on a sampling scope (Tektronix™ DSA8200 Digital Serial Analyzer, 10GHz bandwidth). Compared to the signal without the isolator/circulator system (Figure 2.8 (b)), some additional dispersion in the level of the “1” bit was observed, but the so-called “eye” of the diagram remained well open (Figure 2.8 (c)), showing that faithful digital data transmission is not impaired by our system.

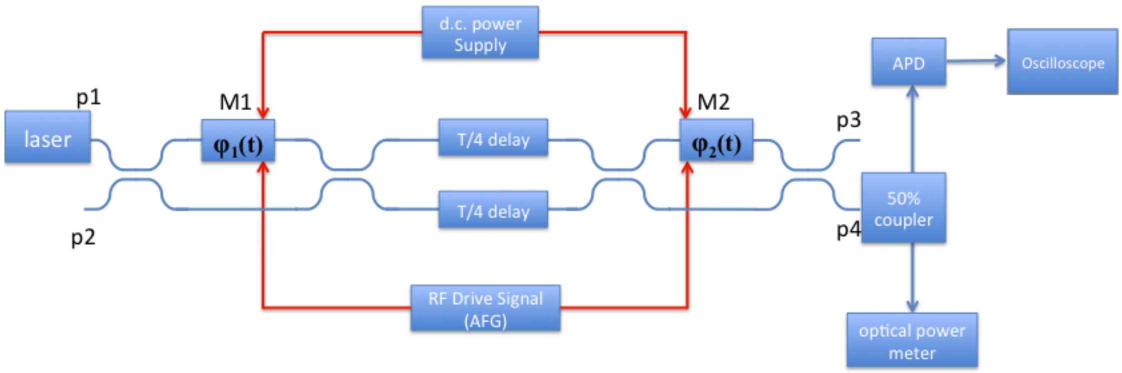

Figure 2.7: Time domain characterization of the system transmission. Forward configuration is shown. Red line: electrical signal path. Blue line: optical path.

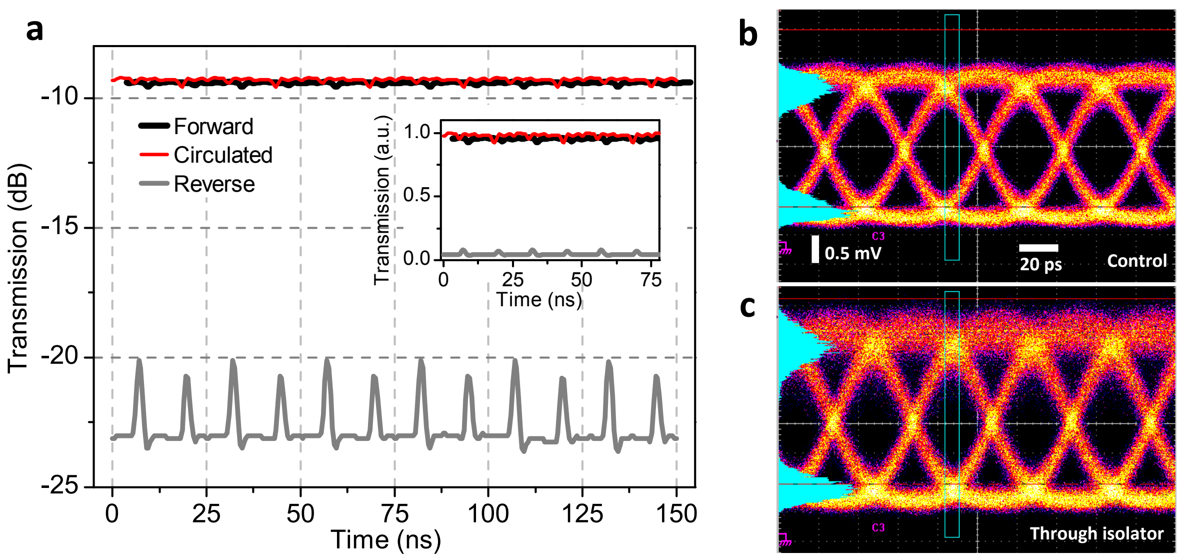

Figure 2.8: Time-domain characterization of the non-reciprocal system. (a) For a CW input light, transmission from p1 to p4, forward path (black line), as well as transmission from p4 to p1 (isolated path, grey line) and p4 to p2 (circulated path, red line). In the inset, the data is plotted on a linear, normalized vertical scale, to show the absolute magnitude of the residual intensity modulations on the transmitted light. (b) PRBS pattern measured on a sampling scope before and (c) after transmission through the isolator/circulator system (path p1 to p4).

We studied the non-reciprocal architecture's robustness when the ideal isolation condition was broken. The experimental modulation frequency was swept from 10.5 MHz to 27.5 MHz while keeping other system parameters the same as described in the former experiment in which the best isolation ER was achieved. Time-averaged forward and backward transmissions were measured. The relationship between ER and driving frequency is shown in in Figure 2.9. The simulation parameters are listed in Table 2.3. Good agreement between theory and experiment was observed. The non-reciprocal architecture can maintain at least 6 dB ER in the face of 10MHz frequency drift of the drive signals.

Table 2.3: Simulation parameters used in Figure 2.9.

Parameter	*Value*	*Unit*
M1 V_π	4.1	V
M2 V_π	4.1	V
Vpp of RF driving signal	5	V
50/50 splitter's phase unbalance: θ	3	degree
Loss of upper optical path	1.8	dB
Loss of lower optical path	1.5	dB
Optical path between M1 and M2 (upper=lower)	2.51	m
M1 insertion loss	3.4	dB
M2 insertion loss	3.2	dB
Phase error due to M1 d.c. bias point deviation	7	degree
Phase error due to M2 d.c. bias point deviation	-4	degree
Group index of light in fiber	1.48	

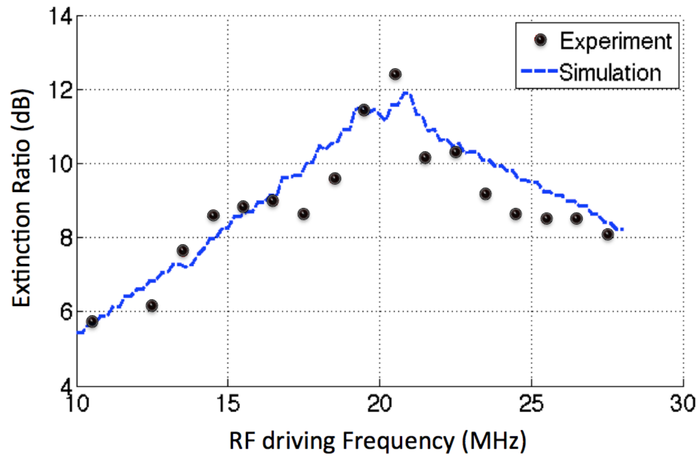

Figure 2.9: Simulated (dashed lines) and experimental results (black dots) of ER at different modulation frequencies of the non-reciprocal system.

Our non-reciprocal architecture has intrinsically flexible isolation characteristics. By tuning the V_{pp} of the driving voltages, we can change the isolation path direction. The driving frequency was 17.43 MHz; DC biases for M1 and M2 were 0.8 V and 2.2 V, respectively. Laser power was 6 dBm at 1550 nm. We measured the system forward and backward transmissions at different peak-to-peak voltage*s*. The simulation results agree well with the experimental data as shown in Figure 2.10. Simulation parameters are listed in Table 2.4. Simulated drive signals are the same as Figure 2.3. The experiment proved that the driving amplitude influences the phase shift of the optical signal and thus changes the ER as well as the isolation path direction. We found that when V_{pp} was about 0.8 V, the isolation direction was switched. The switched direction is from p4 to p1 and the isolation direction is from p1 to p4 as shown in Figure 2.1 (a) and Figure 2.10. This flexibility will make our system a good candidate to support future reconfigurable optical networks or automatic protection systems. It can also be considered as an optical logic device.

Table 2.4: Simulation parameters used in Figure 2.10.

Parameters	*Real Value*	*Ideal Value*	*Unit*
M1 V_π	4.1	4.1	V
M2 V_π	4.3	4.1	V
Vpp of RF driving signal	0 to 10	0 to 10	V
50/50 splitter's phase unbalance: θ	5	0	degree
Loss of upper optical path	1.8	1.5	dB
Loss of lower optical path	1.5	1.5	dB
Optical path between M1 and M2	2.5 and 2.501	2.5	m
M1 insertion loss	3.4	3.4	dB
M2 insertion loss	3.2	3.4	dB
Phase error due to M1 d.c. bias point deviation	2	0	degree
Phase error due to M2 d.c. bias point deviation	-1	0	degree
Group index of light in fiber	1.48	1.48	

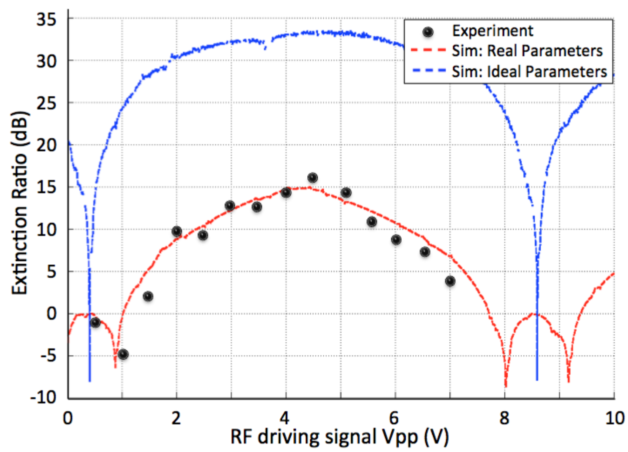

Figure 2.10: Simulated (dashed lines) and experimental results (black dots) of ER at different driving voltage's V_{pp}.

Next, we simulated the modulator's DC biases' influence on the isolation path direction. The DC biases of both modulators were swept from 0V to near $2V_\pi$. Without loss of generality, we assume that the light will experience 0 rad phase shift when the modulator is biased at 0 V, Simulation parameters for both ideal and non-ideal conditions are listed in Table 2.5. Drive signals are the same as Figure 2.3. We found that the DC bias has similar effects of RF V_{pp} and the isolation direction was switched periodically as shown in Figure 2.11. Positive ER means that light can pass from p1 to p4 but is blocked from p4 to p1. Negative ER means the reverse case. Similar to the results of V_{pp}'s influence on the isolation direction, the ER was reduced when using non-ideal simulation parameters. Simulation shows that tuning DC biases can provide more freedom in the control of isolation path direction because high ER is available in many combinations of DC biases.

Table 2.5: Simulation parameters used in Figure 2.11.

Parameters	*Non-ideal Value*	*Ideal Value*	*Unit*
M1 V_π	4.5	4.6	V
M2 V_π	4.7	4.6	V
Vpp of RF driving signal	4.5	4.5	V
50/50 splitter's phase unbalance: θ	3	0	degree
Loss of upper optical path	1.4	1.2	dB
Loss of lower optical path	1.3	1.2	dB
Optical path between M1 and M2	2.51 and 2.511	2.51	m
M1 insertion loss	3.6	3.4	dB
M2 insertion loss	3.5	3.4	dB
M1 DC Bias (0 V-0 rad)	0 to 7	0 to 7	V
M2 DC Bias (0 V-0 rad)	0 to 7	0 to 7	V
Group index of light in fiber	1.48	1.48	

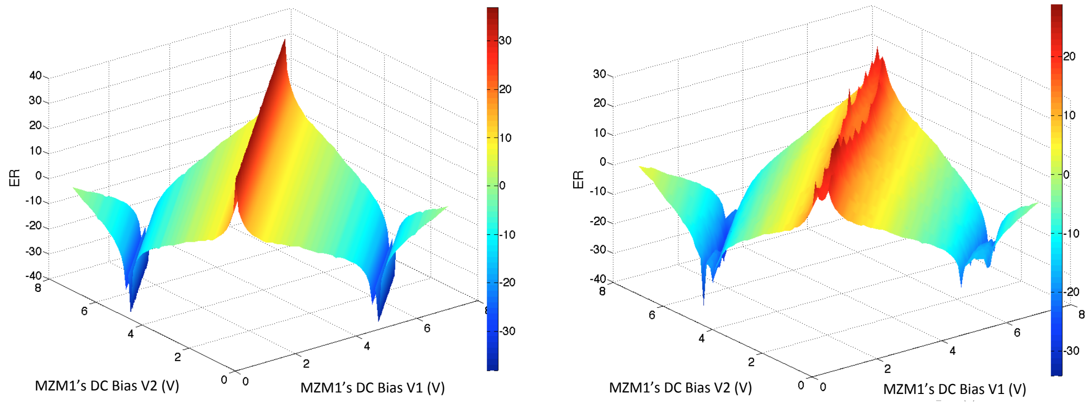

(a) (b)

Figure 2.11: Simulated ER at different DC biases of two modulators in the ideal (a) and non-idea (b) conditions.

To compete with commercial optical isolators [52], the system's ER should be larger than 40 dB for real applications. We can improve the ER by cascading more isolators. To simplify the analysis, we treat the single isolator system as a basic block. We cascade two isolator blocks as shown in Figure 2.12. The optical path from isolator 1, port 1 to isolator 2, port 4 is the forward path as shown by the blue arrows. The path from isolator 2, port 4 to isolator 2, port 2 is the circulation path as shown by the red arrows. The path from isolator 2's port 4 to isolator 1's port 1 is the optical isolated path.

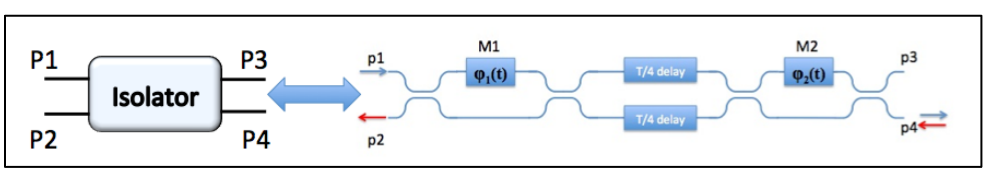

Figure 2.12: Single isolator building block, which is equivalent to the isolator/circulator system shown in Figure 2.1 (a)

We cascaded two isolator blocks as shown in Figure 2.13. Isolator 1's port 4 was connected to isolator 2's port 1. So the optical path from isolator 1's port 1 to isolator 2's port 4 is the forward path as shown by the blue arrows in Figure 2.13. And the path from isolator 2's port 4 to isolator 2's port 2 is the circulation path as shown by the red arrows in Figure 2.13. The path from isolator 2's port 4 to isolator 1's port 1 is the optical isolated path.

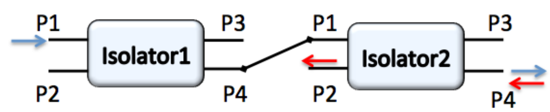

Figure 2.13: The two-isolator cascaded system.

The analyzing method is the same as Section 2.2. Since we have found the isolator block's scattering matrices in both propagation directions as shown in Eq. (2.12) and (2.16), the two-isolator cascaded system's output is easy to calculate. To avoid complex deduction, we do not need to find the total cascaded system's scattering matrix. Instead, we calculated the first isolator block's output that is a 2×1 field amplitude vector. Then we exchanged the row values and set the first row value to be zero to simulate the disconnection between isolator 1's port 3 and isolator 2's port 2 as shown in Figure 2.13. Then this new 2×1 vector was used as the input vector to the isolator 2's scattering matrix. Finally, we can calculate the isolator 2's output field amplitude vector that shows the forward propagation features. By the same way, we can find the backward propagation characteristics. The advantages of this two-isolator system are high ER and low circulator insertion loss (the same as the single block). Moreover, any isolator block's RF drive signals are independent with the other block.

And in each block, two RF drive signals must obey the requirement as shown in Figure 2.1 (b). However, the method will increase the insertion loss of the forward path. We simulated the system transfer function in the time domain as shown in Figure 2.13 by substituting the same parameters for each isolator block as shown in Table.2.2. The simulated RF drive signals were the same as shown in Figure 2.3. Compared with the single block, the two-isolator system's ER is largely improved from 23.7 dB to 116.1 dB and its insertion loss is increased from 9.5 dB to 18.3 dB as shown in Figure 2.14.

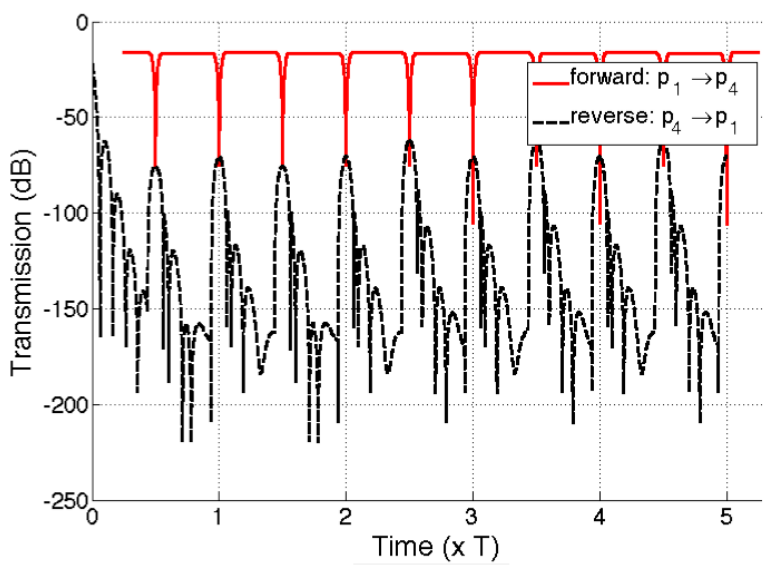

Figure 2.14: The two-isolator cascaded system's time-domain transmission simulation. System simulation parameters are the same as Table.2.2. To simplify the analyzing, all the isolator blocks are identical. In the legend, p1 is isolator 1's port1; p4 is isolator 2' s port 4.

Another disadvantage of this two-isolator cascaded system is that the potential forward path from isolator 1's port 2 to isolator 2's port 3 cannot work due to the requirement of disconnecting isolator 1's port 3 and isolator 2's port 2. People may wonder whether these ports can be connected as shown in Figure 2.15.

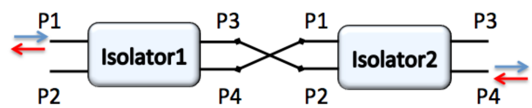

Figure 2.15: A wrong connection for two-isolator cascaded system

If people still want to realize an isolator/circulator non-reciprocal system, the author's answer is no. This is because the total phase-shift that the light experiences in the backward propagation will be 2π after passing the two-isolator cascaded system as shown in Figure 2.15. Therefore, all the output light in backward propagation will come out from isolator 1's port 1 when the input light comes from isolator 2's port 4. We also simulated the time-domain transfer function of the system. The results are shown in Figure 2.16. It's clear that all the backward propagated light from isolator 2's port 4 comes out from isolator 1's port 1.

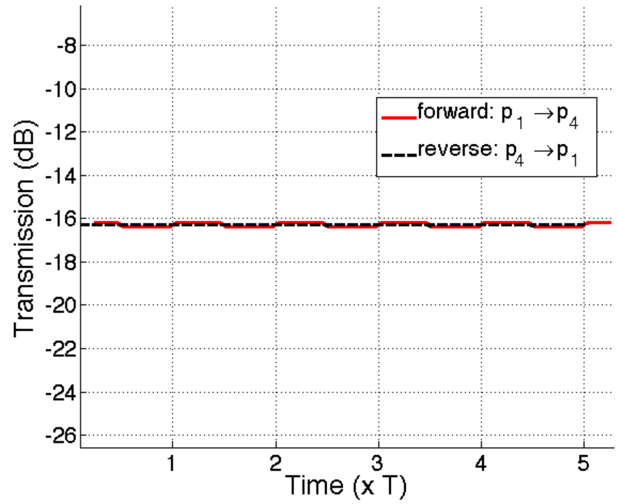

Figure 2.16: The two-isolator cascaded system's time-domain transfer function when the connection is shown in Figure 2.15. p1 is isolator 1's port1; p4 is isolator 2' s port 4.

Then we can move a further step to solve this open-port introduced problem in two-isolator system. The author's method is to use a three-isolator system as shown in Figure 2.17. One attention is that the intermediate output's (2×1 vector's) row values should be exchanged before they are used to calculate the next block's output. Each block's RF drive signals' time delay must obey the requirement as shown in Figure 2.1 (b). But RF drive signals of each block are independent with other blocks.

Figure 2.17: The three-isolator cascaded system.

To simplify analyzing, we set three isolator blocks to be identical in the simulation using parameters as shown in Table 2.2. The RF drive signals are the same as shown in Figure 2.3. From system transmission simulation, we found that the ER was about 53.5 dB and the insertion loss was about 25.5 dB as shown in Figure 2.18. The three-isolator system's disadvantages are the high insertion loss and large device footprint. The ER is less than the two-isolator system's as shown in Figure 2.13 because the two-isolator system removes the entire backward propagating light from isolator 2's port 2 to isolator 1's port 3 by disconnecting them. The advantage of the three-isolator system is that it has two optical isolated paths of high ER. They are from isolator 1's port 1 to isolator 3's port 4 and from isolator 1's port 2 to isolator 3's port 3. Both paths' ERs are larger than 50 dB from simulation. This increases the system flexibility and robustness for future complex applications. The two-isolator cascaded system can only provide one optical isolation path with extremely high ER (>100dB). Although, in the two-isolator system, we can use the path from isolator 1 (or isolator 2)'s port 2 to isolator 1 (or isolator 2)'s port 3 as the optical isolation path, the ER is the same as the single isolator block's, which is about 23.7dB.

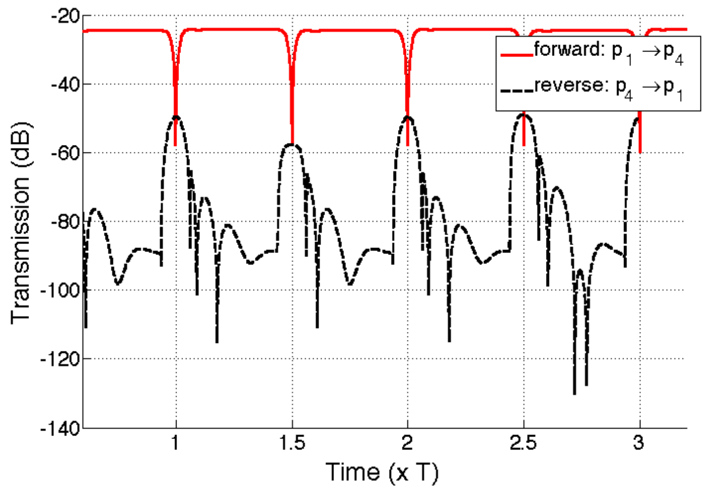

Figure 2.18: The simulated time-domain transfer function of three-isolator cascaded system.

2.4 On-chip Silicon Non-Reciprocal System

One key question is whether the non-reciprocal system presented here could indeed be implemented in integrated silicon photonics. Gathering some of the most recent phase shifter performance results from the literature [53], we find that the phase modulator made by this silicon phase shifter has very high modulation efficiency. Its $V_\pi \cdot L_\pi$ is 0.31 V·cm. That is, if 0.31 V bias is used to drive both arms of the phase modulator with a phase shifter of 1cm length, the π phase shift can be achieved. This phase shifter has a S-size PN junction. And the phase shifter's optical insertion loss is reduced as low as 20dB/cm by multi-step different PN doping profiles that matched the special waveguide geometry and S-size PN junction. Therefore, the phase modulator with S-size PN junction phase shifter is a good candidate for our non-reciprocal system. The schematic of PN junction and doping strategies are shown in Figure 2.19. Experiment showed that the phase modulator had an intrinsic bandwidth of 27 GHz.

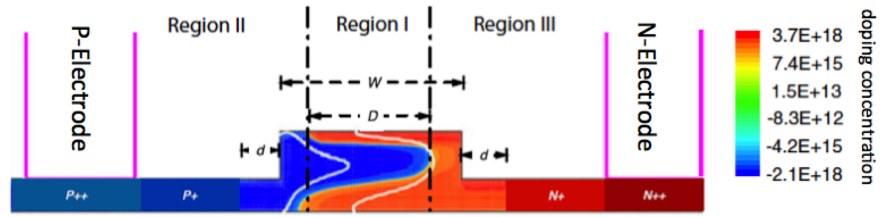

Figure 2.19: Configuration of the proposed S-size PN junction based phase shifter. White line shows the depletion region at 3V reverse bias. Reproduced with permission from [53].

Based on the reported experimental results, we predict that a 1.75 mm long modulator could provide the needed π phase shift (if both arms are driven) with only 3.5 dB of loss at 1.77 Vpp. The needed delay line could be implemented with low-loss silicon ridge waveguides on SOI wafer. It is a standard routing waveguide consisting of a 1.2μm wide rectangular channel. Experimental results showed that it has an average propagation loss of 0.27±0.06 dB/cm [54]. In such waveguides, group indices are around 4.3. Therefore, a 4 cm long on-chip delay line, which entails only 1.08 dB of loss, could enable a modulation frequency around 440 MHz. At such a low speed, a high-quality square wave can be generated and imparted onto the optical phase. And the frequency is much smaller than the bandwidth of high-efficient low-loss silicon phase modulator (27 GHz)[24]. And the 50/50 directional couplers are also available in the silicon photonic platform with insertion loss less than 0.1dB/each (See Chapter 5).

Moreover, both the active and passive devices mentioned above can be fabricated in the same silicon photonics platform provided by the Institute of Microelectronics (IME), a research institute of the Agency for Science, Technology and Research (A*STAR). SOI wafers from SOITEC™, 8 inches in diameter, with a

220 nm device layer and a 2um buried oxide (BOX) layer can be used as a substrate. Three anisotropic etch steps can be employed to define silicon heights of 0, 90 nm, 160 nm and 220 nm, which are used to build the GCs, rib waveguides and strip waveguides. Six separate ion implantation steps (p++, p+, p, n++, n+, n) allow for the design of the S-size PN junction modulators and other active devices like Si-Ge photodetector. The implants are followed by a rapid thermal anneal (RTA) of 1030 °C for 5 seconds to activate the dopants. Finally, contact vias and two levels of Aluminum interconnects can be fabricated. A schematic platform cross-section is shown Figure 2.20 [54].

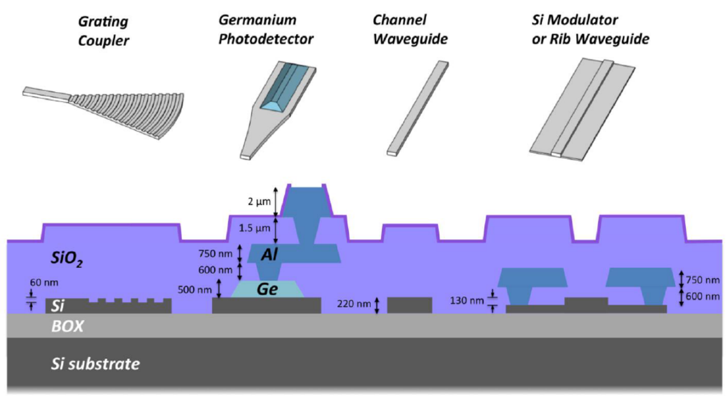

Figure 2.20: Schematics of the layers cross-section and the key components of the platform. Reproduced with permission from [54].

Based on the discussion of real on-chip devices' performance, we choose their parameters with a relative conservative estimation as shown in the Table 2.6 for the non-reciprocal system simulation. The non-reciprocal system architecture is shown in Figure 2.1 (a). From the simulation results shown in Figure 2.21, we found that the on-chip non-reciprocal system's total insertion loss was 8.7 dB and ER was 29.8 dB. Besides, the on-chip system's better performance is expected to exceed the simulation results thanks to the intrinsic stability of integrated Mach-Zehnder interferometers compared to fiber optics. Moreover, if the RF driving voltage can be increased from 1.8 Vpp to 7 Vpp in big power budget applications, the modulator's insertion loss can be further reduced to 0.9dB as phase shifter length is reduced to 0.44 mm. Thus, the non-reciprocal system's forward path insertion loss can be reduced to 4dB while keeping ER at about 30dB.

Table 2.6: Simulation parameters used in Figure 2.21.

Parameters	*Value*	*Unit*
M1 Vπ	1.8	V
M2 Vπ	1.8	V
Vpp of driving signal	1.8	V
Splitter coupling ratios	0.51,0.49,0.5,0.52	NA
Splitter losses	0.1,0.1,0.2,0.2	dB
Loss of upper optical delay path	1.1	dB
Loss of lower optical delay path	1.2	dB
Optical path length between M1 and M2	4	cm
Length difference between bottom path and top path	0	cm
M1 insertion loss	3.5	dB
M2 insertion loss	3.6	dB
Group index of light in fiber	4.3	
Modulation frequency	435.74	MHz

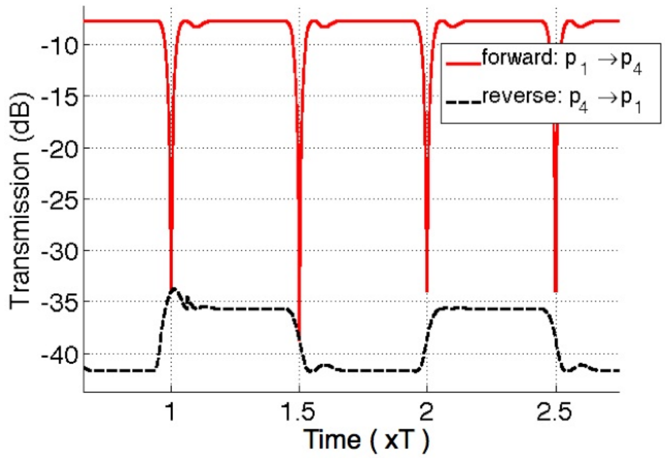

Figure 2.21: Simulation of the on-chip silicon non-reciprocal system.

2.5 Summary

The presented photonic architecture can break Lorentz reciprocity relying on commercial optical modulators. Our theory and experiment show that the non-reciprocal system is both flexible and scalable. If implemented in a silicon photonic platform, system isolation performances would be competitive with the commercial bulk opto-magnetic isolators.

Chapter 3

SILICON PN JUNCTION OPTICAL MODULATOR

The optical modulator is a key component in the non-reciprocal system. In practical applications, the required phase shift for the ideal full isolation may not be satisfied. For example, the RF driving voltage to the phase modulator may have small variations due to the change of outside environmental conditions or the instabilities of the RF source's internal clock. Thus, the phase shift will vary according to the voltage and ER will decrease as shown in Figure 2.10.

To solve this problem, the author's contribution is the design and the realization of a silicon phase shifter that utilizes the PN junction's nonlinearity. Based on this work, we also solve the complex design problem of silicon carrier-depletion optical modulator to achieve high linearity, broad EO bandwidth and high modulation efficiency. The author's design was verified by experiments of real devices fabricated in a CMOS compatible MPW run. This work paves a way to wide applications of silicon optical modulators from the non-reciprocal system to analog optical links.

3.1 Modulator Working Principle

Near-infrared wavelength range plasma dispersion effect in silicon is the main mechanism to build silicon PN junction optical modulators. It shows that the carrier concentration change in silicon results in the change of both real and imaginary part of the refractive index. At wavelength of 1550 nm, the relationship is approximately following [55]:

$$\Delta n = \Delta n_e + \Delta n_h = -8.8\times 10^{-22}\times \Delta N_e - 8.5\times 10^{-18}\times({\Delta N_h}^{0.8}), \tag{3.1}$$

$$\Delta\alpha = \Delta\alpha_e + \Delta\alpha_h = -8.5\times 10^{-18}\times \Delta N_e - 6.0\times 10^{-18}\times \Delta N_h. \tag{3.2}$$

The phase velocity of an optical mode is characterized by its effective index. The above equation directly links carrier concentration to index change of the material, but we also need the relationship that shows how the material index change translates into the perturbation of the effective index of an optical mode. A propagation mode can be expressed as:

$$\begin{pmatrix} \mathrm{E} \\ H \end{pmatrix} = \begin{pmatrix} E_m^*(x,y,\omega) \\ H_m^*(x,y,\omega) \end{pmatrix} e^{-jn_{eff}(\omega)\frac{\omega}{c}z - j\omega t}. \tag{3.3}$$

Substituting (3.3) into Maxwell's equations, we can get:

$$\begin{pmatrix} i\omega\epsilon_0\epsilon(x,y) & 0 & 0 & 0 & 0 & \partial y \\ 0 & i\omega\epsilon_0\epsilon(x,y) & 0 & 0 & 0 & -\partial x \\ 0 & 0 & i\omega\epsilon_0\epsilon(x,y) & -\partial y & \partial x & 0 \\ 0 & 0 & -\partial y & i\omega\mu_0 & 0 & 0 \\ 0 & 0 & \partial x & 0 & i\omega\mu_0 & 0 \\ \partial y & -\partial x & 0 & 0 & 0 & i\omega\mu_0 \end{pmatrix} \begin{pmatrix} E_x \\ E_y \\ E_z \\ H_x \\ H_y \\ H_z \end{pmatrix} \tag{3.4}$$

$$= i\beta \begin{pmatrix} 0 & 0 & 0 & 0 & 1 & 0 \\ 0 & 0 & 0 & -1 & 0 & 0 \\ 0 & 0 & 0 & 0 & 0 & 0 \\ 0 & -1 & 0 & 0 & 0 & 0 \\ 1 & 0 & 0 & 0 & 0 & 0 \\ 0 & 0 & 0 & 0 & 0 & 0 \end{pmatrix} \begin{pmatrix} E_x \\ E_y \\ E_z \\ H_x \\ H_y \\ H_z \end{pmatrix}.$$

Rewrite Eq. (3.4):

$$\mathrm{H}\Psi = \mathrm{i}\beta\mathrm{A}\Psi. \tag{3.5}$$

The Eigen-value of Eq. (3.5) is:

$$\beta = \frac{\Psi^{\mathrm{T}}\mathrm{H}\Psi}{\mathrm{i}\Psi^{\mathrm{T}}\mathrm{A}\Psi}. \tag{3.6}$$

Consider the perturbation in permittivity ε as $\Delta\varepsilon$, H becomes H = H + ΔH. The perturbation is:

$$\Delta H = \begin{pmatrix} i\omega \Delta \epsilon(x,y) & 0 & 0 & 0 & 0 & 0 \\ 0 & i\omega \Delta \epsilon(x,y) & 0 & 0 & 0 & 0 \\ 0 & 0 & i\omega \Delta \epsilon(x,y) & 0 & 0 & 0 \\ 0 & 0 & 0 & 0 & 0 & 0 \\ 0 & 0 & 0 & 0 & 0 & 0 \\ 0 & 0 & 0 & 0 & 0 & 0 \end{pmatrix}. \tag{3.7}$$

So we can get:

$$\beta + \Delta\beta = \frac{(\Psi + \Delta\Psi)^T(\mathrm{H} + \Delta\mathrm{H})(\Psi + \Delta\Psi)}{\mathrm{i}(\Psi + \Delta\Psi)^T \mathrm{A}(\Psi + \Delta\Psi)} \quad . \tag{3.8}$$

Applying perturbation theory to solve Δβ since Δ ε << ε , we can neglect Δ A× Δ B items where A, B= ψ or H and get:

$$\Delta\beta \approx \frac{\Psi^T \Delta\mathrm{H}\Psi}{\mathrm{i}\Psi^T \mathrm{A}\Psi} \quad , \tag{3.9}$$

$$\Delta\mathrm{n}_{eff} \approx \Delta\beta\frac{\mathrm{c}}{\omega} \quad . \tag{3.10}$$

The Eq. (3.9) and (3.10) show that given the modal profile (Ψ) and permittivity change (ΔH), we can calculate the effective index change by the generalized Rayleigh quotient, which is the optical mode-overlap integral [56]:

$$\frac{dn_{eff}}{dn} = 2n\frac{dn_{eff}}{d\epsilon} = \frac{2n}{Z_0}\frac{\iint |E|^2 dS}{\iint (E_x H_y^* - E_y H_x^* + E_x^* H_y - E_y^* H_x) dS} \cdot \tag{3.11}$$

Z_o is the vacuum wave impedance. The integral in the numerator of (3.11) is taken over the region where the refractive index is changing, while the integral in the denominator is taken over the entire x-y plane. This is done assuming that propagation occurs in the z direction. The change of effective index can be calculated by:

$$\Delta n_{eff} = \frac{2n}{Z_0}\frac{\iint \Delta n|E|^2 dS}{\iint (E_x H_y^* - E_y H_x^* + E_x^* H_y - E_y^* H_x) dS} \quad . \tag{3.12}$$

Eq. (3.12) presents a convenient analytic method to predict the shift in the modal effective index induced by a small change in the refractive index in some part of the mode. From Eq. (3.1) and (3.12), we need to change the carrier concentration in the PN junction's depletion region so as to modulate the effective index of an optical mode. This can be done by an electrical voltage signal that applied to PN junction, so that electro-optic modulation can be achieved. The phase shifter's PN junction is reversely biased in our design, because forward biased junctions suffer from slow carrier lifetime that prevents them from achieving high-speed modulation. The depletion region width in P region and N region can be expressed as [57]:

$$\mathrm{W1} \approx \sqrt{\frac{2\epsilon(\mathrm{V}_B + \mathrm{V}_R)\mathrm{N}_D}{q\mathrm{N}_A(\mathrm{N}_D + \mathrm{N}_A)}}\ , \mathrm{W2} \approx \sqrt{\frac{2\epsilon(\mathrm{V}_B + \mathrm{V}_R)\mathrm{N}_A}{q\mathrm{N}_D(\mathrm{N}_D + \mathrm{N}_A)}}\ , \tag{3.13}$$

where

$$\mathrm{V}_B \approx \frac{kT}{q} ln(\frac{\mathrm{N}_A \mathrm{N}_D}{n_i^2})\ . \tag{3.14}$$

V_B and V_R are the built-in voltage and the reverse bias voltage (unit: V) of the PN junction, respectively. N_A and N_D are impurity concentrations (unit: cm^{-3}) of acceptor and donor in P-region and N-region, respectively. k is Boltzmann constant. T is temperature (unit: K). q is the electron charge (unit: C). n_i is intrinsic carrier concentration (unit: cm^{-3}). Changing the depletion width (W=W1+W2) of a PN junction is equivalent to changing the free carrier density. Thus, by changing the bias voltage, we can achieve the refractive index modulation through the free carrier plasma dispersion effect.

The depletion width is usually smaller than the waveguide width of optical modulator phase shifter. A typical phase shifter's cross-section made by rib waveguide is shown in Figure 3.1. And the phase modulation efficiency will be high if optimizing the overlap of the mode profile between the waveguide core and the depletion region. However, to increase the robust performance of the non-reciprocal system, we design the unusual depletion width that can be modulated to be wider than the waveguide width. The design details will be discussed in the next section.

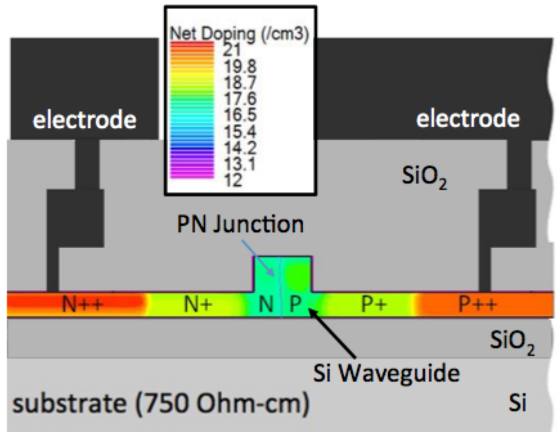

Figure 3.1: A typical phase shifter's cross-section based on rib waveguide (waveguide width=500nm, waveguide thickness=220nm, slab thickness=90nm; slab width=6.5μm) and doping profile simulation results.

3.2 Phase Shifter for Non-Reciprocal Architecture

Our goal is to design a PN junction phase shifter in the phase modulator which is able to provide a π phase shift even the bias voltage may vary in a small range around the ideal V_π. We use the nonlinearity of PN junction to realize this goal. Several assumptions are made. First, the doping concentration is assumed to be constant in the abrupt PN junction. Thus, the free carrier density can be considered proportional to the depletion region's width. There are two strong nonlinear relationships. The first one is shown in Eq. (3.1) and the other one is shown in Eq. (3.13). If the Ohm contact requirement is not so urgent as the power budget is enough and working speed is low as we discussed in the end of Chapter 2, we can use the low doping concentration to reduce optical loss. Moreover, the lightly doped PN junction's depletion region width (W) will have larger variation range than the heavily doped PN junction under the same bias voltage. For example, at the doping level of P and N regions are both 3e16 cm^{-3}, the depletion region width can vary from 240 nm to 745 nm if reverse bias changes from 0v to 5v as shown in Figure 3.2 black curve. However, with the same reverse bias variation, the depletion width can only change less than 100 nm at the heavily doped level of 3e17 cm^{-3} as shown in Figure 3.2 red curve. The simulated net charge concentration in the PN junction was consistent with the results obtained from Eq. (3.13) as shown in Figure 3.3 [58]. By plugging the net charge concentration into Eq. (3.1) and using a standard rib waveguide as shown in Figure 3.1, we found the change of refractive index is about 9e-5 at reverse bias of -5V. Then we extracted the effective index and the $V_\pi L_\pi$ by the FEM mode solver [59]. The simulated $V_\pi L$ is 3.9 V·cm.

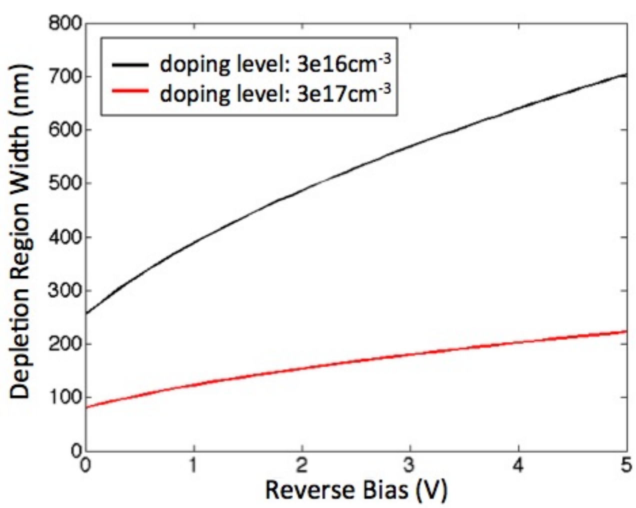

Figure 3.2: The relationship between the depletion region width and the reverse bias at different doping concentrations.

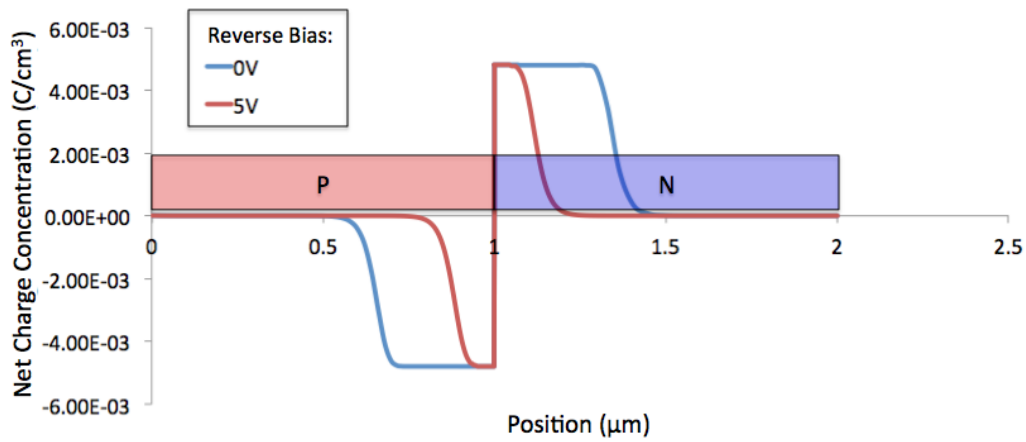

Figure 3.3: The net charge concentration distribution of a PN junction with 3e16 cm^{-3} doping concentration for both P and N regions at different reverse biases.

Then we can design the PN junction for the robust non-reciprocal system. We choose a 5.5 mm-length phase shifter. The $V_\pi \approx 7.1$ V as $V_\pi L$ is 3.9 V·cm. By tuning DC biases, the phase modulator can provide π phase shift when RF voltage is 7.1 V and 0 phase shift when RF voltage is 0 V. As shown in Figure 3.2 (black curve), if RF driving voltage's peak value varies from 7 V to 8 V, the depletion region's width will be larger than the waveguide width that is 500 nm, which means the carrier concentration is constant from the view of the optical mode highly-confined in the waveguide center. Therefore, even the RF driving voltage's peak value has variation as large as 500 mV, the effective index can be approximately kept as a constant. Thanks to the low doping level, the optical insertion loss will be further reduced to around 16 dB/cm by rough simulation. And the disadvantage is that the Ohm contact performance will degrade and the absolute insertion loss for the 5.5 mm phase modulator will be 8.8 dB. To avoid the PN junction breakdown, reverse bias is kept less than 10 V. The reverse breakdown voltage is about 13 V estimated by [57]:

$$V_{break} \approx \frac{\epsilon E_{cr}^2}{2qN_A}. \tag{3.14}$$

$$\text{For Silicon, } E_{cr} \approx \frac{4\times10^5}{1-\frac{1}{3}(log(N_A/10^{16})}. \tag{3.15}$$

We fabricated the phase shifter in IME/A*STAR through an UD OpSIS [54] MPW run. PN junction was created by ion implantation. P doping was realized by boron dopant with ion energy of 16keV and ion dose of 5e12 cm^{-2}. N doping was realized by phosphorus dopant with ion energy of 45 keV and ion dose of 3e12 cm^{-2}. All ion implantation angles were 0 degree. The ion concentrations in P and N regions were about 5.7e16 cm^{-3} and 4.8e16 cm^{-3} simulated by [60]. The experimental doping levels had the same order of our design condition (1e16 cm^{-3}). The ion implantation recipes were fixed because the process must be compatible with foundry's requirements. An unbalanced (arm length difference=100μm) MZI was made by the phase shifters as shown in Figure 3.4. The waveguide cross-section is the same as Figure 3.1. The phase shifter's length is 3 mm. The light around 1550 nm at 6dBm from the tunable DFB laser was coupled in/out of the MZI from two GCs and a fiber array. MZI spectra were measured when the phase shifter was biased at different reverse biases as shown in Figure 3.5. The phase shifter's tunability performance was nonlinear and the max phase shift was saturated when the bias was larger than V_π (about 8.9V). Good agreement between theory and experiment was observed. The difference came from the real fabrication process that introduced more insertion loss and uncertainty in the doping levels.

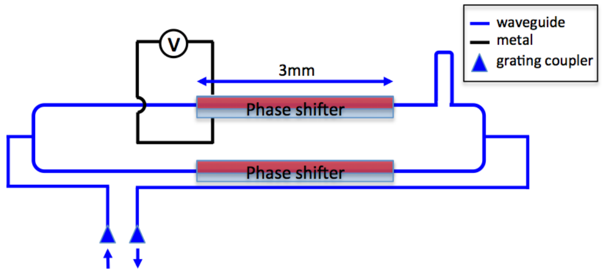

Figure 3.4: Schematic of the unbalanced MZI structure made by phase shifters.

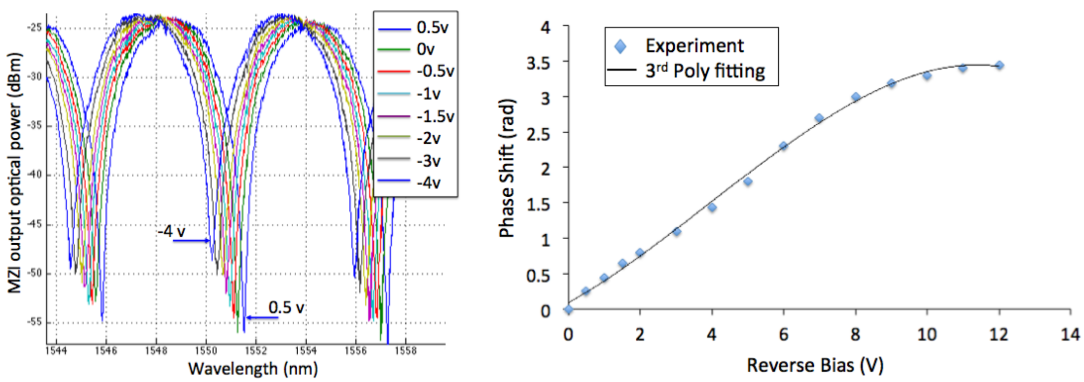

(a) (b)

Figure 3.5: Phase shifter's experimental results. (a) The spectra of the unbalanced MZI structure at different biases. (b) The relationship between phase shift and reverse bias.

3.3 High-linear Optical Modulator

The study of high-linear optical modulator originates from our work of non-reciprocal system but it is not directly related to improve the performance of non-reciprocal system. After showing how to use nonlinearity of PN junction in the design of non-reciprocal system, we will discuss the opposite situation. That is, how to realize high-linear optical modulator with broad EO bandwidth, high modulation efficiency and small footprint.

3.3.1 Introduction

A majority of modulators have been based on reverse-biased silicon PN junctions. Such devices have been used to realize low power consumption, compact footprint and high-speed modulation simultaneously. Micro-ring based PN junction modulators have been demonstrated [8, 38, 39] although a few issues remain to be fully addressed, such as limited optical bandwidth and thermal stabilization. The other main category of carrier-depletion PN junction modulator is the TWMZ modulator. Balanced Mach-Zehnder modulators are relatively temperature insensitive. The traveling wave design increases device bandwidths by allowing a longer phase shifter for higher modulation efficiency (low V_π) than lumped-element designs, but the longer phase shifter has higher insertion loss. Significant progress has been made in realizing high-speed, low voltage devices with low loss [40, 61-68]. Recent work has focused on linearity in these devices [9-11, 61, 69] applied in optical analog transmission links. A figure of merit is spur-free dynamic range (SFDR), which is the signal-to-noise ratio of the largest signal that the link can transmit and receive without introducing distortion. However, the SFDR of the link with a single drive silicon push-pull TWMZ modulator has not been previously reported. It is also important to compare linearity performance between silicon modulators and the commercial $LiNbO_3$ modulators, which are widely used in analog optical links today.

We present a 7-mm long, single drive push-pull TWMZ modulator in silicon. The push-pull scheme can suppress second-order intermodulation distortion, which is the dominant nonlinear term in reverse-biased silicon diodes [70]. Simultaneously, We shift the operating point away from quadrature by tuning the device's common DC bias, which introduces a quadratic term in the sine-square MZ transfer function to lower third-order intermodulation distortion. The SFDR measurement was conducted near 1 GHz in an optical link, which contained our linearized TWMZ modulator. This link's 3rd order intermodulation distortion (IMD3) and second harmonic distortion (SHD) were 100.4 dB·Hz$^{2/3}$ and 90.5 dB·Hz$^{1/2}$ respectively when the modulator's DC common bias was 2 V. It demonstrated an increase in the IMD3 by at least 3.4 dB or 16.4 dB compared to the measured IMD3 of links using a simple TWMZ or ring modulator, respectively [9, 10, 61, 71]. This number was about 5 dB less than the link using a commercial $LiNbO_3$ modulator. The device's $V_\pi \cdot L_\pi$ remained as low as 2.2 V·cm and 15.9 GHz EO bandwidth was achieved. The insertion loss of the device was about 7.7 dB. To our best knowledge, the state-of-the-art linearity performances of recently reported silicon TWMZ and ring modulators are summarized in Figure 3.6 (see Appendix A.1 for details).

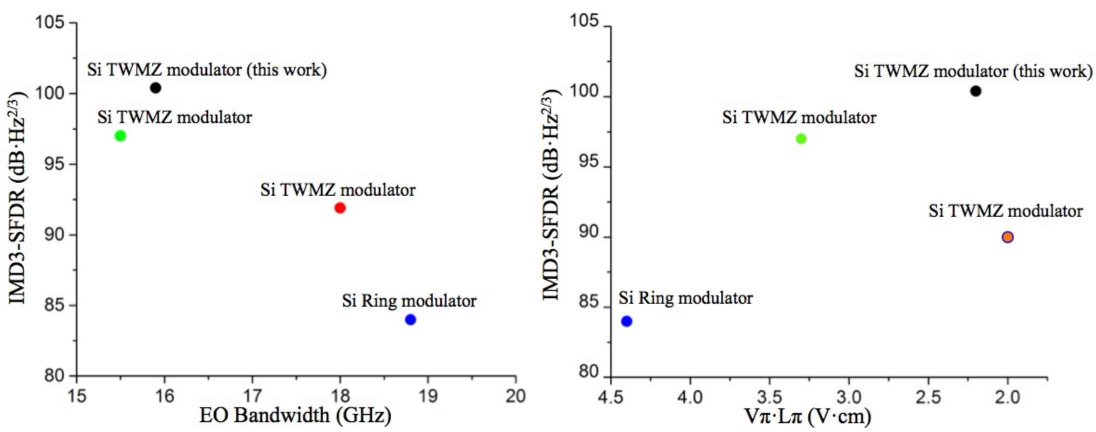

(a) (b)

Figure 3.6: Comparison of the on-chip Si modulator's linearity and other merits: (a) comparison of IMD3 and EO bandwidth; (b) comparison of IMD3 and $V_\pi \cdot L_\pi$. Black dot: this work; red dot: [61]; green dot: [9]; blue dot: [10]; orange dot: [71].

3.3.2 Design Method

To achieve low V_π and low optical insertion loss, the PN junction and phase shifter length of the modulator were carefully optimized. The cross-section of the TWMZ modulator is a "Back-to-Back" PN junction with transmission line (TL) electrode evaporated on the top as shown in Figure 3.7 (a). The model of the modulation section is shown in the inset figure of Figure 3.7 (a). The two diodes (one for each arm) were connected in series with opposite polarity. This configuration provides a push-pull drive scheme. The RF drive signal is delivered between 'S' and 'G' as shown in Figure 3.7 and Figure 3.8. A common DC reverse bias is applied to the middle point through an integrated inductor (metal wire) and resistor (using doped silicon) to isolate the DC and RF signals. As shown in the Figure 3.7 inset figure, with $V_G = 0$, $V_B = V_0 > 0$, and V_S varying between $(-V_{pp}/2, V_{pp}/2)$, if we assume that two diodes are identical, the reverse voltages across the left and right diodes are $(V_0-V_{pp}/4, V_0+V_{pp}/4)$ and $(V_0+V_{pp}/4, V_0-V_{pp}/4)$, respectively, forming a push-pull configuration with a single drive signal. The device's equivalent circuit is schematized in Figure 3.7 (b). The PN junction series resistance and capacitance between the ground (G) and signal (S) electrodes are captured in R_{pn} (in Ω-m) and C_{pn} (in F/m).

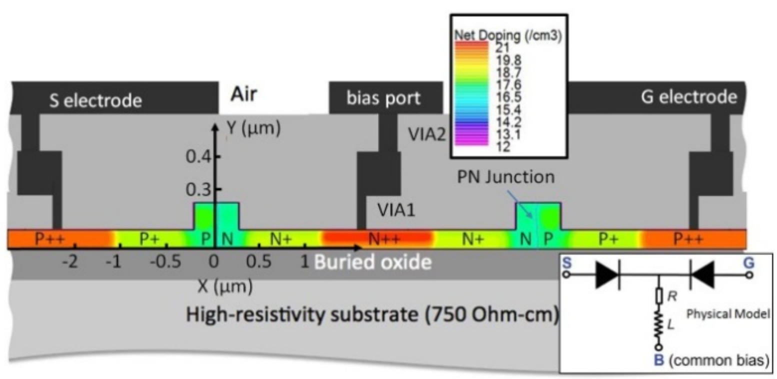

(a)

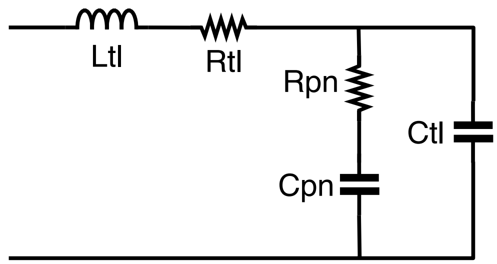

(b)

Figure 3.7: Schematic of the single drive push–pull Si TWMZ modulator: (a) schematic of device cross-section and the simulated doping profile. Schematic is not to scale; (b) schematic of the simplified equivalent circuit of the PN junction loaded TL.

R_{pn} was designed to reduce electrical driving power loss and optical loss while maintaining high modulation efficiency. We employed a 3-level side-doping configuration as illustrated in Figure 3.7 (a). To reduce optical loss, we chose the lightly doped P and N recipes in the waveguide core. The onset of doping to the edge of the waveguide is defined as “clearance”. The clearances of P+ and N+ doping regions were 140 nm and 150 nm respectively. The P++ and N++ doping regions' clearances were both 950 nm, and extend laterally to the electrode contact regions that are 2.3 μm away from the edge of the waveguide. The heavier doped P region (compared to N region) was 100 nm right to the middle of the waveguide core. Our platform employed a 3-level side-doping configuration as illustrated in Figure 3.7 (a). P side average doping concentration was around $5\times10^{17}/cm^3$ and N side was close to $3\times10^{17}/cm^3$. P+ and N+ doping densities of $2\times10^{18}/cm^3$ and $3\times10^{18}/cm^3$ were selected respectively. The P++ and N++ doping were on the level of $1\times10^{20}/cm^3$. As the PN junction geometry was fixed, using the measured sheet resistance value [68], we found $R_{pn}\approx 22.7\ \Omega\cdot$mm.

$V_\pi \cdot L_\pi$ was determined by the PN junction characteristics. Free carrier concentrations of the PN junction in the waveguide's core were simulated at different reverse biases [72]. Setting the operating wavelength to 1.55 μm and substituting carrier concentration, we calculated the change of refractive index as 1.03×10^{-4} from 0 V to -2 V based on plasma dispersion theory [55]. The silicon rib waveguide with silica surrounded had a height of 220 nm, a width of 500 nm and an etching depth of 130 nm for the slab waveguide. The intentional imbalance of the two arms of the TWMZ was 100 μm to make testing convenient. The optical mode simulation [59] showed the change of effective index is 1.1×10^{-4} from 0 V to -2 V. The optical mode simulation is shown in Appendix A.2. We simulated the small-signal $V_\pi \cdot L_\pi$ to be 2.8 V·cm assuming that V_π was 2 V and L_π was the corresponding phase shifter length to achieve π phase shift.

To achieve both low V_π and broad bandwidth, the TL was optimized as following. As shown in Figure 3.7 (b), R_{tl}, C_{tl} and L_{tl} are the TL per unit length metal trace skin resistance, capacitance and inductance, respectively. The TL radio frequency (RF) field loss $\alpha(f)$ was determined by metal series resistance and lateral silicon resistance. The bandwidth of a TWMZ modulator is mostly determined by the RF loss due to R_{pn}, if RF and optical velocities are closely matched. The overall RF field loss coefficient (Neper/m) can be expressed as [68]:

$$\alpha = \alpha_{metal} + \alpha_{Si} , \tag{3.16-a}$$

$$\alpha \approx \frac{R_{tl}(f)}{2Z_{dev}} + \frac{2\pi^2 f^2 C_{PN}^2 Z_{dev}}{1+(\frac{f}{f_{RC}})^2} . \tag{3.16-b}$$

α_{metal} and $\alpha_{silicon}$ are the losses due to metal series resistance and lateral silicon resistance, respectively. Assuming perfect RF and optical mode velocity matching and neglecting other non-ideal RF effects (such as reflection, multi-modal behavior), a relationship between EO 3dB bandwidth $f_{EO,3dB}$ and device length L_{dev} can be derived as [68]:

$$\frac{1-e^{-\alpha(f_{EO,3dB})L_{dev}}}{\alpha(f_{EO,3dB})L_{dev}} = \frac{1}{\sqrt{2}} \Rightarrow \alpha(f_{EO,3dB})L_{dev} \approx 0.74\ \text{Neper} = 6.4\text{dB} \tag{3.17}$$

Therefore, we get the relationship between EO bandwidth ($f_{EO,\,3dB}$) and device length. Substituting *α(f)'s* expression into this relationship and device impedance approximated as $Z_{dev}=[L_{tl}/(C_{tl}+C_{pn})]^{1/2}$, we can calculated the device length as

$$L_{dev} = \frac{0.74}{\frac{R_{tl}(f_{EO,3dB})}{2Z_{dev}} + 2\pi^2 f_{EO,3dB}^2 R_{PN} C_{PN}^2 Z_{dev}}\ . \tag{3.18}$$

By tuning the TL's geometry, R_{tl}, L_{tl} *and* C_{tl} were optimized [73] to yield a 50Ω impedance and RF/optical velocity matching. Without violating fabrication rules [74], the traveling wave electrode strip made by the aluminum M2 layer was 50 μm wide and 2 μm thick. The gap between the electrode and the ground plane was 30 μm as shown in Figure 3.8. The striation of the PN junction with 90% loading factor was to ensure low power loss by guiding the electric current to flow in the metal rather than the silicon. The first SiO_2 buffer layer, 600 nm thick, was sputtered between the silicon waveguide layer and the aluminum M1 layer (750 nm thick). The second SiO_2 buffer layer, 1.5 μm thick, was sputtered between the M1 layer and the M2 layer. Substituting the above geometry, the TL resistance, capacitance and inductance simulation are shown in Figure 3.9 (a-c). The RF total loss, and loss due to R_{tl} and R_{pn}

are plotted separately in Figure 3.9 (d). PN junction related loss is the dominating source of RF loss at high frequencies.

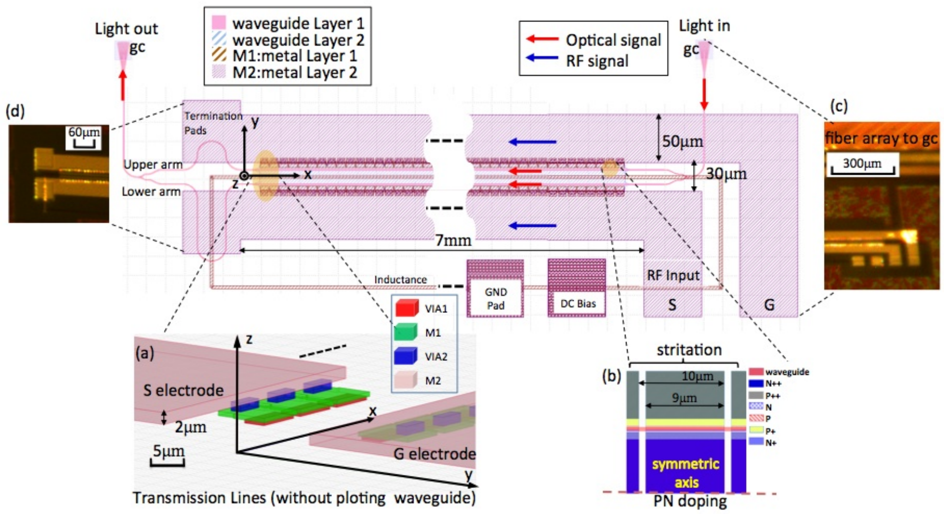

Figure 3.8: Design and microscopic photograph of the single drive push–pull Si TWMZ modulator. Inset figures are: (a) layout of the TL's metal strips; (b) layout of the optical waveguide with PN junction; (c) RF driving ports and a fiber array ; and (d) RF termination ports.

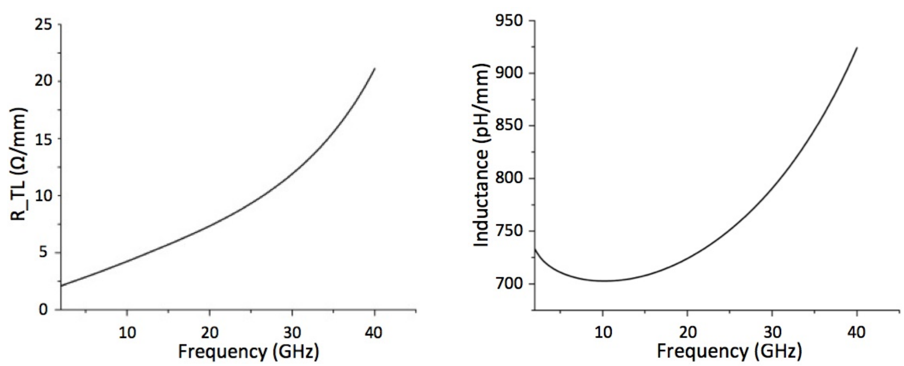

(a) (b)

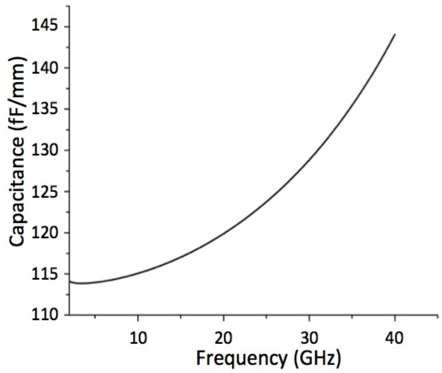

(c)

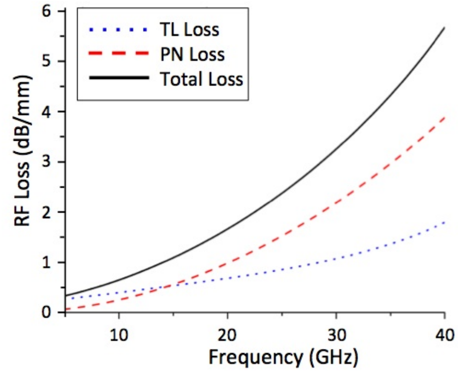

(d)

Figure 3.9: Simulation of TL's RF parameters: (a-c) TL's R, C and L without PN junction; (d) dots: loss due to TL's metal strip; dashed lines: loss due to PN junction; solid lines: loss due to PN junction loaded TL.

A simulation of the PN junction loaded TL is shown in Figure 3.10. At 15 GHz, Z_{dev} and RF field loss are 53.3 Ω and 0.86 dB/mm. At this frequency, the RF index is 4.6, which is close to the optical group index of 4.5. From a design perspective, the traveling electrode length should be shorter than 7.4 mm in order to allow an EO bandwidth higher than 15 GHz, as shown in Figure 3.10 (b). Setting the length to 7.0 mm, the V_π is predicted to be about 4.1 V, which is a balance between the modulation efficiency and the bandwidth.

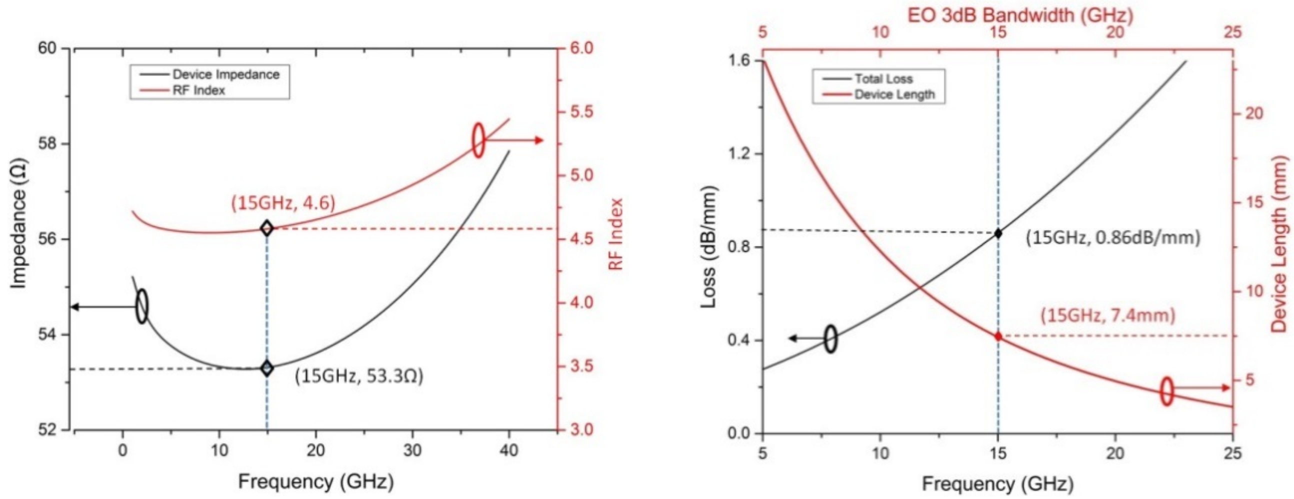

(a) (b)

Figure 3.10: Simulation results of the transmission line parameters: (a) PN junction-loaded TL's impedance and RF index; (b) total RF loss and device length versus EO bandwidth.

3.3.3 Device Fabrication

The device was fabricated at the IME/A*STAR through an UD OpSIS MPW run. Our platform employs six implant layers including lightly doped P and N for forming the junction in the waveguide core, intermediate density P+ and N+ for reducing series resistance without inducing excessive optical loss, and heavily doped P++ and N++ implant for low resistance silicon far away from the waveguide and for forming low resistance metal-to-silicon contact. The traveling-wave phase shifter cross-section is shown in Figure 3.7 (a). The wafer was an 8" SOI from SOITEC with 220 nm top silicon, 2 μm buried oxide layer and 750 Ω-cm high resistive silicon substrate. The 2 μm thick top metal aluminum was used for the traveling-wave electrodes. Other metal and dielectric material properties and thicknesses as well as fabrication steps were identical as reported in [74].

3.3.4 Experiment and Discussion

3.3.4.1 Modulation Efficiency

We first measured the optical transmission and DC performance of the device. The optical experimental setup used a tunable laser (Agilent™ 81980A) centered at a wavelength of 1550 nm. A linearly transverse electric (TE) polarized light beam was coupled into the device using a fiber array and an on-chip GC shown in Figure 3.8 (c). The output light was coupled out of another GC to fiber array and collected by a detector (Agilent™ 8163B). The measured spectra were normalized against the transmission of a straight waveguide without phase shifters but had the same length, shown in Figure 3.11 (a). We tracked the phase shift via the resonance shift in the spectra due to the unbalanced arms of the MZM. Phase shift versus applied reverse bias on one arm is shown in Figure 3.11 (b), from which the V_π was extracted to be 4.3 V. The $V_\pi \cdot L_\pi$ versus applied voltage relation was generated by the measurement of the phase shift $\Delta\phi$ versus the applied voltage $V_{applied}$ on one phase shifter of length L_{dev}, and simply $V_\pi \cdot L_\pi = (\pi/\Delta\phi) \times (V_{applied} L_{dev})$ [68]. As shown in Figure 3.11(c), the measured $V_\pi \cdot L_\pi$ was about 2.2 V·cm at -2 V bias. Further measurements over 5 different chips showed a good uniformity. Compared to the simulated 2.8 V·cm, the difference could come from the real implantation dose being larger than the simulated value, which would enhance the modulation efficiency.

The device insertion loss was obtained by comparing the maximum transmission of the TWMZ spectrum to a GC loop. We measured a device insertion loss of 7.7 ± 0.33 dB, including the two Y-junctions and phase shifter, across five dies on a single wafer. Each Y-junction had an average insertion loss of 0.3 dB ± 0.06 dB across the same wafer [75]. Therefore, the loss due to the phase shifter was 7.1 ± 0.45

dB. The waveguide intrinsic loss was 2.0 ± 0.29 dB/cm [68] contributing about 1.4 dB to the 7-mm phase shifter loss. Therefore the various dopants introduced a loss of approximately 5.7 dB.

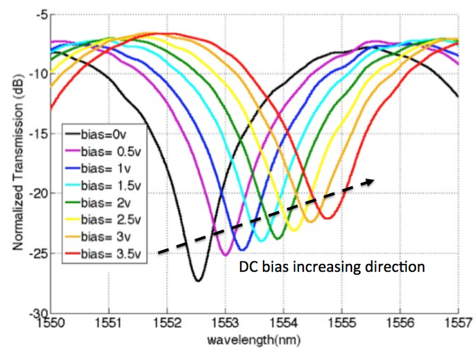

(a)

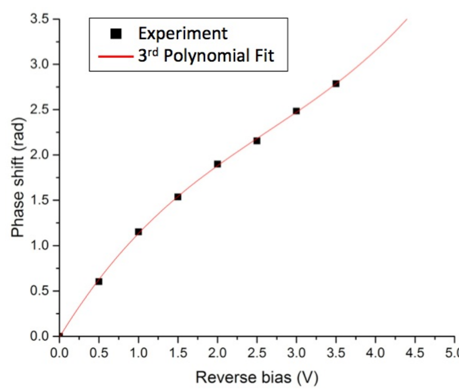

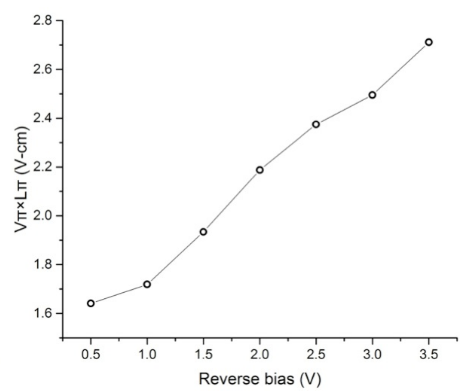

(b) (c)

Figure 3.11: Measured modulation efficiency of the single drive push-pull Si TWMZ modulator: (a) optical spectra versus applied reverse voltages; (b) phase shift versus applied reverse voltage; and (c) $V_\pi L_\pi$ versus applied reverse voltage.

The relationship between the DC phase shift and reverse bias was fitted with a third order polynomial of the form:

$$\Delta\phi = a_1 V + a_2 V^2 + a_3 V^3. \tag{3.19}$$

Fitting parameters are a_1 = 1.42 rad/V, a_2 = -0.32 rad/V^2, a_3 = 0.04 rad/V^3. Substituting Eq. (3.19) and a two-tone (f_1, f_2) time-variant sine driving voltage signal into the MZM transfer function shown in [18], we could obtain the generated multiple frequency components from the output of the TWMZ modulator. The SHD and IMD3 at a desired bias could be derived from this transfer function by examining the components of the 2nd and 3rd order terms of its Taylor expansion that had frequencies $2f_1$ and $2f_1$-f_2.

3.3.4.2 Small-Signal Bandwidth Measurement

The EO frequency response of the TWMZ was characterized using a vector network analyzer (Agilent™ 67 GHz VNA). The RF drive signal and DC bias from VNA port 1 were coupled through a 40 GHz rated Cascade™ ACP GSSG driving probe to the TWMZ driving electrodes and bias port. At the TL's RF output port, the RF signal was terminated by a 40 GHz rated Cascade GS probe with off-chip 50 Ω resistor. A CW laser at 1554.11 nm amplified to 13 dBm was sent to the TWMZ. Light was modulated, coupled out of chip and detected by a 70GHz bandwidth photodetector (U2T™ XPD, responsibility=0.6 A/W). The photodetector output RF signal was coupled back to the VNA. The normalized EO S21 response from a typical device is shown in Figure 3.12. The modulator EO 3dB bandwidth is 8.9 GHz, 15.9 GHz and 17.5 GHz at 0 V, -2 V and -4 V reverse biases, respectively.

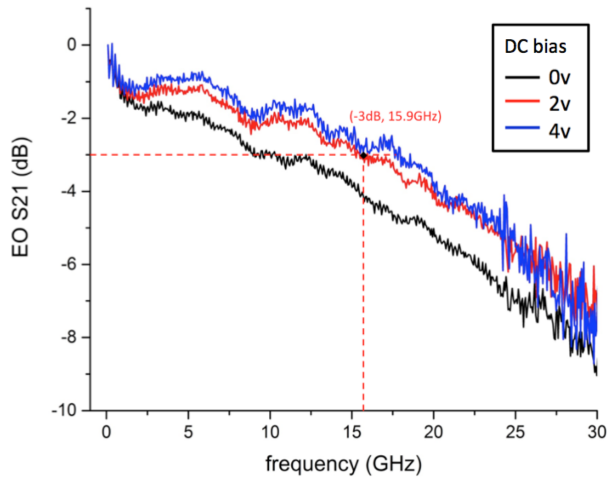

Figure 3.12: The normalized EO S21 response from the real single drive push-pull TWMZ modulator at different reverse biases.

3.3.4.3 Linearity Performance

The SFDR of the optical link using the silicon single drive push-pull modulator was measured by the two-tone method [18]. For comparison, we also measured the SFDR when the link used a $LiNbO_3$ modulator [76] with the same laser and photodetector to keep test system's noise level the same. In this way, the measured SFDR difference was due to the nonlinearity of the modulation process. The block diagram of the experimental setup is shown in Figure 3.13. A CW laser at 1555.41 nm was end firing to an erbium-doped fiber amplifier (EDFA, gain = 8.5 dB). The light was then sent to an optical tunable band-pass filter (BPF, insertion loss=1 dB) and a polarization controller before coupling into the modulator. RF signal generators created two sine-wave drive signals centered at f_1 (1 GHz) and f_2 (980 MHz). Band-pass filters centered at these frequencies were used to remove the testing system's inherent distortion. The two tones were sent to a high-speed power combiner to generate a single RF drive signal. By tuning the signal generator's output power, the device was driven by two signals that have equal power. The probing scheme was the same as described in Section 3.3.4.2. The TWMZ output optical signal was detected by the highly linear photodetector used in Section 3.3.4.2. The detector's output RF signals were sent to RF spectrum analyzer (Tektronix RSA6100A) to measure the linear and nonlinear component. The output optical power from the CW laser was about 13 dBm. The input RF power to the TWMZ was obtained using the signal generator output power, the loss of the RF filter and the loss of RF combiner (RF components' total loss was about 8.5 dB). The measured noise floor was about −160 dBm/Hz (Noise power was -140 dBm measured in a 100 Hz resolution bandwidth (RBW)).

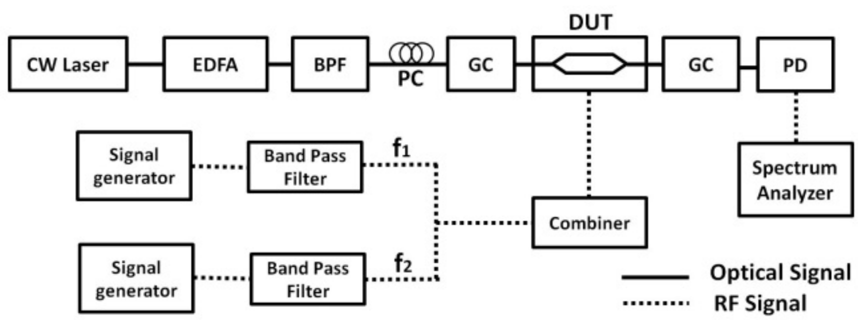

Figure 3.13: Block diagram of the two-tone measurement setup; PC: polarization controller, DUT: device under test; PD: photodetector.

In the following discussion, the dynamic ranges were all determined from the distortion products at $2f_1$-f_2=1.02 GHz and $2f_1$=2GHz (the distortion products at $2f_2$-f_1=0.96 GHz ($2f_2$=1.96 GHz) were within 0.5dB of the distortion products at 1.02 GHz (2 GHz)). For both Si and $LiNbO_3$ modulators, the measured output signal, IMD3 power, SHD power, and noise floor power in a one Hz bandwidth are shown in Figure

3.14. Straight-line fits were made to the measured signal and IMD3 (SHD) powers. The SFDR was found by subtracting the signal level from the noise level at the input power where the extrapolated IMD3 (SHD) power equaled the noise level. When the DC common bias was 2 V, IMD3 and SHD were 100.4 dB·Hz$^{2/3}$ and 90.6 dB·Hz$^{1/2}$, respectively.

The corresponding results of the $LiNbO_3$ modulator biased at quadrature were 95.1 dB·Hz$^{1/2}$ and 105.8 dB·Hz$^{2/3}$, respectively. For SHD and IMD3, our silicon modulator was about 5 dB less than the commercial $LiNbO_3$ modulator. The DC reverse bias' influence on linearity was also measured, shown in Table. 3.1. The highest linearity of our device was obtained at 2 V DC common bias. The linear fit to the IMD3 had a slope of approximately 3.2dB/dB, which suggested that the transfer curve was performing IMD3 cancellation up to almost the fifth power (See Appendix). This was consistent with analysis in [77] that showed that below saturation the IMD3 curve should be steeper than 3dB/dB slope. From experimental results shown in Fig.3.14, the power fits to an exponent are 1.03 dB/dB, 1.92 dB/dB for the fundamental and SHD components, which agree with the SFDR theory prediction of 1 dB/dB and 2 dB/dB.

Thus, this experiment has shown that a single drive push-pull scheme, with a tuned DC bias and optimized PN junction, can effectively suppress nonlinear distortion terms. In the future, we need to reduce optical link loss to have better SFDR. Thus, monolithically PICs were preferred to replace the discrete devices. Key active devices like on-chip laser [78] and photodetector [79] have been realized in the same platform.

Table 3.1: Compare the SFDR between our Si on-chip TWMZ modulator and commercial $LiNbO_3$ TWMZ modulator.

	Single-drive push-pull Si TWMZ modulator					$LiNbO_3$ modulator
DC Bias (V)	0	1	2	3	4	biased at quadrature
$SFDR_{IMD3}$ ($dB \cdot Hz^{2/3}$)	86.9	93.7	100.4	95.4	93.1	105.8
$SFDR_{SHD}$ ($dB \cdot Hz^{1/2}$)	80.2	88.7	90.6	88.1	85.4	95.1

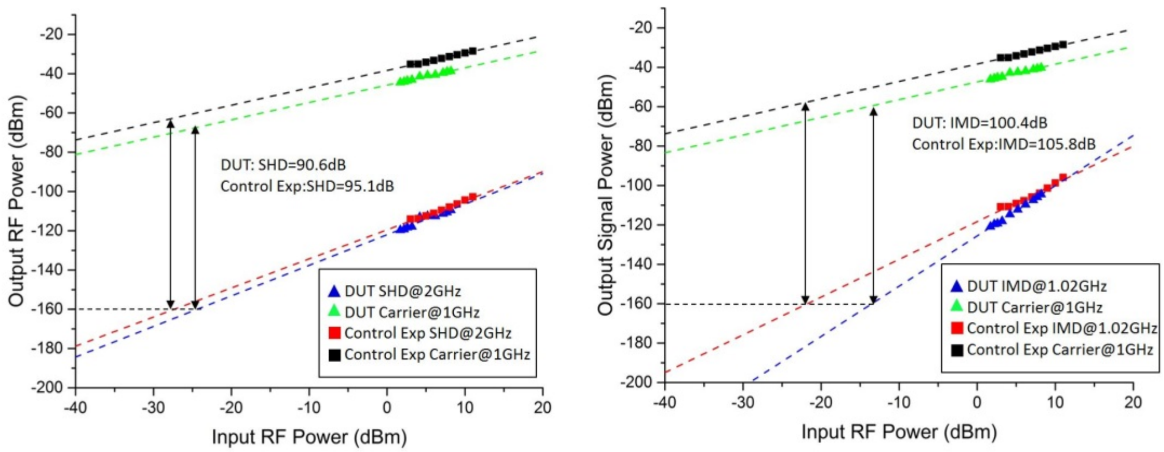

(a) (b)

Figure 3.14: Measured SFDR of the optical link with Si TWMZ modulator (marked as DUT) at -2V reverse bias or with a commercial $LiNbO_3$ modulator (marked as control experiment). Shot noise power in a one Hz bandwidth is shown on the black horizontal dashed lines. (a) The device output signal power and second-order harmonic at 2GHz versus input RF power (b) The device output signal and IMD3 at 1.02GHz versus input RF power.

3.3.4.4 Data Transmission Performance

We also demonstrated high-speed data transmission performance of the Si single drive push-pull TMMZ modulator. Eye-diagram measurements exhibited similar V_π as shown in Section 3.3.2. The measurement was set up as following. The PRBS (2^{31}-1) at 10 Gb/s was created by a pulse pattern generator. It was amplified by a 50 Ω modulator driver (Centellax™ 40 Gb/s driver). The drive signal was attenuated to the desired amplitude (4 V_{pp}) before being applied to the modulator. A DC bias was applied to modulator. The working wavelength, device probing method and RF termination configuration were the same as shown in Section 3.3.4.3.

When 4V_{pp} RF drive signal was applied, the maximum reverse bias on top and bottom arms' PN diodes were (V_{DC} ± 1V). The voltage swing range is 2V that is less than 0.5V_π. And considering the non-linearity in PN junction, the ER will be low as shown in Figure 3.15. We think the noise in Figure 3.15 (a) is due to several reasons. First, the fabrication non-uniformity could generate differences between top and bottom phase shifters, which broke our ideal identical devices assumptions. Second, there were high-resistance issues in the VIA fabrication. It may create the poor Ohm contact and impedance mismatch. Thirdly, RF probe contacts were not ideal in the real testing. Therefore, the RF modes' interference and the reflections in our device will cause the problem in the eye testing when the PN junctions had the minimum reverse bias voltage (0-2V) compared to other cases in Figure 3.15.

The eye diagram's ER improves with increasing DC bias. This is because the special working wavelength at 1555.42nm. From the tunability experimental results of the modulator as shown in Figure 3.15 (e), we can find bias points shown in green dots. When the DC bias increases from 0v to 4v, the slope of the MZI transfer function increases. The RF voltage swing range is the same (4V_{pp}) for all DC biases. So eye diagram's ER will increase. And, at the same time, the bias point is moving away from quadrature and compressing the zero level into the minimum of the MZI transfer function as shown in Figure 3.15 (d). The eye-diagram ER was 5.5 dB at 2 V DC bias. The one-level insertion loss was about 3.2dB at 2V DC bias. And other one-level losses are about 1.2dB, 4.6dB and 7.2dB at 1V, 3V and 4V DC biases respectively. At an impedance of 50 Ω, an ideal 4 V_{pp} NRZ RF driving signal centered on 0 V carries 40 mW of power, which in turn implies an energy consumption of 4 pj/bit at 10 Gb/s. With these parameters we could have a general view of the modulation performances. Due to the availability of test equipment, only 10Gb/s operation was demonstrated, although we expected the device to be capable of passing higher data rate bit (>25Gb/s) streams based on EO bandwidth test results.

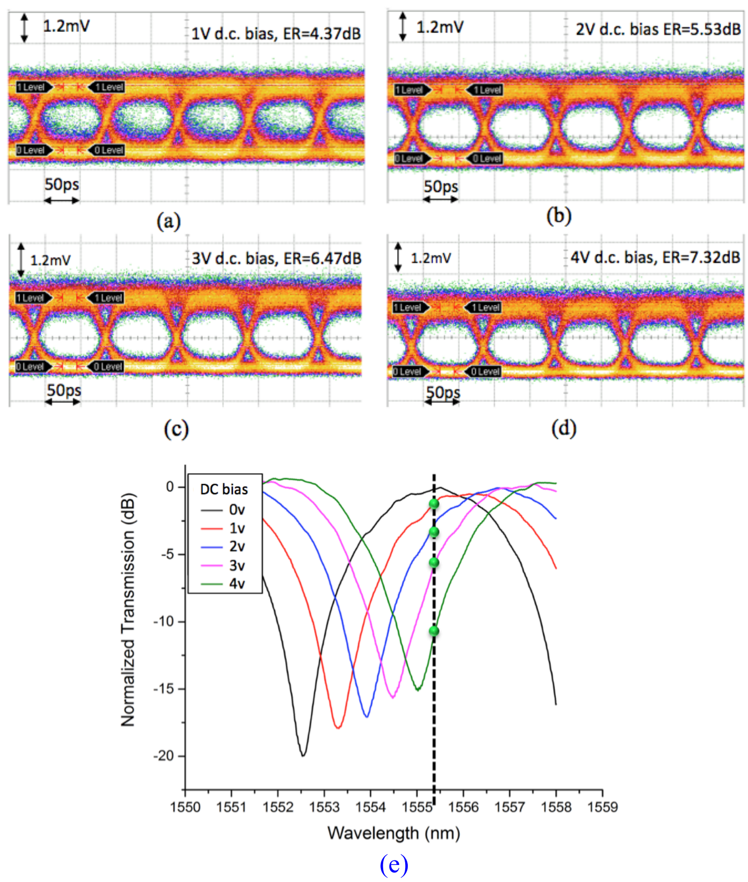

Figure 3.15: (a-d): The silicon TWMZ modulator's electrical eye-diagram at 10 Gb/s with 4 V_{pp} driving voltage at different reverse biases; (e) the tunability and bias points (green dots) of the silicon modulator in the eye-diagram measurement. Spectrum is normalized with the max output power of MZM at 0v bias. Working wavelength is shown by dashed line.

3.4 Summary

The author designed a nonlinear phase shifter for the optical phase modulator applied in our non-reciprocal system. The phase shifter can improve the non-reciprocal system's robustness in the face of RF driving voltage's variation. We fabricated the phase shifter in the silicon photonic platform and verified its characteristics by the experiment. The author also designed a high-linear silicon TWMZ modulator with single drive push-pull structures. An intermodulation distortion of 100.4 $dB \cdot Hz^{2/3}$ and a second harmonic distortion of 90.6 $dB \cdot Hz^{1/2}$ were measured at -2V reverse bias. This device's SFDR performance had about a 5 dB gap compared to a commercial $LiNbO_3$ modulator. The device's modulation efficiency ($V_\pi \cdot L_\pi$) was about 2.2 $V \cdot cm$. Nearly 16 GHz EO 3dB bandwidth and 10 Gb/s eye-diagram were measured.

Chapter 4

COHERENCE LENGTH IN SILICON PHOTONIC PLATFORM

In this chapter, the author's contribution is finding, for the first time, the typical coherence length of silicon waveguides fabricated in a CMOS compatible silicon photonic MPW run. The author proposes a new analyzing method to verify phase coherence length model and designs the experiment to extract the coherence length that shows the relationship between the waveguide output random phase variance and the waveguide length. The coherence lengths were 4.17 ± 0.42 mm and 1.61 ± 0.12 mm for silicon strip and rib waveguides respectively with statistical significance. We hope to use the coherence length as a figure of merit to evaluate the fabrication non-uniformity.

4.1 Introduction

Like other complex PIC systems, one big challenge of our silicon on-chip non-reciprocal system is to realize accurate phase control by using integrated optical components that have high uniformity. Reliable fabrication processes and PDKs are critical to provide the infrastructure for the manufacture of practical, competitive PICs in silicon [80]. However, the current situation is not satisfactory [81]. The bottleneck is the fabrication non-uniformity that results in fluctuations in waveguide's effective index. The issue creates large phase uncertainty that makes the peak resonant wavelength of resonators hard to predict [8, 41, 82, 84, 85]. Thus, extra power as well as development effort for control systems will be spent on the tuning of these devices' resonance positions. But this is undesirable in power budget limited scenarios [41, 82, 83, 86].

The phase coherence length is a key parameter to characterize these fabrication non-uniformities. Traditionally, the phase coherence length (we refer "coherence length" for short) was used to characterize the phase noise level of a laser in interferometric measurements. In brief, if the interferometer's path-length difference is larger than the coherence length, the interferometer's screen will not show the pronounced interference fringes as shown in Figure 4.1. The exact definition of coherence length will be given in the next section.

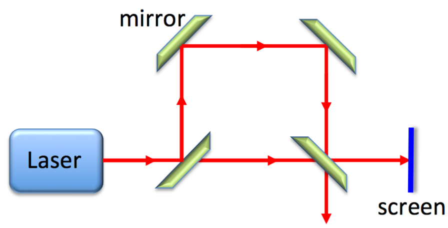

Figure 4.1: Setup of an interferometer to measure the coherence length of a laser.

The coherence length was then applied to study the phase noise of low confinement non-silicon waveguides. For instance, typical fiber Bragg grating's coherence length is about 10-100cm [43] and the silica channel waveguide coherence length is about 27m [42]. However, former coherence length reports in integrated optics didn't show large statistical significance as they were extracted from small numbers of samples due to fabrication and test limitations [42, 43, 87].

To the best of our knowledge, the coherence length has not yet been reported in silicon photonic waveguides. This is because analyzing coherence length requires a large amount of data from special designed interferometer structures across the entire wafer. Unlike many researchers [42, 43, 87, 88] in silicon photonics, the author had access to a complete Si photonics wafer from a commercial foundry. This provides a unique opportunity to take the extensive cross-wafer data set needed to accurately measure the coherence length. Developing reliable statistical methods to measure random phase is another challenge. Researchers have made great progress by stitching a hundred scanning electron microscope (SEM) images of one waveguide to quantify phase noise in integrated silicon Bragg gratings [88], but the cost would be high if hundreds of devices are characterized using SEM.

In this dissertation, more than 800 silicon MZIs in clusters were automatically measured across the wafer. The MZIs' spectra clearly show fabrication non-uniformity similar to previous work on non-uniformity of micro ring resonators [41, 82, 84]. Moreover, the coherence length extracted from MZIs shows the relationship between the waveguide's random phase variance and the waveguide length. With rings, this relationship is less obvious, because of the small device footprint. We find the coherence lengths are 4.17 ± 0.42 mm and 1.61 ± 0.12 mm for silicon strip and rib waveguides respectively. We hope to use the coherence length as a standard figure of merit to evaluate the fabrication non-uniformity to support system level integration efforts in silicon photonics.

4.2 Theory

4.2.1 Effective Index and Physical Variations

In this work, we study the coherence length of the strip waveguide and the rib waveguide as shown in Figure 4.2. The input optical wavelength was 1550 nm. The effective index of the waveguides will change due to variations in waveguide thickness (t), width (w), sidewall angle (α) and slab layer thickness (s). The relationships between effective index and physical variations can be considered to be linear if the variations satisfy that δt<10nm, δw<10nm, δs<10nm and δα<10° as shown in Figure 4.3. The proportionality constants that link geometries to the effective index are defined as C_w, C_t, C_α and C_s. They were simulated by a finite element mode solver [59] and summarized in Table. 4.1. We found that the effective index was very sensitive to the silicon layer thickness and sidewall angle. The effective index of the rib waveguide is less sensitive to sidewall angle as compared to the strip waveguide.

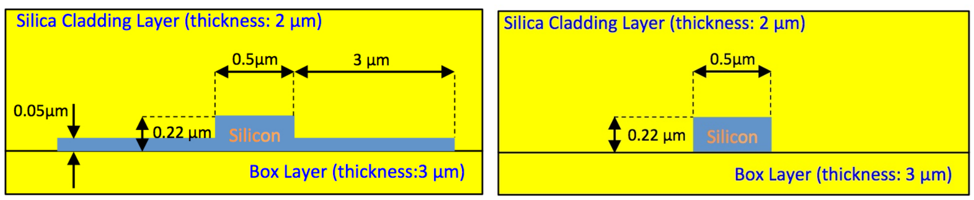

(a) (b)

Figure 4.2: Cross-sections of two kinds of waveguides used to build MZIs: (a) the rib waveguide; (b) the strip waveguide.

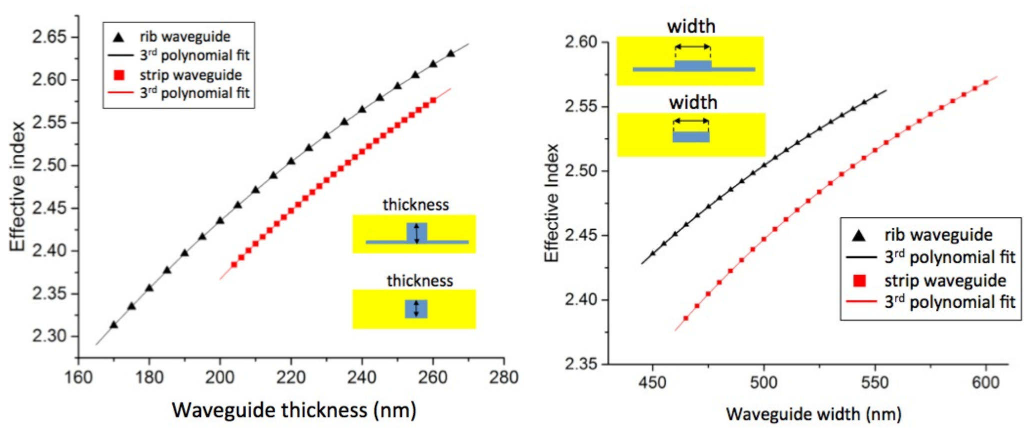

(a) (b)

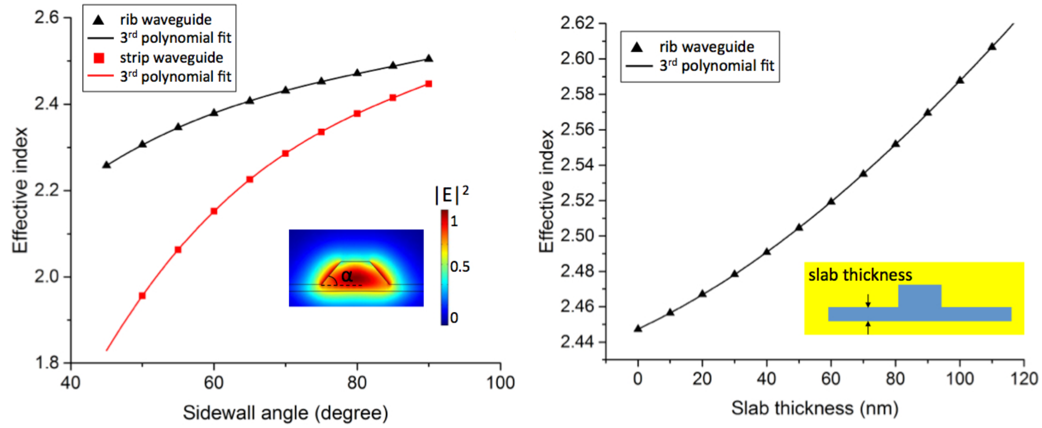

Figure 4.3: The relationship between the waveguide geometry and the effective index. The geometry parameters are (a) waveguide thickness, (b) waveguide width, (c) sidewall angle and (d) slab layer thickness. The inset figures show the definition of the geometry parameters. In (c), the inset figure also shows the mode profile when the sidewall angle is 45º. Default geometry parameters are the same as shown in Figure 4.2. Input wavelength is 1550nm.

Table 4.1: The proportionality constants, linking the waveguide width, thickness, sidewall angle and slab height variations to an effective index variation.

	C_t (nm^{-1})	C_w (nm^{-1})	C_α (degree^{-1})	C_s (nm^{-1}).
strip waveguide	3.7×10^{-3}	1.6×10^{-3}	6.9×10^{-3}	NA
rib waveguide	3.2×10^{-3}	1.2×10^{-3}	3.5×10^{-3}	1.4×10^{-3}

4.2.2 Phase Noise Model

The vertical variations are coming from the wafer top silicon layer thickness non-uniformity and etching process. The thickness can vary up to ± 20 nm between wafers [80] even before the wafer processing begins. The lateral variations of waveguides are coming from sidewall roughness created during the etching process. The etching processes are dependent on foundry tools. Standard 248 nm lithography CMOS processes are used in the fabrication of the samples, but there are uncertainties in the photoresist thickness or roughness, mask alignment positions, the developing speed, the silicon dry etching rate and the thermal oxidation growth speed. Therefore, a lot of random factors contribute to the change of effective index and the accumulated output phase of the waveguide is assumed to have a zero-centered random variable that undergoes a random walk under Gaussian distribution. The randomly introduced phase noises are assumed to be independent and based on the central limit theorem [42].

4.2.3 Coherence Length Model

The coherence length characterizes the physical phenomena that when the waveguide's length (L) is equal to the coherence length (L_{coh}), the random noise phase ($\Delta\phi\ (L)$: Gaussian random variable, with zero average) inside the waveguide as a result of fabrication non-uniformity will cause signal phase vary in a certain range. The average deviation range is expressed as $<e^{i\Delta\phi(L=Lcoh)}> =e^{-1}$ following the community's tradition. In other words, the random phase noise's standard deviation is $(2L/L_{coh})^{1/2}$ for the waveguide of length L. If we use the waveguide to build interferometers like rings (perimeter=L_{coh}) and MZIs (unbalanced arm length=L_{coh}), the average difference in resonant wavelength between two as fabricated interferometers will be $\pm FSR\times\Delta\phi\ (L_{coh})/2\pi \approx \pm 0.11\times FSR$. The theory predicts that the random phase noise variances increase linearly with the waveguide length if the coherence length is constant.

In order to calculate the coherence length, we propose a new method to extract optical phase noise from unbalanced MZIs. Although each MZI's waveguide has a different overall effective index after real fabrication processes, we can assume the average effective index ($<n_{eff}>$) to be same for the same type of MZIs. Then for the i-

th MZI of the same type, the effective index can be expressed as a function of position (x):

$$n_{eff,i}(x) = < n_{eff} > + \Delta n_{eff,i}(x), \quad (4.1)$$

where $\Delta n_{eff,\,i}$ (x) is a random deviation of effective index from its average value at the position x with Gaussian distribution centered at zero. The destructive interference condition of a MZI can be written as below:

$$\frac{2\pi}{\lambda}\int_0^{dL} n_{eff}(x)dx = (2m+1)\pi, \quad (4.2)$$

where dL is the length difference between two arms of the MZI; m is an integer standing for the MZI azimuthal mode index; n_{eff} (x) is the effective index of fundamental mode at position x; λ is the input optical wavelength. The destructive interference condition can be re-written as below:

$$\frac{2\pi}{\lambda} < n_{eff} > dL + \Delta\phi_i(dL) = (2m+1)\pi, \quad (4.3\text{-a})$$

$$\Delta\phi_i(dL) = \frac{2\pi}{\lambda}\int_0^{dL} \Delta n_{eff,i}(x)dx \ . \quad (4.3\text{-b})$$

Although ideally Eq. (4.3-b) should be written:

$$\Delta\phi_i(dL) = \frac{2\pi}{\lambda}\int_0^{L_1+L_2} \Delta n_{eff,i}(x)dx \ . \quad (4.3\text{-b'})$$

Since every slice (dx) of waveguide in both MZI arms (L_1 and L_2 are arm lengths and $L_1<L_2$) contributes to the phase error, Eq. (4.3-b) is a good approximation when $dL >> L_1$ or $L_1 << L_{coh}$, which is the discussed based on our MZI test structures (see Appendix A.3). Another reason to use Eq. (4.3-b) is that, when two waveguides are placed close (as shown in the GDS layout in Figure 4.4 (c)'s inset, distance (x)< 700 μm), they become statistically correlated in terms of fabrication (see Appendix

A.3). We then calculate the effective index dispersion slope (k) by a mode solver [59] in order to find the mean of effective index at the wavelength of interest.

$$k = \frac{d<n_{eff}>}{d\lambda} \ . \tag{4.4}$$

We simulated that k=-1.13×10^{-3} nm^{-1} and -9.81×10^{-4} nm^{-1} for strip and rib waveguides respectively. From the MZI spectrum, we measured the FSR and the corresponding resonant wavelengths. Next, we can calculate the average effective index ($<n_{eff}(\lambda_1)>$) by the following formula:

$$\frac{2\pi}{\lambda_1} < \mathrm{n_{eff}}(\lambda_1) > \mathrm{dL} - \frac{2\pi}{\lambda_2} < \mathrm{n_{eff}}(\lambda_2) > \mathrm{dL} = 2\pi \, , \tag{4.5-a}$$

$$\frac{2\pi}{\lambda_1} < n_{eff}(\lambda_1) > dL - \frac{2\pi}{\lambda_2} < n_{eff}(\lambda_1 + k \cdot FSR) > dL = 2\pi \, , \tag{4.5-b}$$

where λ_1 and λ_2 are adjacent resonant wavelengths ($\lambda_1 < \lambda_2$). The interferometer's azimuthal mode m is estimated by the method in [84]. That is, using measured resonant wavelength (λ_i), FSR and dL to extract group index (n_g) by:

$$\mathrm{FSR} = \frac{\lambda_1 \lambda_2}{n_g dL} \ . \tag{4.6}$$

Then we can determine the m from the closely gathered cluster in the scatter plotting of (λ_i,n_g) as shown in Figure 4.4 (d). Substituting MZI$_i$'s $<n_{eff}(\lambda_1)>$ and m into Eq. (4.3-a), we get the random phase shift $\Delta\phi_i\,(dL)$. Finally, we can calculate the coherence length (L_{coh}) from the linear regression of the variance ($<\Delta\phi_i(dL)^2>$) and dL. The relationship is shown as:

$$< \Delta\phi(L)^2 >= \frac{2L}{L_{coh}} \ . \tag{4.7}$$

In the author's method, L is replaced by dL in Eq. (4.7).

4.3 Experiment and Discussion

In this dissertation, the MZIs were fabricated by BAE Systems™ [89] through an UD OpSIS MPW run with 248 nm lithography. The devices were built on a 6" SOI wafer from SOITEC™ with 220 nm top silicon, 3 μm buried oxide layer with 10 Ω-substrate [90]. The MZIs were made using waveguide geometries shown in Figure 4.2. In the measurement, a linearly TE polarized light beam from a tunable laser (Agilent™ 81980A) centered at a wavelength around of 1550 nm was coupled into the MZI through a fiber array and an on-chip GC. The MZI's output light was coupled out through another GC to the fiber array and measured by a lightwave multimeter (Agilent™ 8163B) as shown in Figure 4.4. The measured spectra were normalized against the transmission of a reference GC loop connected by the same length waveguide. We tracked each resonant wavelength in the spectra of a set of MZIs by sine square function curve fitting [91]. For example, spectra of strip MZIs with dL = 144 μm are shown in Figure 4.4 (c). The azimuthal mode m is determined by the scatter plot of group index and resonant wavelength as shown in Figure 4.4 (d).

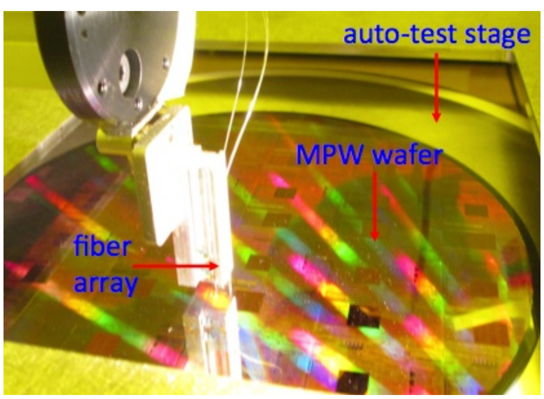

(a)

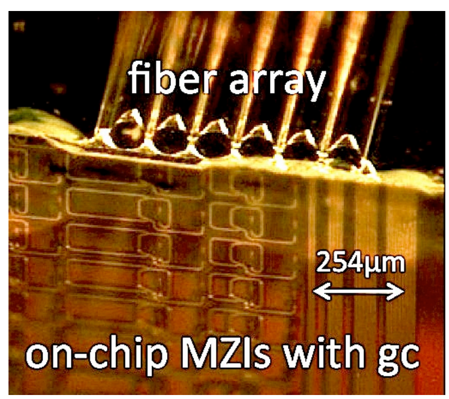

(b)

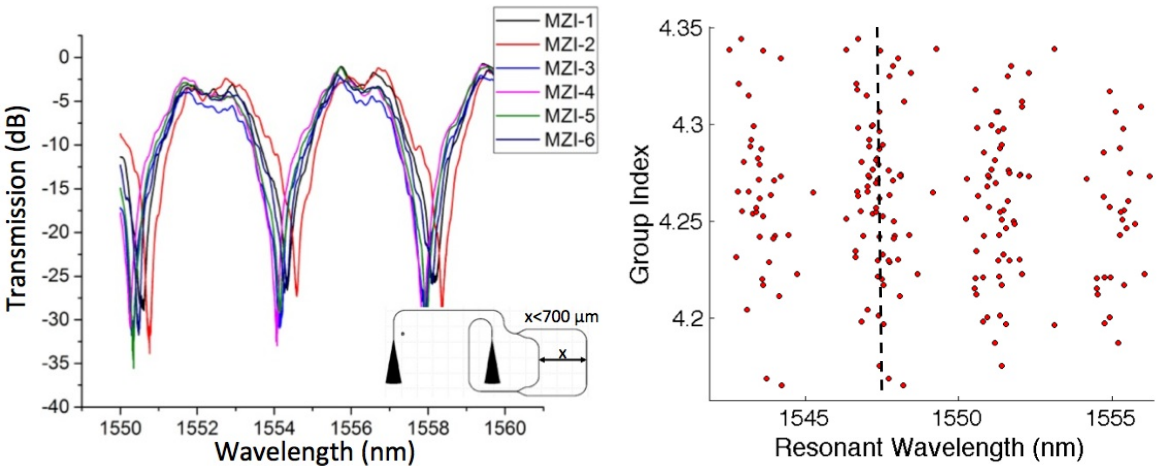

(c) (d)

Figure 4.4: Automatic wafer-scale test setup and measured of MZI spectra: (a) the photograph of wafer-scale auto-test setup with a 6" MPW loaded and (b) zoom in on-chip devices and a fiber array. (c) Transmission spectra (unit: dB) of six nominally identical MZIs in the same die. Device layout is shown in the inset. Plotting only shows 6 samples among 100 same designed MZIs (*dL*=144µm) in one die. (d) Extracted group index versus the resonant wavelength for MZIs (*dL*=144µm) in one die (about 100 samples). The mode selected from the line has the same azimuthal mode *m*.

We studied five groups of MZIs in each die (area size: 2.5 × 3.2 cm^2). Each group had a different *dL* and included 20 nominally identical MZIs that were spaced 120 µm apart as shown in Figure 4.4 (b). The *dLs* are 50 µm, 144 µm, 444 µm, 744 µm and 1044 µm. The transmission spectra of 800 MZIs from 8 dies across the wafer were measured to guarantee statistical significance. Based on the analysis method described in the section 4.2, we found that the coherence lengths of the strip and rib waveguides across the wafer were 4.17 ± 0.42 mm and 1.61 ± 0.12 mm, respectively. The linear regressions of $<\Delta\phi\ (dL)^2>$ and *dL* are shown in the Figure 4.5. We also did statistical T-test to verify the linear relationship as shown in Fig. 4(a, c). T-test is used because the degree of freedom is as small as 4 as we characterized 5 types of *dL*s. Calculated by the experimental data shown in Fig. 4 (a, c), T value proves that the relationship of Eq. (7) for both rib and strip MZIs have statistical significance. The type-I error's α level is smaller than 0.1%.

The strip waveguide's coherence length is longer than the rib waveguide's, which indicates that the fabrication process for the strip waveguide has better tolerance to process variations. Both waveguides have same waveguide width (500 nm) and the fundamental optical mode was highly confined in the center of the waveguide based simulation results. So it can be assumed that the top surface roughness is approximately same. It's clear that the rib waveguide has larger overall non-uniformity due to the additional slab layer. The extra phase error of the rib waveguide could mainly suffer from the partial etch step that forms the slab layer. Different mechanisms of fabrications uncertainties have been studied by others, including etching, mask aligning, and oxidation step errors. For example, some reports showed that the waveguide sidewall roughness was about ± 1.8 nm [88] and the waveguide top surfaces roughness was about ± 0.45 nm [92]. The thickness and width variations of slab layer of rib waveguide in one die were about ± 0.1 nm and ± 0.4 nm [82]. Compared with the strip waveguide, the rib waveguide has larger non-uniformity in the slab layer fabrication. Although these results came from dedicated runs, they could qualitatively show that slab layer variations degrade the phase noise performance indicated by shorter coherence length.

We randomly generated 10000 MZIs with slab thicknesses that is a Gaussian random variable centered at 50 nm. The standard deviation was set as 0.25 nm. Each waveguide's effective index at different wavelength was simulated [59]. Using Monte-Carlo numerical method, we found MZIs resonant wavelengths near 1550 nm under the same azimuthal mode m. The simulated phase noise variance as a function of dL is shown in the appendix. From Figure 4.5(e), coherence length was extracted as 1.8 mm that agreed very well with the experimental results (1.6 mm). Thus, our coherence length model is proved by both simulation and experiments. Moreover, 0.25nm is also a reasonable prediction [82] for the standard deviation of slab thickness. Thus, our method opens a path to characterize fabrication non-uniformity without using SEM test. The measured coherence length is shorter than the simulation because other non-uniformities' influences such as the waveguide thickness, width and sidewall roughness. In this work, we provide a wafer scale variation of coherence length since our major goal is to analyze the wafer level fabrication non-uniformities. The small deviation of coherence length across the wafer proves the high uniformity. Depending on the applications, die scale variation may be more important than wafer scale [43, 87]. Therefore, we provide a simple but general analyzing method that can extract the coherence length under different scales.

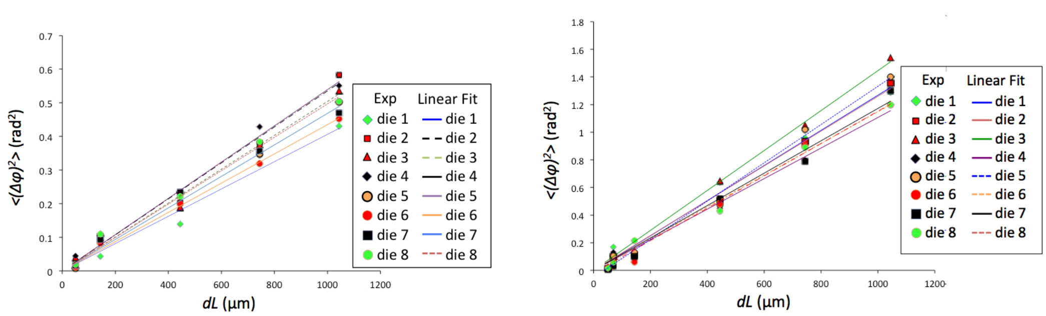

(a) (b)

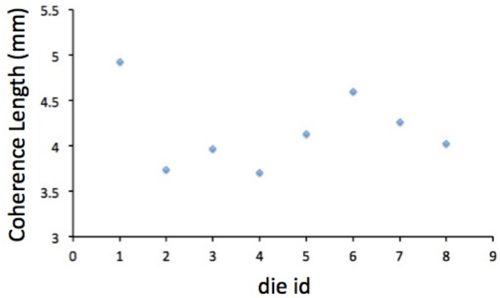

(c)

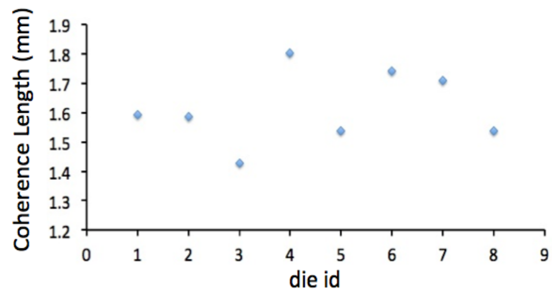

(d)

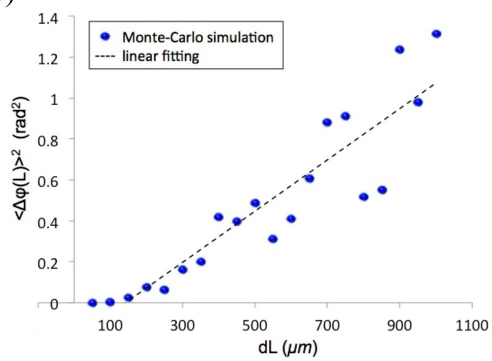

(e)

Figure 4.5: Coherence length measurement results: (a/b) the relationship between the strip/rib MZI's unbalanced arm length and the variances of random phase shifts; (c/d) the statistics of the coherence length of strip/rib waveguide in 8 dies across the wafer. (e)The Monte-Carlo simulation of phase noise variance for rib MZI. The rib waveguide's slab thickness' standard deviation is 0.25nm

Since the fabrication non-uniformity may bring extra loss to waveguide, we measured waveguide insertion loss to study whether it was related to the phase coherence length. We fitted each measured GC loop (connected by waveguide of different length) spectrum with parabola in a 40 nm range centered at its peak wavelength. The insertion loss obtained from linear regression between waveguide length and maximum power at around 1550nm is -4.8 ± 0.03 dB/cm and −5.2 ± 0.06 dB/cm for the strip waveguide and the rib waveguide, respectively, as shown in Figure 4.6. Lower insertion loss could be attributed to the better sidewall roughness in strip waveguide but the difference is only 0.4 dB, which shows that the low insertion loss and the long coherence length are not strongly related. The author thinks one reason is that the insertion loss reflects the averaged random phase-shift variance contributed by all fabrication non-uniformities, but the coherence length stands for the total sum of variance as a result of all non-uniformities.

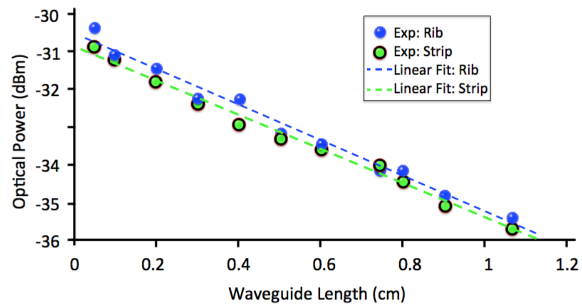

Figure 4.6: Relationship between the output power and the waveguide length.

Compared with the reported coherence lengths of fiber device and silica waveguide [42, 43, 87], the coherence length of silicon waveguide is several orders of magnitude shorter. Note that the index contrast of silicon waveguide is much larger than others. Near 1550nm, silicon and silica refractive index are 3.47 and 1.45 respectively. Moreover, the uncertainty of the silicon thickness is high [89]. Therefore, The author thinks the shorter coherence length is likely due to the high-index-contrast highly confined waveguide. The effective index is very sensitive to geometry changes as shown in Figure 4.3

To show the fabrication non-uniformity, we also measured destructive resonant wavelengths and FSRs contours of MZIs (dL=144 μm, strip waveguide and rib waveguide) across the wafer as shown in Figure 4.7 and 4.8. Twenty nominally identical samples were measured in each MZI set. With statistical significance, FSRs are 3.938 ± 0.014 nm (strip waveguide) and 4.191 ± 0.084 nm (rib waveguide), respectively. Peak resonant wavelengths are 1548.409 ± 0.712 nm (strip waveguide) and 1548.806 ± 0.988 nm (rib waveguide), respectively. Then we can calculate group index (n_g) by Eq. (4.6). We found n_g=4.2 and 4.0 for strip and rib waveguides respectively. We can also calculate the group indices in another way by Eq. (4.4) and Eq. (4.8). We found they were 4.2 and 3.9. Good agreement between theory and experiment is observed.

$$n_g = n_{eff}(\lambda) - \lambda \frac{dn_{eff}}{d\lambda} = n_{eff}(\lambda) - k\lambda \ . \tag{4.8}$$

For each MZI, the peak resonant wavelengths were picked up under the same azimuthal mode index. The rib waveguide's resonant wavelength random shift is larger than the strip waveguide's, which is consistent with our coherence length analysis. Although the standard deviation of resonant wavelength shift is about ten times larger than the FSR's, which is consistent with the reports in [82], a long coherence length guarantees that the output phase is still under well control.

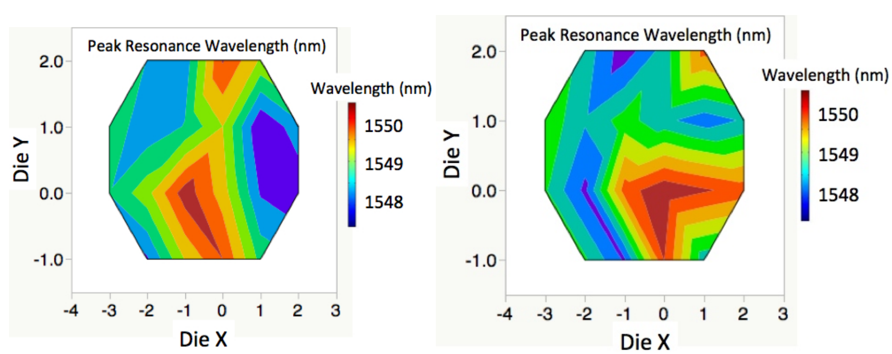

(a) (b)

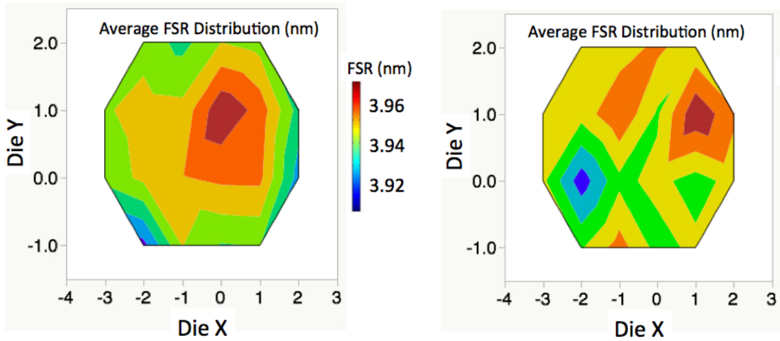

(c) (d)

Figure 4.7: Cross-wafer measurement of strip/rib MZIs (dL=144µm): (a/b) strip / rib MZIs' resonant wavelengths; (c/d) strip / rib MZIs' FSRs

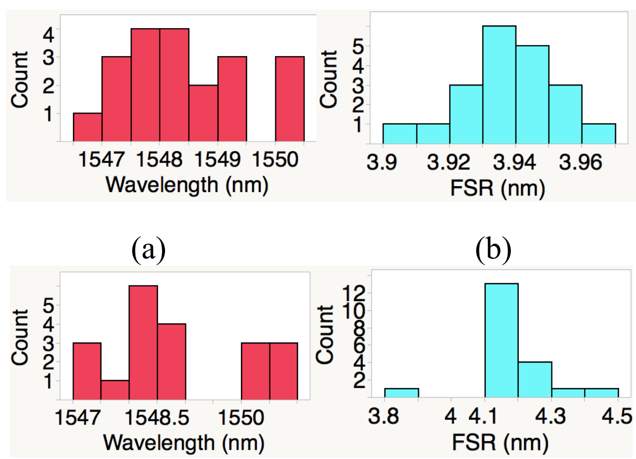

(a) (b)

(c) (d)

Figure 4.8: Histograms of the strip and rib MZIs' (dL=144µm) resonant wavelengths and FSRs across the wafer: (a) strip MZI's resonant wavelengths; (b) strip MZI's FSRs; (c) rib MZI's resonant wavelengths (d) rib MZI's FSRs. Each count stands for one die's average value.

4.4 Coherence Length Validation and Application

We also use other published experimental results to verify the coherence length measurements in this work. In [84], researchers tested 371 racetrack resonators that were made by strip waveguides as shown in Figure 4.2 (b). The devices from [84] were also fabricated by a commercial CMOS MPW foundry. Thus, we can assume our strip waveguide's coherence length can be applied in [84]. In [84], when the device separation distance (this is equivalent to dL in our model) is 1mm, the resonant wavelength average shift (<Δλ>) was about 0.75 nm as shown in [84]'s Figure 3 (b). The racetrack resonator's perimeter was 84.36 μm and FSR was about 6.8 nm at around 1550nm. Therefore, the phase noise's standard deviation is 0.69 rad calculated by 2π×<Δλ>/FSR. By our coherence length method, substituting strip waveguide's L_{coh}=4mm and dL=1mm, we find the phase noise's standard deviation is $(2dL/L_{coh})^{1/2}$=0.71 rad. Therefore, [84]'s experimental results can be successfully predicted by our coherence length theory model. In general, coherence lengths may vary among different MPW runs.

The coherence length theory can be applied in PIC system design. For example, considering an on-chip non-reciprocal system's 4 cm long delay line made by strip waveguide as shown in Figure 4.2 (b), we can find the standard deviation of random phase shift to be 4.47 rad by Eq. (4.7). The equivalent waveguide length uncertainty's standard deviation is:

$$\Delta L_{eff} = \frac{\Delta\phi(dL)}{2\pi}\frac{\lambda}{n_{eff}}. \tag{4.9}$$

Then we can calculate the time uncertainty by

$$\Delta t = \frac{\Delta L_{eff}}{c/n_{eff}}. \tag{4.10}$$

Therefore, the uncertainty in time domain due to phase coherence length (assume n_{eff}=2.5) is about 3.7 fs.

4.5 Summary

The author extracted the phase coherence lengths in the silicon photonics platform for the first time. The measured coherence lengths were 4.17 ± 0.42 mm and 1.61 ± 0.12 mm for strip and rib waveguides, respectively. These results show statistical significance and high consistence based on large amount of samples of MZIs across the wafer. The strip waveguide has better fabrication tolerance than the rib waveguide. The coherence length was not strongly correlated to the waveguide insertion loss. Moreover, the coherence length method can be applied to other researchers' work related to silicon photonics fabrications. There is a good agreement between theory and experiment. This work provides both theoretical and experimental supports of using the coherence length as a guideline to design PICs.

Chapter 5

DIRECTIONAL COUPLER

5.1 Introduction

Directional coupler is a significant passive building block in our time-dependent non-reciprocal system. In this chapter, the author’s contribution is the low loss directional coupler with high yield performance. The device has been used as PDK in our silicon photonic platform for wide applications. In addition to the non-reciprocal system, it is also widely used in WDM multiplexer (MUX) [8], optical phase array transceiver [93], and on-chip quantum optics [94]. Moreover, the author’s work contributes to a reliable fabrication error model for the silicon photonic platform based on the directional coupler's experimental results.

5.2 Design Method

Directional coupling can be achieved by bringing two optical waveguides into proximity, so that the evanescent tails of both waveguide modes overlap. This overlap will then lead to a gradual coupling of the optical mode from one waveguide to another. The design layout of the current directional coupler is shown in Figure 5.1. The layout and key parameters of symmetric directional coupler made by strip/rib waveguide are shown in Figure 5.1 (a). L is coupling length. The gap is the separation between two waveguides in the coupling region. The I/O waveguide is bend waveguide that is connected by two arcs with same radius R. For simplicity, we refer them as strip directional coupler and rib directional coupler. The accurate modeling of the power distribution of the propagation mode between the two waveguides in the coupling region is comprehensively studied by couple mode theory using perturbation method [91].

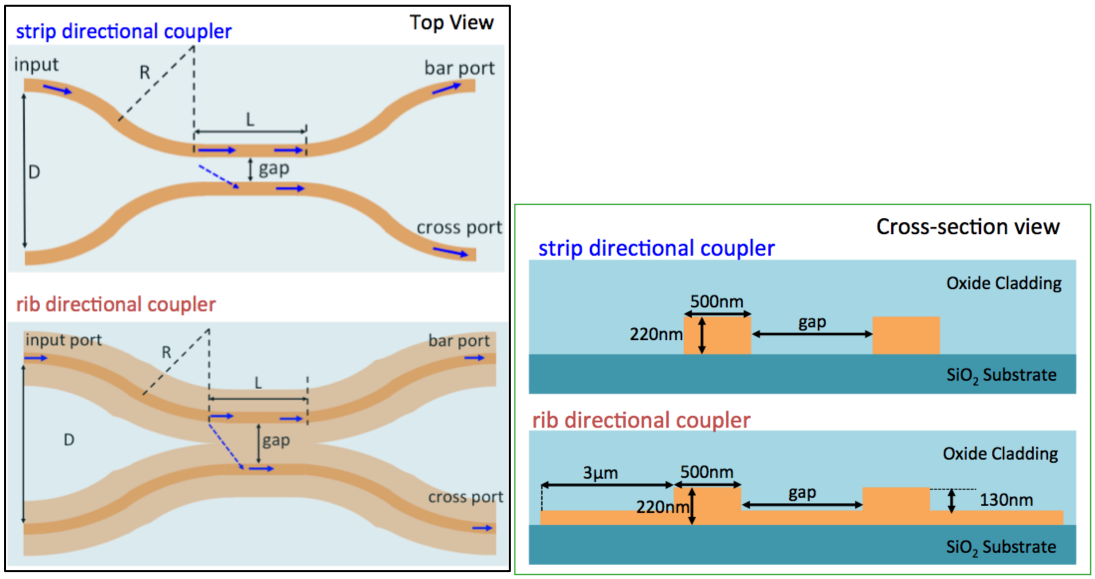

(a) (b)

Figure 5.1: Schematics of silicon directional couplers working at 1550nm. (a) The top view of strip and rib directional couplers. (b) The cross-section view of strip and rib directional couplers in the coupling regions. The waveguide is made by silicon.

The I/O bend waveguide's total length and bend radius were carefully selected in order to reduce the insertion loss and footprint. To study the bend loss, we designed the bend structures as shown in Figure 5.2. The bend waveguide was made by strip waveguide as shown in Figure 4.2 (b). That is, w=500 nm, h=220nm. We simulated the total modes and the fundamental mode bend losses at different bend radius (R) by 3D-FDTD [95].

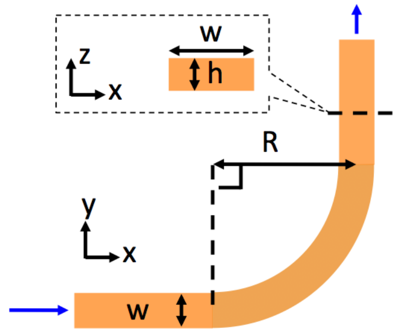

Figure 5.2: The top-view of the bend strip waveguide. w: waveguide width; h: waveguide height; bend angle: 90°; R: bend radius; input/output lead waveguide length: 1μm.

Two power monitors were placed in X-Z and Y-Z plane at the input and output ports respectively. We launched a TE_0 fundamental mode into the waveguide. Both monitors' size was 2.5×2.5 μm^2 because 2.5 μm was larger than 5w or 5h. The FDTD mesh gird size was λ/200 that was ten times of the algorithm normal requirement (λ/20). And the stable bend waveguide loss was obtained as shown in Figure 5.3. Both the total output power and TE fundamental mode power were measured by mode expansion [95]. When bend radius (R) increases, the bend loss decreases as shown in Figure 5.4. The bend loss of fundamental mode is reduced to 0.07 dB when the bend radius is 3 μm.

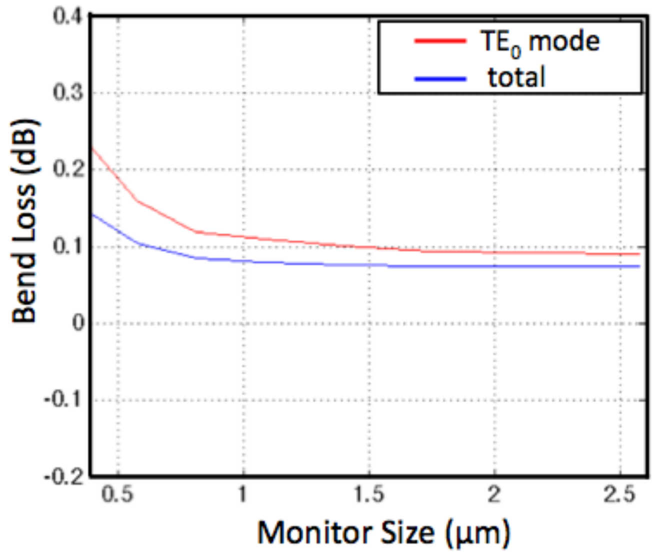

Figure 5.3: FDTD power monitor size's influence on the simulation. The square monitor's size is defined by its side length. Bend radius=2 μm, bend angle=90°.

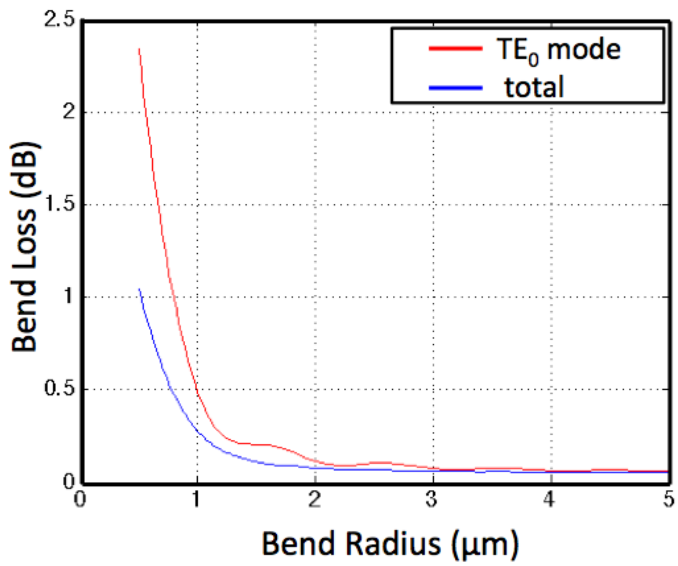

Figure 5.4: The loss of a 90° bend waveguide at different radius.

Based on the simulation of bend loss, we made a conservative choice for the bend radius as 15~20 μm for the directional coupler's I/O waveguide. The level of coupling between the two waveguides can be predicted to take the following form in the ideal case:

$$P_{bar}(L) = \left(cos\left(\pi L/(2L_c)\right)^2\right) \tag{5.1}$$

P_{bar} is the power ratio that remains in the bar waveguide. L_c is called "critical coupling length" which means the total power is coupled into the cross port at this coupling length. However, for a realistic directional coupler, some coupling will occur even if the length is made precisely zero, due to the fact that the waveguides need to be brought together in a gradual curve. We therefore will utilize the adjusted model:

$$P_{bar}(L) = (cos(\kappa L + \phi)^2)\ . \tag{5.2}$$

Similarly, the power that couples to the opposing waveguide can be modeled by:

$$P_{cross}(L) = (sin(\kappa L + \phi)^2)\ . \tag{5.3}$$

We don't consider the excess loss when analyzing the symmetric directional coupler's 50% coupling length (L_{50}). Coupling ratio (R) is defined as the power that couples into the cross port when the output power is normalized by the input power. We need to test devices with different *Ls*. Then we can fit the coupling length and coupling power by Eq. (5.2) and (5.3). Finally, we extract L_c , κ and ϕ, which can be used to calculate the coupling ratio at any coupling length.

There are three types of gaps in our design, which are 0.2um, 0.25um and 0.3um. There are two types of waveguides, which are rib and strip waveguides as shown in Figure 5.1. Among several different combinations, our goal is to select a reliable 50/50 directional coupler with small footprint and low loss. "Reliable" means the performance of coupler is consistent across the wafer and close to the simulation. Before fabrication, we simulated the L_{50} of different directional couplers by 3D FDTD. The gap separation, coupling length (L) and bend radius (R) were tuned to optimize the loss and footprint. Fundamental TE_0 mode at 1550nm was launched into the single mode waveguide. The output power at cross and bar port was monitored, which was normalized by the input power. The simulation results are shown in the Table 5.1. Learning from the blue parts in the table, we selected $\lambda/40$ as the FDTD mesh size in the coupling region and 3rd level mesh accuracy [95] in other parts, which guaranteed the fast simulation to obtain stable numerical results. Take one directional coupler as an example (red part in Table 5.1). The simulated output power at different coupling lengths is shown in Figure 5.5. Simulation data is fitted by sine curves using Eq. (5.2) and (5.3).

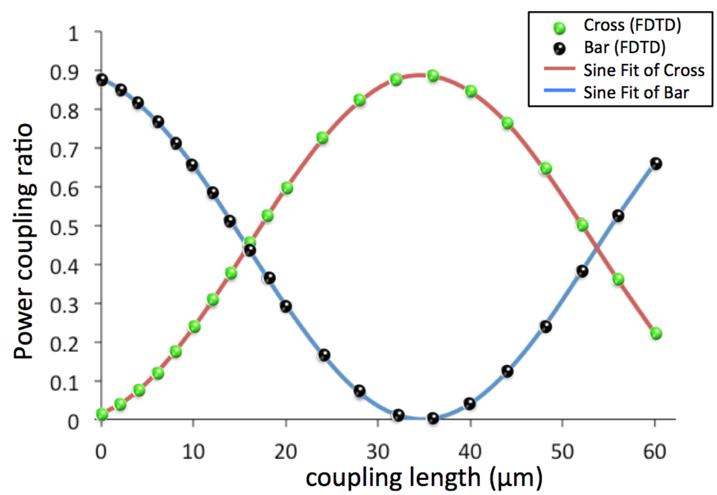

Figure 5.5: FDTD simulation of a directional coupler's (red part in Table 5.1) output power at the different coupling lengths (L).

Table 5.1: Simulation results of different directional couplers.

Type	Gap (nm)	R (μm)	D (μm)	L_c (μm)	ϕ (rad)	L_{50} (μm)	Mesh size in coupling region	Other mesh accuracy
rib	200	20	11.42	13.33	0.36	3.53	λ/40	3
rib	200	10	6.06	15.59	0.33	4.62	λ/50	4
rib	250	20	11.47	20.98	0.31	6.41	λ/40	1
rib	300	20	11.52	23.76	0.21	9.01	λ/40	3
rib	250	20	11.47	21.21	0.30	6.55	λ/40	3
rib	220	20	11.44	17.16	0.35	4.76	λ/40	3
rib	250	20	11.47	20.85	0.29	6.54	λ/100	5
strip	200	20	11.42	38.19	0.13	15.87	λ/40	3
strip	250	20	11.47	62.90	0.087	27.97	λ/40	3
strip	300	20	11.52	86.32	0.057	40.00	λ/40	3
strip	200	15	15.98	37.94	0.12	16.13	λ/40	3
strip	220	20	11.44	43.23	0.11	18.58	λ/50	3

5.3 Experiment and Discussion

5.3.1 Device Fabrication

These devices' fabrication occurred at IME/A*STAR. The starting material was an 8" SOI wafer from SOITEC™, with a Boron-doped top silicon layer of around 10 ohm-cm resistivity and 220 nm thickness, a 2 μm bottom oxide thickness, and a 750 ohm-cm handle silicon wafer, needed for RF performance. A 60 nm anisotropic dry etch was first applied to form the trenches of the GC. Next, the rib waveguides for the directional coupler were formed using additional etch steps. In all cases, 248 nm photolithography was utilized. This is full flow silicon photonic MPW run as we used in Chapter 3.

5.3.2 Coupling Length

We tested the strip directional coupler named device D1 that has a 200nm gap, 20 μm radius, 500 nm width and 220 nm height. A linearly TE polarized light beam from a tunable laser (Agilent™ 81980A) centered at a wavelength around of 1550 nm was coupled into the device through a fiber array and an on-chip GC. The output light was coupled out through another GC to the fiber array and measured by a lightwave multimeter (Agilent™ 8163B). The automatic wafer-scale test setup is discussed in Chapter 4. The coupler's output power at 1550nm at different Ls was measured as shown in Figure 5.6. The device's output routing is carefully designed as shown in Figure 5.6. (a). The adjacent GC's distance is equal to the fiber array's adjacent ports' separation. We placed input GC between two output GCs. Therefore, the output light of bar port and cross port can be measured through the same pair of fiber array's ports. Thus, the influence of different insertion losses due to different fiber array ports is removed from our experiment. The spectra cluster stands for 25 different Ls from 0 to 50 μm in one die as shown in Figure 5.6. (b). We can find the L_{50} by fitting the output power and the coupling length based on Eq. (5.2) and (5.3) as shown in Figure 5.6. (c).

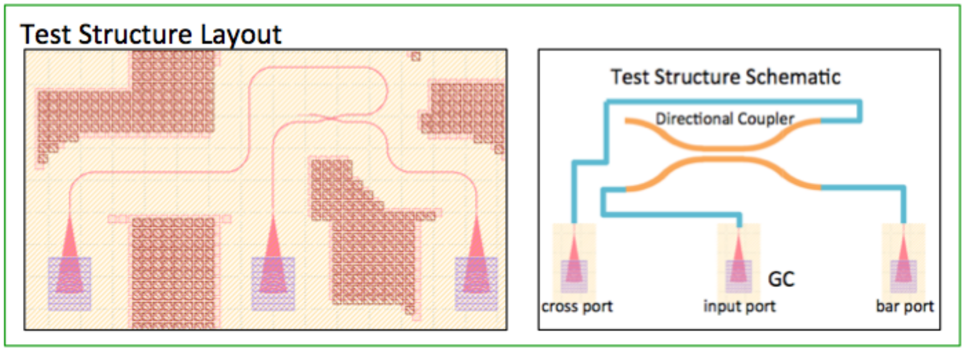

(a)

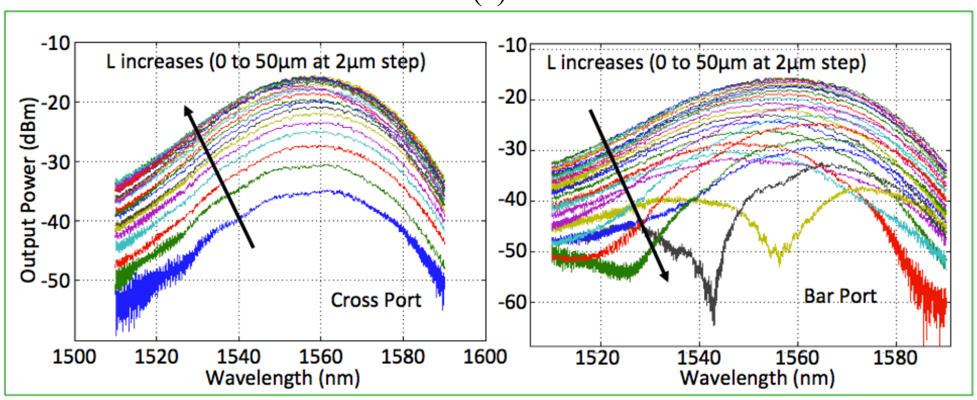

(b)

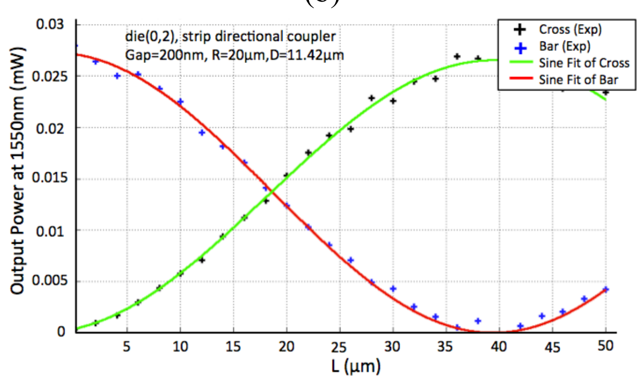

(c)

Figure 5.6: A typical test structure and experimental results of the strip directional coupler in one die. (a) One test structure layout of the strip directional coupler and its equivalent schematic. The difference between test structures is L. (b) The output spectra of directional coupler's cross port and bar port. Input light power is 0 dBm. (c) Directional coupler's output power at different coupling lengths.

By the same method, we measured several different types of directional couplers. For clear illustration, we named different directional couplers as shown in Table.5.2. The L_{50} in far-apart five dies were measured across the wafer. They were consistent. If the standard deviation of L_{50} is δL, we define the figure of merit $R_L=\delta L$ / L_{50} to evaluate the performance consistence across wafer as shown in Figure 5.7 (a). We found that device C1 and D1 had better consistence across the wafer. Device C1 has the best consistent performance and the smallest $L_{50.}$ Therefore, device C1, D1 are good candidates of PDKs.

Table 5.2: Designed geometry of directional couplers and their measured L_{50}.

Design	*50% coupling length (µm)*	*Gap (nm)*	*Waveguide Width (nm)*	*R (µm)*	*D (µm)*	*Waveguide type*
Device C1	3.65+/- 0.04	200	500	20	4	rib
Device D1	18.64 +/- 0.31	200	500	20	4	strip
Device D2	17.73 +/- 0.36	200	500	15	4	strip
Device D3	29.11 +/- 0.90	250	500	20	4	strip
Device D4	41.94 +/- 1.94	300	500	20	4	strip

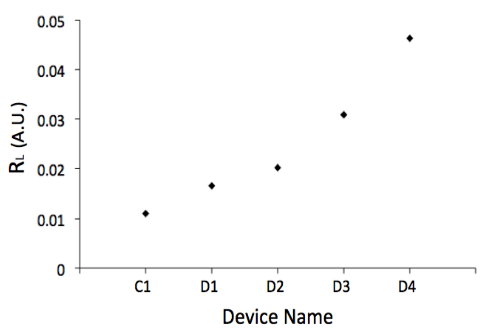

(a)

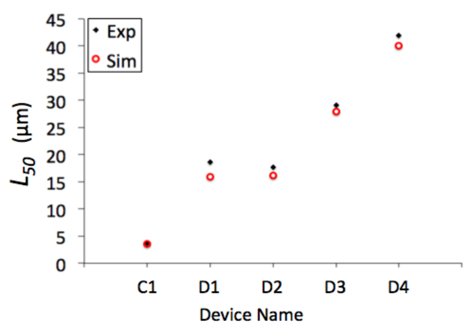

(b)

Figure 5.7: Experimental results of different directional couplers: (a) performance consistence across the wafer. $R_L= \delta L$ / L_{50} ;(b) experimental results of L_{50} and the simulated values by FDTD as shown in Table.5.1. Device name is defined in Table.5.2.

5.3.3 Fabrication Error Model

Comparing the experimental and simulation data, we found that there were mismatches as shown in Figure 5.7(b). For example, the measured average L_{50} of device D1 was 18.64 +/- 0.31μm. Looking at the simulated L_{50} (15.87 μm) as shown in Table 5.1 and Figure 5.5, the difference was 2.7μm. This could due to the numerical error in the FDTD simulation and the device geometry deviation in the real fabrication processes. For example, the sidewall angle of a fabricated rib waveguide was about 76° other than the ideal 90° as shown in Figure 5.8. In order to study the fabrication error pattern, we used SEM to measure device D1, D2 and D3's geometry. Device D1's average waveguide width was 523nm and the average gap was 176nm. The measured gap and width of device D2 were the same as those of device D1. Device D3's average waveguide width was 530nm and the average gap was 232nm. By the experimental results, we can predict the fabrication error model as shown in Figure 5.9. The model shows that when the waveguide width increases Δ, the gap will decrease Δ accordingly in the directional coupler's coupling region. Device D1's experimental results satisfied this model very well and its Δ =23.5nm that is calculated by

$$\Delta = \frac{|W_{SEM} - W_{design}| + |Gap_{SEM} - Gap_{design}|}{2}. \qquad (5.4)$$

The model can also predict device D3's performance qualitatively because we found $|W_{SEM}\text{-}W_{design}|$ and $|Gap_{SEM}\text{-}Gap_{design}|$ were close if we considered the 10nm uncertainty of SEM test. And its Δ was about 24nm. By the same way, we analyzed device D2 and its Δ was about 23.5nm. We plugged the SEM measured waveguide width and gap values into the FDTD simulation. Then we got the corrected L_{50} of device D1, D2 and D3, which were 18.31 μm, 17.44 μm and 29.13μm. Considering corresponding experimental results that were 18.64 μm, 17.73 μm and 29.11 μm as shown in Figure 5.7 (b) and Table.5.2, we verified the proposed fabrication error model by the good agreement between the simulation and the experiment.

To sum up, in order to design directional coupler with desired coupling ratio, we should not rely too heavily on the FDTD simulation but on the experimental data to calibrate the error of simulation.

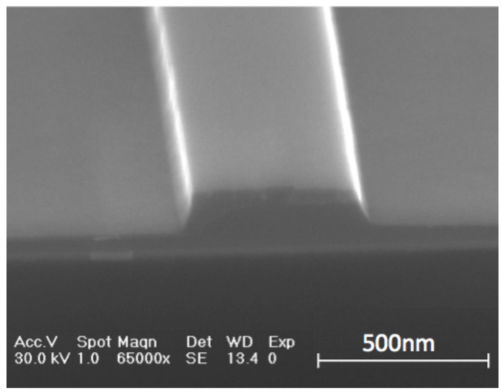

Figure 5.8: SEM micrograph of the cross-section of a fabricated rib waveguide.

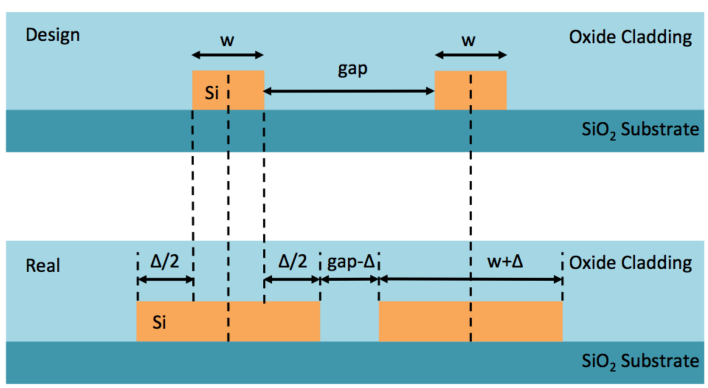

Figure 5.9: Fabrication error model.

5.3.4 Excess Loss

Chaining a large number of directional couplers in series so a linear regression can be performed in order to deduce the loss per device. The passive test setup is the same as the section 4.3. Device D1 and C1 were tested. The single device D1's output power is shown in Figure 5.10. The excess loss is defined as the difference between the input power and the sum of the bar port and the cross port output power. And the insertion loss is defined as the difference between the input power and the bar/cross port (single port) output power. After de-embedding the GC response shown in Figure 5.10, device D1's bar and cross ports' insertion losses were 3.02 and 3.01 dB at 1549nm when L=16 μm. The total output power (cross + bar) from cascaded devices was measured by the characterizing structures that are shown in Figure 5.11 (a). By linear regression, the loss of each device could be extracted by measuring the relationship between total output power and cascaded device number as shown in Figure 5.11 (b,c). The excess loss of device D1 at L=16 μm across the wafer was about 0.009 +/- 0.002 dB/each as shown in Table.5.4. By the same way, the excess loss of device C1 at L=4 μm across the wafer was about 0.046 +/- 0.014 dB/each. Thus, the directional coupler's low excess loss was proved by experiments.

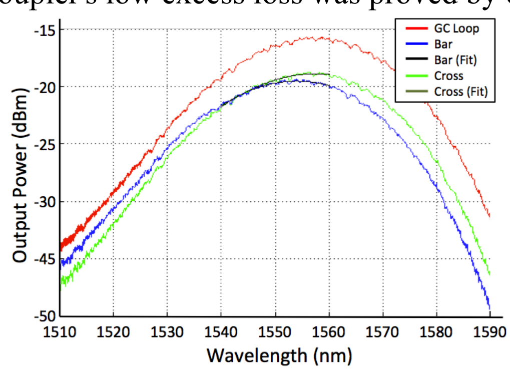

Figure 5.10: The output power spectra of a single directional coupler (device D1 with L=16 μm): blue curve: bar port; green curve: cross port; red curve: nearby control GC loop.

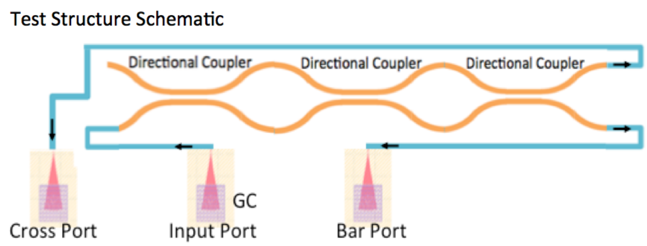

(a)

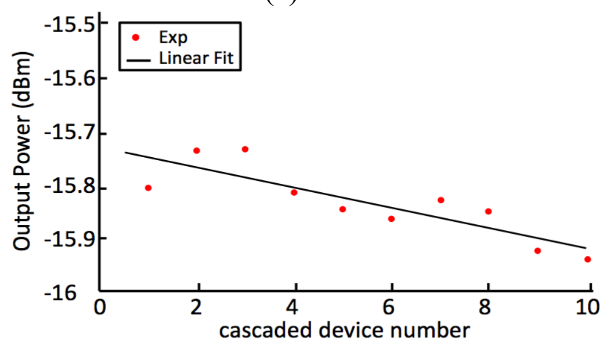

(b)

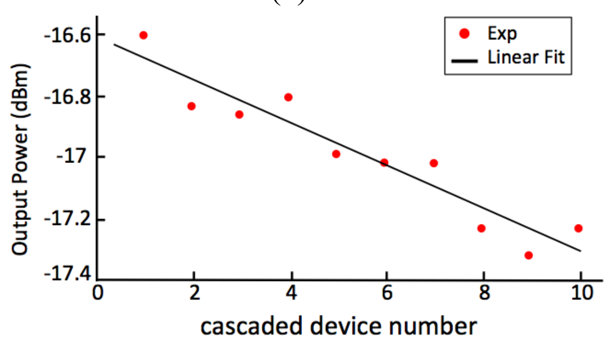

(c)

Figure 5.11: Directional coupler's excess loss. (a) schematic of the cascaded test structure; (b) device D1's test results; (c) device C1's test results.

Table 5.3: Measured excess losses of directional couplers.

Device D1	Loss (dB)
Die (0,0)	0.012
Die (2,0)	0.011
Die (-2,0)	0.009
Die (0,2)	0.007
Die (0,-2)	0.008
Average	0.009 +/- 0.002

Device C1	Loss (dB)
Die (0,0)	0.067
Die (2,0)	0.050
Die (-2,0)	0.025
Die (0,2)	0.040
Die (0,-2)	0.038
Average	0.046 +/- 0.014

5.3.5 Wavelength Dependence

A study on the typical wavelength dependence of device C1 and D1 was performed. To de-convolve the results from the wavelength dependence of the GC structure, the output spectrum from a directional coupler structure was subtracted from that of a control GC structure. In the ideal case, this would expose only the wavelength dependence of the directional coupler. The measurements are challenging, as the wavelength dependence of the GC is not completely consistent and difficult to de-convolve entirely from the directional coupler. If the application is highly dependent on the fine structure of the directional coupler, an FDTD simulation is suggested, with the precise layer thicknesses adjusted until the observed 50% coupling lengths are matched. The spectra of bar port and cross port were measured for device C1 at L = 4 μm and device D1 at L=18 μm. The output power was then de-embedded from the GC loop's spectrum as shown in Figure 5.12. The wavelength dependent effect is not dramatic, but it does exist. For device C1, the dispersion slope of the cross port and the bar port are 0.01dB/nm and -0.007dB/nm, respectively. For device D1, the dispersion slope of the cross port and the bar port are 0.03dB/nm and -0.02dB/nm, respectively.

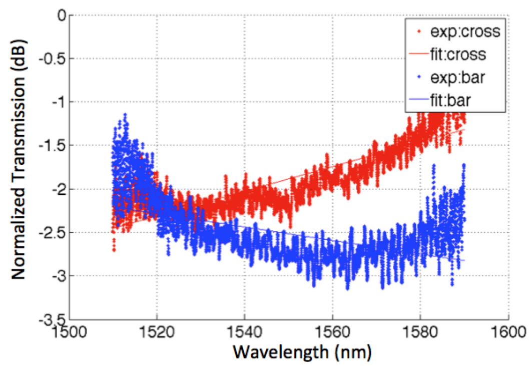

(a)

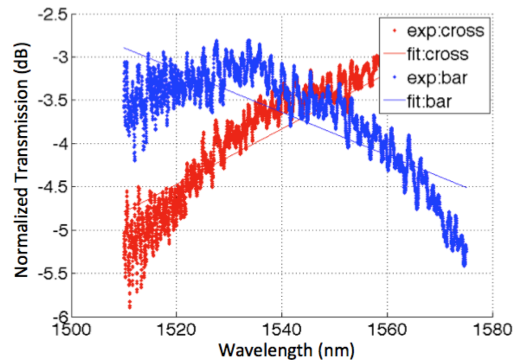

(b)

Figure 5.12: The test results of wavelength dependence after de-embedded from the GC's response. (a) Device C1 at L=4 µm. (b) Device D1 at L=18 µm.

5.4 Summary

High yield low loss silicon directional couplers were designed and fabricated. There was a good agreement between FDTD simulations and experimental results if using our fabrication error model. A strip directional coupler and a rib directional coupler are selected as PDKs for the application of non-reciprocal architectures. Standard deviations of 50% coupling lengths across the wafer are 0.04 µm and 0.31 µm for these devices. Their excess losses are about 0.046 dB and 0.009 dB, respectively.

Chapter 6

CONCLUSIONS AND FUTURE WORK

6.1 Conclusions

An on-chip isolator is the last key optical component missing from the increasingly popular silicon photonic platforms fabricated in CMOS-compatible processes. This dissertation focuses on this kind of device that exhibits nonreciprocal behavior without the use of unconventional materials. The device only relies on time-dependent optical phase modulation to break time-reversal symmetry. The author designs and demonstrates the non-reciprocal system in fiber optics and show that there is a clear path to implement it in silicon photonics or any other PIC platform in which modulators are available. The proposed non-reciprocal system features a significantly improved level of performance compared to other non-magnetic isolators. It is flexible and scalable to meet real application requirements. Moreover, this is the first demonstration of not just modulation-based isolation, but circulation as well, whereby the reverse flowing mode can be captured with minimal additional loss. This work has the potential to remove a major roadblock toward the development of truly large-scale and complex PICs.

In the study of the active device applied in this non-reciprocal system, the author realizes a high linear on-chip single drive push-pull Si TWMZ modulator. Experiment shows that effective 3^{rd} order nonlinearity cancellation is possible by properly adjusting the bias point of the modulator. The author measured an inter-modulation distortion of 100.4 dB·Hz$^{2/3}$ and second harmonic distortion of 90.5

dB·$Hz^{1/2}$ when the modulator was reversely biased at -2V. A predictive model of the performance is given. This work proves that the silicon optical modulator is capable of being applied not only in the data communication but also in analog optical links.

Fabrication non-uniformity makes accurate phase control hard and increases the difficulty of building an integrated isolator or other PICs. In order to quantitate this non-uniformity, the author reports two typical phase coherence lengths in highly confined silicon waveguides fabricated in a standard CMOS foundry's MPW run for the first time. The coherence lengths are 4.17 ± 0.42 mm and 1.61 ± 0.12 mm for single mode strip and rib waveguide, respectively. The author presents a new analyzing and experiment method to extract the phase coherence length. The theory model was verified by experiments. The coherence length is expected to help design large-scale complex PICs including our non-reciprocal system.

Finally, the author designed, fabricated and measured several compact directional couplers that have low loss and high consistent performance in the silicon photonic platform. They are key passive devices in our non-reciprocal system. When the coupling length is near 50% coupling length, strip and rib directional couplers' excess losses are about 0.046 dB and 0.009 dB, respectively.

6.2 Future Work

In this dissertation, the non-reciprocal chip-scale photonic architecture in silicon is established and demonstrated, which is comprised of with optical delay lines, directional couplers and modulators driven by matched signals. In the future, low driving speed on-chip isolator/circulator should be pursued in order to simplify the system design and increase the robustness of performance. On-chip optical delay line is an essential component required by the non-reciprocal system. Additional development in fabrication uniformity is called for large delay time and low insertion loss. It was also shown that the on-chip drive signals' phase and amplitude have a significant impact on the performance of the non-reciprocal system. Further study is necessary to optimize the design of the on-chip modulator driver. Future work is also desired to improve the directional coupler's 3dB bandwidth by introducing the phase control technologies, which will increase the non-reciprocal system's optical bandwidth.

REFERENCES

1 Cisco™ corporation: "Cisco visual networking index: global mobile data traffic forecast update 2014–2019 white paper," Internet source:

http://www.cisco.com/c/en/us/solutions/collateral/service-provider/visual-networking-index-vni/white_paper_c11-520862.html (2015.3.12).

2. E. Mohammed, A. Alduino, T. Thomas, H. Braunisch, D. Lu, J. Heck, A. Liu, I. Young, B. Barnett, G. Vandentop, and R. Mooney, "Optical interconnect system integration for ultra-short reach applications," Intel. Technology Journal, vol. 8, No.2, pp. 115–127 (2004).

3. R. Soref and J. Lorenzo, "All-silicon active and passive guided-wave components for λ = 1.3 and 1.6 μm," IEEE J. Quantum Electronics, vol. QE-22, no.6, pp. 873–879 (1986).

4. R. Soref and B. R. Bennett, "Kramers–Kronig analysis of E–O switching in silicon," in Proc. SPIE Integr. Opt. Circuit Eng., vol. 704, pp. 32–37 (1986).

5. B. Schuppert, J. Schmidtchen, and K. Petermann, "Optical channel waveguides in silicon diffused from Ge-Si alloy," Electron. Lett., vol. 25, no. 22, pp. 1500–1502, Oct. (1989).

6. R. Soref, J. Schmidtchen, and K. Petermann, "Large single-mode rib waveguides in Ge-Si and Si-on-SiO2," IEEE J. Quantum Electron., vol. 27, no. 8, pp. 1971–1974, Aug (1991).

7. B. Jalali and S. Fathpour, "Silicon photonics," J. Lightwave Technology, vol. 24, no.12, pp. 4600-4615 (2006).

8. Y. Liu, R. Ding, Y. Ma, Y. Yang, Z. Xuan, Q. Li, A. Lim, G. Lo, K. Bergman, T. Baehr-Jones and M. Hochberg, "Silicon Mod-MUX-Ring transmitter with 4 channels at 40 Gb/s" Opt. Express, vol. 22, no.13, pp.16431-16438 (2014).

9. M. Streshinsky, A. Ayazi, Z. Xuan, A. E. Lim, G. Lo, T. Baehr-Jones, and M. Hochberg, "Highly linear silicon traveling wave Mach-Zehnder carrier depletion modulator based on differential drive," Opt. Express, vol. 21, no.3, pp.3818–3825 (2013).

10. A. Ayazi, T. Baehr-Jones, Y. Liu, A. E.J. Lim, and M. Hochberg, “Linearity of silicon ring modulators for analog optical links,” Opt. Express, vol. 20, no.12, pp.13115–13122 (2012).

11. R. Cardenas, P. Morton, J. Khurgin, A. Griffith, C. Poitras, K. Preston and M. Lipson, “Linearized silicon modulator based on a ring assisted Mach Zehnder interferometer,” Opt. Express, vol. 21, no.19, pp.22549-22557 (2013).

12. S. Hu, Y. Zhao, K. Qin, S. T. Retterer, I. I. Kravchenko, and S. M. Weiss, "Enhancing the sensitivity of label-free silicon photonic biosensors through increased probe molecule density," ACS Photonics, vol.1, no.7, pp. 590–597 (2014).

13. B. Jalali, "Silicon photonics: nonlinear optics in the mid-infrared," Nature Photonics 4, pp.506 - 508 (2010).

14. C. Harris, D. Grassani, A. Simbula, M. Pant, M. Galli, T. Baehr-Jones, M. Hochberg, D. Englund, D. Bajoni, and C. Galland, "Integrated source of spectrally filtered correlated photons for large-scale quantum photonic systems", Phys. Rev. X 4, pp. 041047 (1–10) (2014).

15. Dong, X. Liu, S. Chandrasekhar, L. Buhl, R. Aroca, and Y. Chen, "Monolithic silicon photonic integrated circuits for compact 100+Gb/s coherent optical receivers and transmitters," IEEE J. Sel. Top. Quantum Electron., vol. 20, no.4, pp.6100108 (2014).

16. N. Sherwood-Droz and M. Lipson, "Scalable 3D dense integration of photonics on bulk silicon," Opt. Express, vol.19, no.18, pp.17758-17764 (2011).

17. T. Baehr-Jones, T. Pinguet, G. Lo, S. Danziger, D. Prather, and M. Hochberg. "Myths and rumors of silicon photonics." Nature Photonics, vol.6, no.4, pp. 206-208 (2012).

18. M. Streshinsky, R. Ding, Y. Liu, A. Novack, C. Galland, A. Lim, P. Guo-Qiang Lo, T. Baehr-Jones, and M. Hochberg, "the Road to affordable, large-scale silicon photonics," Opt. Photon. News, vol.24, no.9, pp.32-39 (2013).

19. EPIXfab^{TM}, Internet Source: http://www.epixfab.eu/ (12.20.2014).

20. D. Liang, G. Roelkens, R. Baets, and J. E. Bowers, "Hybrid integrated platforms for silicon photonics," Materials, vol.3, no.3, pp. 1782-1802 (2010).

21. K.Tanabe, K. Watanabe, and Y. Arakawa, "III-V/Si hybrid photonic devices by direct fusion bonding," Scientific Reports. vol.2, no.349, pp.1-6 (2012).

22. K. Hill and G. Meltz, "Fiber Bragg grating technology fundamentals and overview." J. Lightwave Technol., vol.15, no.8, pp.1263-1276 (1997).

23. Y. Shoji, T. Mizumoto, H. Yokoi, I. W. Hsieh and R. M. Osgood, "Magneto-optical isolator with silicon waveguides fabricated by direct bonding," Appl. Phys. Lett., vol.92, pp. 071117(1-3) (2008).

24. T. Shintaku, "Integrated Optical Isolator Based on Efficient Nonreciprocal Radiation Mode Conversion," App. Phys. Lett., vol. 73, pp.1946-1948 (1998).

25. J. Hwang, M. H. Song, B. Park, S. Nishimura, T. Toyooka, J. W. Wu, Yoichi Takanishi, Ken Ishikawa and Hideo Takezoe, "Electro-tunable optical diode based on photonic bandgap liquid-crystal heterojunctions," M. Nature, vol.4, pp.383-387 (2005).

26. H. Shimizu and Y. Nakano, "Fabrication and Characterization of an InGaAsP /InP active waveguide optical isolator with 14.7 dB/mm TE mode nonreciprocal attenuation," J. Lightwave Tech. vol.24, no.1, pp.38-43 (2006).

27. W.V. Parys, B. Moeyersoon, D. V. Thourhout, R. Baets, M. Vanwolleghem, B. Dagens, J. Decobert, O. L. Gouezigou, D. Make, R. Vanheertum and L. Lagae, "Transverse magnetic mode nonreciprocal propagation in an amplifying AlGaInAs / InP optical waveguide isolator," Appl. Phys. Lett., vol. 88, pp.071115(1-3) (2006).

28. L. Bi, J. Hu, P. Jiang, D. H. Kim, G. F. Dionne, L. C. Kimerling and C. A. Ross, "On-chip optical isolation in monolithically integrated non-reciprocal optical resonators," Nature Photon. vol.5, pp.758-762 (2011).

29. M. C. Tien, T. Mizumoto, P. Pintus, H. Kromer and J. E. Bowers, "Silicon ring isolators with bonded nonreciprocal magneto-optic garnets," Opt. Express, vol. 19, no.12, pp.11740-11745 (2011).

30. K. Gallo, G. Assanto, K. R. Parameswaran, M. M. Fejer, "All-optical diode in a periodically poled lithium niobate waveguide," Appl. Phys. Lett., vol.9, no.3, pp. 314-316 (2001).

31. M. Fujii, A. Maitra, C. Poulton, J. Leuthold, and W. Freude, "Non-reciprocal transmission and Schmitt trigger operation in strongly modulated asymmetric WBGs," Opt. Express, vol.14, no.26, pp. 12782-12793 (2006).

32. S. Manipatruni, J. T. Robinson and M. Lipson, "Optical nonreciprocity in optomechanical structures," Phys. Rev. Lett., vol. 102, pp. 213903(1-4) (2009).

33. H. Lira, Z. Yu, S. Fan and M. Lipson, "Electrically driven nonreciprocity induced by interband photonic transition on a silicon chip," Phys. Rev. Lett., vol.109, pp. 033901(1-5) (2012).

34. S. Bhandare, S. K. Ibrahim, D. Sandel, H. Zhang, F. Wust, and R. Noé, "Novel nonmagnetic 30-dB traveling-wave single-sideband optical isolator integrated in III/V material," IEEE J. Sel. Top. Quantum Electron.,vol.11, no.2, pp. 417-421 (2005).

35. C. Doerr, L. Chen and D. Vermeulen, "Silicon photonics broadband modulation-based isolator," Opt. Express, vol.22, no.4, pp.4493-4498 (2014).

36. C. Galland, R. Ding, N. C. Harris, T. Baehr-Jones and M. Hochberg, "Broadband on-chip optical non-reciprocity using phase modulators," Opt. Express, vol.21, no.13, pp. 14500-14511 (2013).

37. E. Li, B. J. Eggleton, K. Fang and S. Fan, "Photonic Aharonov–Bohm effect in photon–phonon interactions," Nature Communications, vol.4225, pp.1-5 (2014).

38. Q. Xu, B. Schmidt, S. Pradhan and M. Lipson, "Micrometer-scale silicon electro-optic modulator," Nature, vol.435, pp.325-327 (2005).

39. G. Li, X. Zheng, H. Thacker, J. Yao, Y. Luo, I. Shubin, K. Raj, J. Cunningham, A. Krishnamoorthy, "40 Gb/s thermally tunable CMOS ring modulator," in Proceedings of IEEE 9th International Group IV Photonics, pp. 1–3 (2012).

40. D. Petousi, L. Zimmermann, A. Gajda, M. Kroh, K. Voigt, G. Winzer, B. Tillack K. Petermann, "Analysis of optical and electrical tradeoffs of traveling-wave depletion-type Si Mach–Zehnder modulators for high-speed operation," IEEE J. Sel. Top. Quantum Electron, vol.21, no.4, pp.1-8, (2014)

41. A. Krishnamoorthy, X. Zheng, G. Li, J. Yao, T. Pinguet, A. Mekis, H. Thacker, I. Shubin, Y. Luo, K. Raj, and J. Cunningham1,"Exploiting CMOS Manufacturing to Reduce Tuning Requirements for Resonant Optical Devices," Photonics Journal, IEEE, vol.3, no.3, pp. 567-579 (2011).

42. R. Adar, C. Henry, M. Milbrodt, and R. Kistler, "phase coherence of optical waveguides", J. Lightwave Technol. IEEE, vo.12, no.4, pp. 603-606 (1994).

43. R. Feced and M. Zervas, "Effects of random phase and amplitude errors in optical fiber Bragg gratings," J. Lightwave Technol. IEEE, vol.18, no.1 pp.90-101 (2000).

44. S. Fan, R. Baets, A. Petrov, Z. Yu, J. D. Joannopoulos, W. Freude, A. Melloni, M. Popovic, M. Vanwolleghem, D. Jalas, M. Eich, M. Krause, H. Renner, E. Brinkmeyer and C. R. Doerr, "Comment on 'Nonreciprocal Light Propagation in a Silicon Photonic Circuit'," Science, vol.335, no.6064, pp.38 (1-2) (2012).

45. D. Jalas, A. Petrov, M. Eich, W. Freude, S. Fan, Z. Yu, R. Baets, M. Popovic, A. Melloni, J. D. Joannopoulos, M. Vanwolleghem, C. R. Doerr and H. Renner, "What is - and what is not - an optical isolator," Nature Photon., vol.7, pp. 579-582 (2013).

46. Haus, H. A. Waves and Fields in Optoelectronics (Prentice- Hall, 1984) Ch. 3.

47. H. Shimizu and Y. Nakano, "Fabrication and Characterization of an InGaAsp/InP Active Waveguide Optical Isolator with 14.7 dB/mm TE Mode Nonreciprocal Attenuation," J. Lightw. Technol. IEEE., vol.24, no.1, pp.38-43 (2006).

48. S. Ghosh, S. Keyvavinia, W. Van Roy, T. Mizumoto, G. Roelkens and R. Baets, "Ce: YIG/Silicon-on-Insulator waveguide optical isolator realized by adhesive bonding," Opt. Express, vol.20, no.2, pp.1839-1848 (2012).

49. Y. Shoji and T. Mizumoto, "Magneto-optical non-reciprocal devices in silicon photonics," Science and Technology of Advanced Materials, vol.15, pp .014602 (2014).

50. F. Li, J. Wang, L. T. Varghese, H. Shen, B. Niu, Y. Xuan, A. M. Weiner and M. Qi, "An All-Silicon Passive Optical Diode," Science, vol.335, pp.447-450 (2012).

51. L. Wang, L. T. Varghese, J. Wang, Y. Xuan, A. M. Weiner and M. Qi, "Silicon optical diode with 40dB nonreciprocal transmission," Optics Lett., vol.38, no.8, pp.1259-1261 (2013).

52. General Photonics ™: inline isolator, Internet source:

http://pdf.directindustry.com/pdf/general-photonics/line-isolator-notail/36256-171412.html

53. Y. Liu, S. Dunham, T. Baehr-Jones, A.E. Lim, G. Lo and M. Hochberg, "Ultra-responsive phase shifters for depletion mode silicon modulators," J. Lightwave Technol., vol.31, no.23, pp.3787-3793 (2013).

54. C. Galland, A. Novack, Y. Liu, R. Ding, M. Gould, T. Baehr-Jones, Q. Li, Y. Yang, Y. Ma, Y. Zhang, K. Padmaraju, K. Bergman, A. E. Lim, G. Lo and M. Hochberg, " A CMOS-compatible silicon photonic platform for high-speed integrated opto-electronics," Proc. SPIE, INTEGRATED PHOTONICS: MATERIALS, DEVICES, AND APPLICATIONS II. 8767, G1-G8 (2013).

55. R. A. Soref and B. R. Bennett, "Electrooptical effects in silicon," Quantum Electronics, IEEE Journal of, vol. 23, no.1, pp.123–129 (1987).

56. T. Baehr-Jones, M. Hochberg, C. Walker, E. Chan, D. Koshinz, W. Krug, and A. Scherer, "Analysis of the tuning sensitivity of silicon-on-insulator optical ring resonators," J. Lightwave. Technol. IEEE., vol.23, no.12, pp. 4215–4221, (2005).

57. S. L. Chuang, Physics of Optoelectronics Devices. (John Wiley, New York, 1995).

58. TCAD Lab, PN Junction simulation tool, Internet source: https://nanohub.org/tools/atcadlab/session?sess=830227 (3.1.2015)

59. Multi-Physics Software ™ Comsol ™ Corporation, "RF Module - Software for Microwave and RF Design," Internet source:

http://www.comsol.com/rf-module (3.1.2015).

60. Ion Implantation simulation tool, Internet Source:

http://www.cleanroom.byu.edu/implantcal.phtml (3.2015)

61. T. Li, D. Wang, J. Zhang, Z. Zhou, F. Zhang, X. Wang and H. Wu. "Demonstration of 6.25 G baud advanced modulation formats with subcarrier multiplexed technique on silicon Mach-Zehnder modulator." Opt. Express, vol.22, no.16, pp.19818-19823 (2014).

62. P. Dong, L. Chen, and Y. Chen, "High-speed low-voltage single-drive push-pull silicon Mach-Zehnder modulators," Opt. Express, vo.20, no.6, pp.6163-6169 (2012).

63. L. Liao, A. Liu, D. Rubin, J. Basak, Y. Chetrit, H. Nguyen, R. Cohen, N. Izhaky and M. Paniccia, “40 Gbit/s silicon optical modulator for high speed applications,” Electron. Lett., vol.43, no.22, pp.1196–1197 (2007).

64. F. Junichi, U. Jun, M. Yu, L. Ding, G. Lo, K. Dim-Lee and T. Nakamura, “25 GHz operation of silicon optical modulator with projection MOS structure,” in Optical Fiber Communication Conference, 2010 OSA Technical Digest Series (Optical Society of America, 2010), paper OMI3.

65. F. Y. Gardes, D. J. Thomson, N. G. Emerson, and G. T. Reed, “40 Gb/s silicon photonics modulator for TE and TM polarizations,” Opt. Express, vol.19, no.12, pp.11804–11814 (2011).

66. D. Thomson, F. Gardes, J. Fedeli, S. Zlatanovic, Y. Hu, B. Kuo, E. Myslivets, and N. Alic, S. Radic, G. Z. Mashanovich and G. T. Reed, “50Gbit/s silicon optical modulator,” Photon. Technol. Lett., IEEE vol.24, no.4, 234–236 (2012).

67. L. Chen, C. Doerr, P. Dong, and Y. K. Chen, “Monolithic silicon chip with 10 modulator channels at 25 Gb/s and 100-GHz spacing,” Opt. Express vol.19, no.26, pp. 946-951 (2011).

68. R. Ding, Y. Liu, Q. Li, Y. Yang, Y. Ma, K. Padmaraju, A. Lim T. Baehr-Jones and M. Hochberg, "Design and characterization of a 30-GHz bandwidth low-power silicon traveling-wave modulator," Optics Communications vol.321, 124-133(2014).

69. L. Chen, P. Dong, and Y. Chen, "Chirp and dispersion tolerance of a single-drive push–pull silicon modulator at 28 Gb/s," Photon. Technol. Lett., IEEE vol.24, no.11, pp.936-938 (2012).

70. A. Khilo, C. Sorace, and F. Kärtner, "Broadband linearized silicon modulator," Opt. Express 19(5) 4485-4500 (2011).

71. X. Luo, X. Tu, J. Song, L. Ding, Q. Fang, T. Liow, M. Yu, and G. Luo, "Slope efficiency and spurious-free dynamic range of silicon Mach-Zehnder modulator upon carrier depletion and injection effects," Opt. Express vol.21, no.14, pp. 16570-16577 (2013).

72. Athena™ simulator, SILVACO™ Corporation (2014).

73. Ansoft ™ HFSS software tools (2014).

74. T. Baehr-Jones, R. Ding, Y. Liu, A. Ayazi, T. Pinguet, N. Harris, M. Streshinsky and M. Hochberg, "Ultralow drive voltage silicon traveling-wave modulator," Opt. Express, vol.20, no.11, pp.12014-12020 (2012).

75. Y. Zhang, S. Yang, A. Lim, G. Lo, C. Galland, T. Baehr-Jones and M. Hochberg, "A compact and low loss Y-junction for submicron silicon waveguide," Opt. Express 21(1), 1310-1316 (2013)

76. Thorlabs^{TM} Inc. 40 GHz Phase and Intensity Modulators Spec. Internet source: https://www.thorlabs.com/NewGroupPage9_PF.cfm?Guide=10&Category_ID=220&ObjectGroup_ID=3948 (4.1.2015)

77. J. Schaffner, J. Lam, C. Gaeta, G. Tangonan, R. Joyce, M. Farwell and W. Chang, "Spur-Free dynamic range measurements of a fiber optic link with traveling wave linearized directional coupler modulators", Photon. Technol. Lett., IEEE, vol.6, no.2, pp.273-275 (1994).

78. S. Yang, Y. Zhang, D. W. Grund, G. A. Ejzak, Y. Liu, A. Novack, D. Prather, A. E. Lim, G. Lo, T. Baehr-Jones and M. Hochberg, "A single adiabatic microring-based laser in 220nm silicon-on-insulator," Opt. Express, vol.22, no.1, 1172-1180 (2014).

79. Y. Zhang, S. Yang, Y. Yang, M. Gould, N. Ophir, A. E. Lim, G. Lo, P. Magill, K. Bergman, T. Baehr-Jones, and M. Hochberg, "A high-responsivity photodetector absent metal-germanium direct contact," Opt. Express, vol.22, no.9, pp.11367-11375 (2014).

80. L. Chrostowski and M. Hochberg: Silicon Photonics Design: From Devices to Systems (Cambridge University, 2015)

81. Ding, Ran, "High-Speed Optical Modulators and Data Communication Systems in Silicon Photonics," Doctoral Diss. 2014.

82. W. Zortman, D. Trotter, and M. Watts, "Silicon photonics manufacturing," Opt. Express vol.18, no.23, pp. 23598-23607 (2010).

83. A. Krishnamoorthy, R. Ho, X. Zheng, H. Schwetman, J. Lexau, P. Koka, G. Li, I. Shubin, and J. Cunningham, "Computer systems based on silicon photonic interconnects," Proceedings of the IEEE 97, 1237-1361, (2009).

84. L. Chrostowski, X. Wang, J. Flueckiger, Y. Wu, Y. Wang, and S. Talebi Fard, "Impact of Fabrication Non-Uniformity on Chip-Scale Silicon Photonic Integrated Circuits," in Optical Fiber Communication Conference, OSA Technical Digest (online) (Optical Society of America, 2014), paper Th2A.37.

85. S. Nakamura, S. Yanagimachi, H. Takeshita, A. Tajima, T. Katoh, T. Hino, and K. Fukuchi, "Compact and low-loss 8x8 silicon photonic switch module for transponder aggregators in CDC-ROADM application," in Optical Fiber Communication Conference, OSA Technical Digest (online) (Optical Society of America, 2015), paper M2B.6.

86. C. Gunn, "CMOS photonics for high-speed interconnectors," Micro, IEEE, vol.26, no.2, pp.58–66 (2006).

87. T. Goh, S. Suzuki, and A. Sugita, "Estimation of waveguide phase error in silica-based waveguides," J. Lightwave Technol. IEEE, vol.15, no.11, pp. 2107-2113 (1997).

88. A. Simard, G. Beaudin, V. Aimez, Y. Painchaud, and S. LaRochelle, "Characterization and reduction of spectral distortions in Silicon-on-Insulator integrated Bragg gratings," Opt. Express, vol.21, no.20, pp.23145-23159 (2013).

89. M. Beals, J. Michel, J. Liu, D. Ahn, D. Sparacin, R. Sun, C. Hong, L. Kimerling, A. Pomerene, D. Carothers, J. Beattie, A. Kopa, A. Apsel, M. Rasras, D. Gill, S. Patel, K. Tu, Y. Chen, A. White, "Process flow innovations for photonic device integration in CMOS": Proc. SPIE 6898, pp.1-14 (2008).

90. SOITEC™ Corporation, "Soitec Silicon-On-Isolator products," Internet source:

    http://www.soitec.com/en/products-and-services/microelectronics/wave-soi (3.1.2015)A

91. K. Okamoto, Fundamentals of Optical Waveguides (Academic, 2000).

92. C. Qiu, Z. Sheng, H. Li, W. Liu, L. Li, A. Pang, A. Wu, X. Wang, S. Zou, F. Gan, "Fabrication, characterization and loss analysis of silicon nanowaveguides," J. Lightwave Technol., IEEE, vol.32, no.13, pp.2303-2307 (2014).

93. H. Abediasl and H. Hashemi, "Monolithic optical phased-array transceiver in a standard SOI CMOS process," Opt. Express, vol.23, no.5. pp. 6509-6519 (2015).

94. J. Mower, N. Harris, G. Steinbrecher, Y. Lahini, D. Englund, "Towards high-fidelity quantum computation and simulation on a programmable photonic integrated circuit," Internet Source: http://arxiv.org/abs/1406.3255 (2014).

95. Lumerical™ FDTD, simulation software.

96. H. Yi, Qi. Long, W. Tan, L. Li, X. Wang and Z. Zhou, "Demonstration of low power penalty of silicon Mach–Zehnder modulator in long-haul transmission," Opt. Express, vol.20 no.25, pp.27562-27568 (2012).

97. Karim and J. Devenport, "Noise figure reduction in externally modulated analog fiber-optic links," Photon. Technol. Lett., IEEE vol.19, no.5, pp.312-314 (2007).

Appendix A

SUPPLEMENTAL INFORMATION

A.1 Comparison of On-Chip TWMZ Modulators

Recently reported on-chip silicon TWMZ modulators linearity performances are highlighted in Table A.1. It is based on Figure 3.6 but includes additional details.

Table A.1: Comparison of the state-of-the-art of on-chip silicon TWMZ and ring optical modulator linearity performance (loss, modulation efficiency and bandwidth are also summarized)

Ref	Length (mm)	$V\pi L\pi$ (V·cm)	Insertion Loss (dB)	EO Bandwidth (GHz)	Modulator Type	Linearity Performance
[61]	2	NA	4.5	18	Silicon, TWMZ	SHD-SFDR=79.72 dB·Hz $^{1/2}$ IMD3-SFDR=91.85 dB·Hz $^{2/3}$
[69]	3.4	2.38	6	NA	Silicon, single drive push-pull TWMZ	Negative Chirp coefficient
[96]	2	1.52	20	7.5	Silicon, single drive push-pull TWMZ	Negative Chirp coefficient
[9]	3	3.3	6.7	15.5	Silicon TWMZ	IMD 3-SFDR=97dB·Hz $^{2/3}$ SHD-SFDR=82 dB·Hz $^{1/2}$
[11]	5	NA	10	NA	Silicon TWMZ Assisted with ring resonator	IMD3-SFDR=106 dB·Hz $^{2/3}$
[71]	4	2	10	NA	Silicon TWMZ	IMD3-SFDR=90 dB·Hz $^{2/3}$
[10]	Radius: 30μm	10.6 pm/V	NA	18.8	Silicon Ring Modulator Q=5000, FSR=3.2nm	IMD3-SFDR=84 dB·Hz $^{2/3}$ SHD-SFDR=64.5 dB·Hz $^{1/2}$
[76]	115	63.25	4	35	$LiNbO_3$ TWMZ (Discrete device)	IMD3-SFDR=105.8dB·Hz $^{2/3}$ SHD-SFDR=95.1dB·Hz $^{1/2}$
[97]	NA	NA	4.3	NA	$LiNbO_3$ TWMZ (Discrete device)	IMD3-SFDR= 120.8dB·Hz $^{2/3}$
This work	7	2.2	7.7	15.9	Silicon single drive push-pull TWMZ	IMD3-SFDR=100.4dB·Hz $^{2/3}$ SHD-SFDR=90.6 dB·Hz $^{1/2}$

A.2 Fundamental Optical Mode

The fundamental optical mode profile in the waveguide is simulated with a -2 V bias applied, shown in Figure 11.

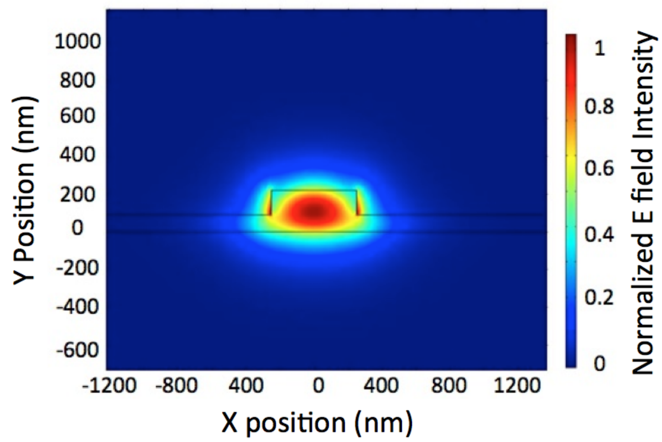

Figure A.1: Fundamental mode profile in the rib waveguide at -2V reverse bias.

A.3 Coherence Length Test Supplemental Information

In our experiment, the total arm lengths (L) of MZIs are: 68.8 μm, 306.2 μm,606.2 μm, 906.2 μm and 1206.2 μm corresponding the arm difference lengths (dL) of 50 μm, 144 μm, 444 μm, 744 μm and 1044 μm. Although the condition $dL >> L_1$ is not always satisfied as shown in Table A1. The condition $L_{coh} >> L_1$ always stands for both waveguides. We think that when $L_{coh} >> L_1$, the dL can replace total length's influence on the L_{coh}. Therefore, replacing Eq. (3-b') by of (3-b') is a good approximation. The relationship $dL >> L_1$ is satisfied as shown in Table A2. Therefore, Eq. (4.3-b) is a good approximation of (4.3-b').

Table A2: MZIs' arm lengths in coherence length experiment. L_1: arm1 length, L_2: arm2 length, $dL=L_2-L_1$; total length=L_1+L_2.

L (μm)	dL (μm)	$L1$ (μm)	$L2$ (μm)	$dL >> L1$?	$L_{coh} >> L_1$
68.8	50	9.42	59.42	No	Yes
306.2	144	81.12	225.12	No	Yes
606.2	444	81.12	525.12	No	Yes
906.2	744	81.12	825.12	Yes	Yes
1206.2	1044	81.12	1125.12	Yes	Yes

The author also studied the relationship between the random phase shift's variance and the MZI's total arm length ($L=L_1+L_2$). The extracted coherence lengths for strip and strip loaded strip waveguides are 4.63 ± 0.35 mm and 1.72 ± 0.11 mm, respectively. The coherence lengths are almost the same as the results extracted from the dL because $dL>> L_1$. But there is one problem: the random phase shift's variance ($<(\Delta\phi)^2>$) is not zero when L = 0 by the linear regression as shown in Figure 4.8. These results go against with the physics In contrast, $<(\Delta\phi)^2>$ extract from dL is almost 0 as shown in Figure 4.5. So using dL is suitable for our experiment condition.

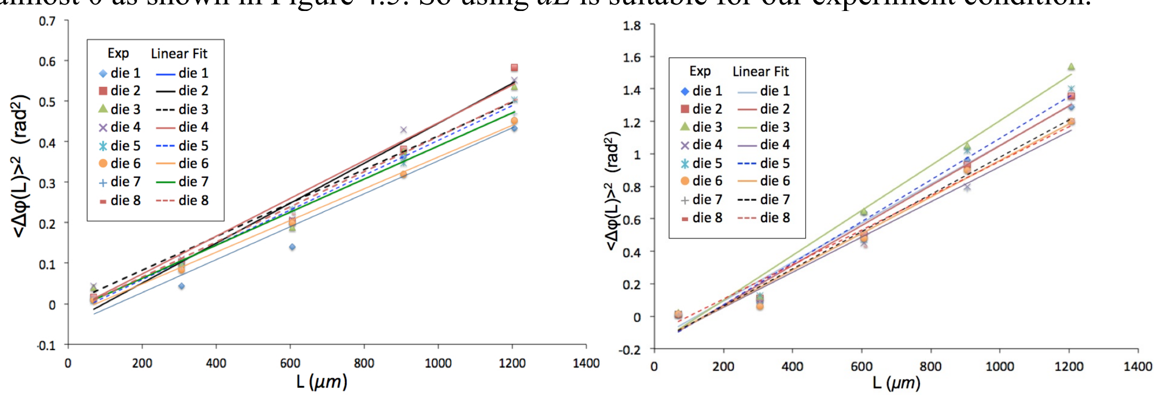

(a) (b)

Figure A.2: The second method of calculating coherence length by the total arm length of MZI: (a, b) the relationship between strip and rib waveguide length and the variances of random phase shifts in 8 dies across a MPW wafer.

To prove the method's feasibility, we also designed and measured about 800 MZIs that have the same dL (110 μm) but different total length (L=1400 μm and 290 μm, respectively). By the same method, the $<\Delta\phi)^2>$ are 0.035 rad^2 when L =1400 μm and 0.033 rad^2 when L =290 μm, which is very close. The small difference in the results proves our analyzing that using dL instead of L to extract coherence length is reasonable.

A.4 Commercial Modulator Specification

The modulator used in our non-reciprocal system is shown in Figure A.3. The modulator1 (M1) and modulator 2 (M2) 's specification is shown in Table A.3 and A.4, respectively.

Figure A.3: The photo of real modulator used in our non-reciprocal system. The port number is consistent with Table A.3 and A.4.

Table A3: Modulator 1 (M1)'s specifications at 1550nm input wavelength.

Input port 1		
Insertion loss	output port 1	output port 2
switched to output port 1	-3.7 dB	<-29 dB
switched to output port 2	<-25 dB	-3.7 dB
Input port2		
Insertion loss	output port 1	output port 2
switched to output port 1	-3.8 dB	<-23 dB
switched to output port 2	<-26 dB	-3.7 dB

RF port : Vpi	4.6V @ 1GHz
DC port : Vpi	5.2V @ DC
EO 3dB Bandwidth	15 GHz

Table A4: Modulator 2 (M2)'s specifications at 1550nm input wavelength.

Input port 1		
	output port 1	output port 2
switched to output port 1	-3.6dB	<-29dB
switched to output port 2	<-24dB	-3.8dB
Input port2		
	output port 1	output port 2
switched to output port 1	-3.5 dB	<-23 dB
switched to output port 2	<-29 dB	-36 dB

RF port : Vpi	4.6V @ 1GHz
DC port : Vpi	5.2V @ DC
EO 3dB Bandwidth	13 GHz

A.5 Analyzing the IMD3's Slope

Our silicon TWMZ modulator schematic is shown as below.

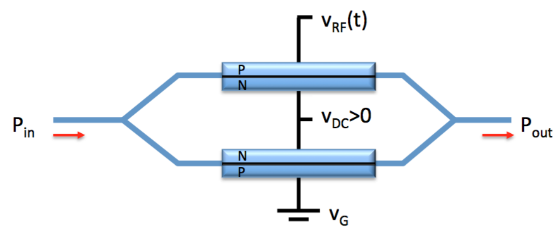

Figure A.4 Schematic of single drive push-pull Si TWMZ modulator.

The optic power at output of the modulator is:

$$P_{out} = \frac{1}{4} P_{in}(2e^{\alpha_A+\alpha_B} cos(\phi_B - \phi_A) + e^{2\alpha_A} + e^{2\alpha_B}) \qquad (A.1)$$

α_A and α_B are the field amplitude losses in the top and bottom phase shifters. ϕ_A and ϕ_B are the phase shifts in the top and bottom phase shifters. In push-pull configuration, $\phi_A = \phi(V_{DC} - \frac{1}{2}V_{RF}), \phi_B = \phi(V_{DC} + \frac{1}{2}V_{RF})$. To analyze the linearity of the MZ transfer function, let us expand the phase ϕ and loss α into a Taylor series around the DC voltage:

$$\phi(V_{DC}+v) = (\phi_{DC} + \phi_1 v + \phi_2 v^2 + \phi_3 v^3 + \ldots)L \tag{A.2}$$

$$\alpha(V_{DC}+v) = (\alpha_{DC} + \alpha_1 v + \alpha_2 v^2 + \alpha_3 v^3 + \ldots)L \tag{A.3}$$

$$cos\,(\phi_B - \phi_A) = sin(\tfrac{\pi}{2} - (\phi_B - \phi_A)) \approx \tfrac{\pi}{2} - (\phi_B - \phi_A) = \tfrac{\pi}{2} - 2(\phi_1 v + \phi_3 v^3 + \ldots)\mathrm{L} \tag{A.4}$$

$$where\ v = \frac{1}{2}V_{RF}$$

We use quadrature bias to get large modulation depth ($\phi_B - \phi_A \approx \frac{\pi}{2}$). So Eq. (A.4) is used in the approximation. Plugging Eq. (A.2)-(A.4) to (A.1) and performing a Taylor expansion, the expressions that describe modulator linearity are finally obtained:

$$P_{out} \approx \frac{1}{2}e^{2\alpha_{DC}\cdot L}\cdot P_{in}\Big[(1+\frac{\pi}{2}) - (2\phi_1)\mathrm{v} + (1+\frac{\pi}{2})(2\alpha_2\cdot \mathrm{L})\mathrm{v}^2 + (-2\phi_3\mathrm{L} - 4\alpha_2\phi_1\mathrm{L}^2)\mathrm{v}^3 + (-4\alpha_2\phi_3\mathrm{L}^2)\mathrm{v}^5\Big] \tag{A.5}$$

The IMD3 item $(2\omega_2 - \omega_1)$ is also included in v^5.

Appendix B

LIST OF PUBLICATIONS

Journal Publications

1. **Y. Yang**, C. Galland, Y. Liu, K. Tan, R. Ding, Q. Li, K. Bergman, T. Baehr-Jones, and M. Hochberg, "Experimental demonstration of broadband Lorentz non-reciprocity in an integrable photonic architecture based on Mach-Zehnder modulators," Opt. Express, vol.22, no.14, pp.17409-17422 (2014).（**Note: This paper is selected by Opt. Express editor as Spotlight on Optics: http://www.opticsinfobase.org/spotlight/summary.cfm?URI=oe-22-14-17409)**
2. **Y. Yang**, R. Ding, M. Streshinsky, Y. Liu, Z. Xuan, Q. Li, K. Bergman, T. Baehr-Jones, and M. Hochberg, "Highly linear low $V\pi{\cdot}L\pi$ single drive push-pull traveling-wave Mach-Zehnder modulator in silicon," Submitted to Opt. Communications, under peer review, 2015.
3. **Y. Yang**, Y. Ma, H. Guan, Y. Liu, S. Danziger, S. Ocheltree, K. Bergman, T. Baehr-Jones, and M. Hochberg," Phase coherence length in silicon photonic platform," accepted for publication in Opt. Express, 2015)
4. Y. Zhang, S. Yang, **Y. Yang**, M. Gould, N. Ophir, A. Lim, G. Lo, P. Magill, K. Bergman, T. Baehr-Jones, and M. Hochberg, "A high-responsivity photodetector absent metal-germanium direct contact," Opt. Express, vol.22, no.9, pp.11367-11375 (2014).
5. Novack, M. Gould, **Y. Yang**, Z. Xuan, M. Streshinsky, Y. Liu, G. Capellini, A. Lim, G. Lo, T. Baehr-Jones, and M. Hochberg, "Germanium photodetector with

60 GHz bandwidth using inductive gain peaking," Opt. Express, vol.21, no.23, pp.28387-28393 (2013).

6. R. Ding, Y. Liu, Y. Ma, **Y. Yang,** Q. Li, A. Lim, G Lo, K. Bergman, T. Baehr-Jones, and M. Hochberg, "High-Speed Silicon Modulator With Slow-Wave Electrodes and Fully Independent Differential Drive," J. Lightwave Technol., IEEE, vol.32, no.12, pp.2240-2247 (2014).
7. Y. Liu, R. Ding, Y. Ma, **Y. Yang**, Z. Xuan, Q. Li, A. Lim, G. Lo, K. Bergman, T. Baehr-Jones, and M. Hochberg, "Silicon Mod-MUX-Ring transmitter with 4 channels at 40 Gb/s," Opt. Express, vol.22, no.13, pp.16431-16438 (2014).
8. R. Ding, Y. Liu, Q. Li**, Y. Yang**, Y. Ma, K. Padmaraju, A. Lim T. Baehr-Jones and M. Hochberg, "Design and characterization of a 30-GHz bandwidth low-power silicon traveling-wave modulator," Optics Communications vol.321, 124-133(2014).
9. M. Streshinsky, R. Ding, Y. Liu, A. Novack, **Y. Yang**, Y. Ma, X. Tu, E. Chee, A. Lim, P. Lo, T. Baehr-Jones, and M. Hochberg, "Low power 50 Gb/s silicon traveling wave Mach-Zehnder modulator near 1300 nm," Opt. Express, vol.21, no.25, pp.30350-30357 (2013).
10. R. Ding, Y. Liu, Q. Li, Z. Xuan, Y. Ma, **Y. Yang**, A. Lim, G. Lo, K. Bergman, T. Baehr-Jones, M. Hochberg, "A Compact Low-Power 320-Gb/s WDM Transmitter Based on Silicon Microrings," Photonics Journal, IEEE, vol.6, no.3, pp.1-8, (2014).

Conference Publications

1. **Y. Yang**, C. Galland, Y. Liu, T. Baehr-Jones, and M. Hochberg, " Towards a Flexible, Scalable and Low Loss Non-reciprocal System in Silicon Photonics", submit ECOC 2015, OSA/IEEE.
2. Y. Liu, R. Ding, Q. Li, X. Zhe, Y. Li, **Y. Yang**, A. Lim, P. Lo, K. Bergman, T. Baehr-Jones, and M. Hochberg, "Ultra-compact 320 Gb/s and 160 Gb/s WDM transmitters based on silicon microrings," in Optical Fiber Communication Conference, OSA Technical Digest (online) (Optical Society of America, 2014), paper Th4G.6.
3. R. Ding, Y. Ma, Y. Liu, **Y. Yang**, A. Lim, P. Lo, T. Baehr-Jones, and M. Hochberg, "High-speed silicon modulators with slow-wave electrodes," in Optical Fiber Communication Conference, OSA Technical Digest (online) (Optical Society of America, 2014), paper Th2A.35.
4. C. Galland, A. Novack, Y. Liu, R. Ding, M. Gould, T. Baehr-Jones, Q. Li**, Y. Yang,** Y. Ma, Y. Zhang, K. Padmaraju, K. Bergman, A. E. Lim, G. Lo and M. Hochberg, " A CMOS-compatible silicon photonic platform for high-speed integrated opto-electronics," Proc. SPIE, INTEGRATED PHOTONICS: MATERIALS, DEVICES, AND APPLICATIONS II. 8767, G1-G8 (2013).
5. Y. Liu, R Ding, M. Gould, T. Baehr-Jones, **Y. Yang**, Y. Ma, Y. Zhang, A. Lim, T Liow, S. Teo, G. Lo, M. Hochberg, "30GHz silicon platform for photonics system," Optical Interconnects Conference, 2013 IEEE, pp.27-28 (2013).

6. A. Novack, Y. Liu, R. Ding, M. Gould, T. Baehr-Jones, Q. Li, **Y. Yang**, et al. "A 30 GHz Silicon Photonic Platform," Proc. of SPIE Vol.8781, invited talk (2013).
7. M. Streshinsky, A. Novack, Y. Liu, R. Ding, M. Gould, T. Baehr-Jones, Q. Li, **Y. Yang**, et al." A 30 GHz Silicon Photonic Platform," Photonics Society Summer Topical Meeting, IEEE, invited talk, (2013).
8. C. Galland, A. Novack, Y. Liu, R. Ding, M. Gould, T. Baehr-Jones, Q. Li, **Y. Yang**, et al. "Systems and devices in a 30 GHz Silicon-on-Insulator platform," ECOC, pp.1, 3, 22-26 (2013).

Appendix C

REPRINT PERMISSION

Most of the published works that directly related this dissertation were available on OSA (Optical Society of America) journals. OSA's copyright transfer agreement gives authors the right to publish the article or chapter in a compilation of the author's own works. The detailed information can be found on its website:

http://www.opticsinfobase.org/oe/submit/review/copyright_permissions.cfm

Here is a detailed description from the website: Transfer of copyright does not prevent an author from subsequently reproducing his or her article. OSA's Copyright Transfer Agreement gives authors the right to publish the article or chapter in a compilation of the author's own works or reproduce the article for teaching purposes on a short-term basis. The author may also publish the article on his or her own noncommercial web page ("noncommercial" pages are defined here as those not charging for admission to the site or for downloading of material while on the site). In addition, we allow authors to post their manuscripts on the Cornell University Library's arXiv site prior to submission to OSA's journals.